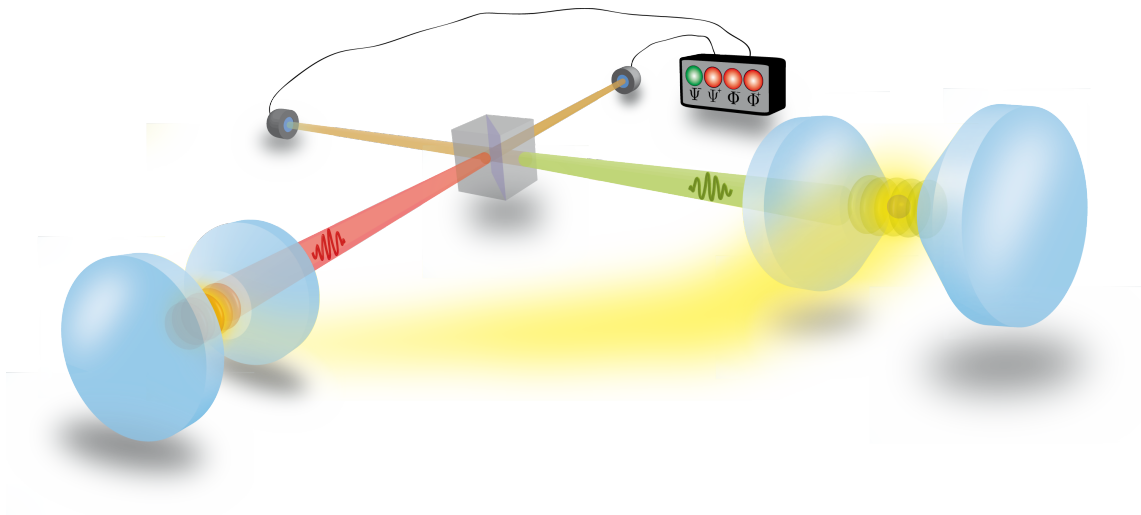# MAX-PLANCK-INSTITUT FÜR QUANTENOPTIK

Quantum state transfer between remote single atoms

Christian Nölleke

Cover illustration: Artist's view of quantum teleportation between two atoms coupled to cavities using an optical Bell-state measurement.

Technische Universität München

Max-Planck-Institut für Quantenoptik

Quantum state transfer between remote single atoms

Christian Nölleke

Abstract

The coupling of a single atom to a high-finesse optical cavity enables efficient information exchange between material and photonic quantum bits. In this thesis, it is demonstrated that an atom-cavity system is a quantum memory for polarization qubits encoded in single photons. Based on this ability, an elementary quantum network comprised of two independent quantum memories separated by 21 m is realized, and two different approaches to quantum communication are investigated. First, the direct transfer of quantum states between the two network nodes is demonstrated. To this end, the atomic state of the sender is mapped onto the polarization of a single photon. By using an optical fiber, the photon is directed to the receiver site where it is finally stored in the atom. In a second experiment, quantum states are transferred between the atoms using teleportation. Initially, sender and receiver share an entangled atom-photon state. The state of the sender is then mapped onto another photon. Conditioned on the outcome of a Bell-state measurement of the two photons, the atom at the receiver site is projected onto the state of the sender atom. The utilization of an optical cavity to enhance the coupling between light and matter results in high success probabilities of the explored protocols. This demonstrates that cavity-based systems are promising candidates for the realization of more complex quantum networks.

Kurzfassung

Die Kopplung eines einzelnen Atoms an einen optischen Resonator hoher Finesse ermöglicht einen sehr effizienten Informationsaustausch zwischen materiellen und photonischen Quantenbits. In der vorliegenden Arbeit wird gezeigt, dass ein Atom-Resonator-System ein Quantenspeicher für Polarisationsqubits einzelner Photonen ist. Darauf aufbauend wird ein elementares Quantennetzwerk aus zwei unabhängigen Quantenspeichern mit einer Entfernung von 21 m realisiert und es werden zwei unterschiedliche Ansätze zur Quantenkommunikation untersucht. Zunächst wird der direkte Transfer von Quantenzuständen zwischen den beiden Netzwerkknoten demonstriert. Der atomare Zustand des Senders wird hierbei auf die Polarisation eines einzelnen Photons übertragen. Mittels einer optischen Faser wird dieses Photon zur Empfängerseite geführt, wo es im Atom gespeichert wird. In einem zweiten Experiment werden Quantenzustände mittels Teleportation zwischen den beiden Atomen transferiert. Hierzu wird zunächst ein verschränkter Atom-Photon-Zustand zwischen Sender und Empfänger erzeugt. Der Zustand des Senders wird auf ein weiteres Photon übertragen. Konditioniert auf das Ergebnis einer Bell-Zustands-Messung zwischen den beiden Photonen wird das Atom auf der Empfängerseite auf den Zustand des Senderatoms projiziert. Die Verwendung optischer Resonatoren zur Erhöhung der Kopplung zwischen Licht und Materie resultiert in hohen Erfolgswahrscheinlichkeiten der untersuchten Protokolle. Dies demonstriert, dass die Verwendung resonatorbasierter Systeme ein vielversprechender Ansatz für die Realisierung komplexerer Quantennetzwerke ist.

Contents

1. Introduction

Quantum mechanics has grown into one of the fundamental pillars of modern physics, broadening our understanding of nature and triggering the development of new technologies. For example, technologies such as the laser [1], nuclear magnetic resonance spectroscopy [2] and atomic clocks [3] have already entered our everyday life. Recently a new field of research has arisen, *quantum engineering*, in which the principles of quantum mechanics are directly employed to manipulate the physical world at the quantum level [4]. Examples of fields which have emanated from quantum engineering include quantum metrology [5], the design of artificial quantum systems [6–9], quantum communication [10] and quantum computation [11].

These latter two fields aim to combine methods of classical information processing with fundamental effects of quantum mechanics. The superposition principle is employed to create a novel form of information, *quantum information*, that potentially improves the acquisition, transmission and processing of data [12]. As early as 1982, Richard Feynman pointed out that the simulation of quantum systems is intractable with a classical computer, as the size of its Hilbert space scales exponentially with the number of degrees of freedom of a quantum system [13]. He conjectured that quantum physics could be exploited to efficiently simulate other quantum systems [14]. Similarly, controllable quantum systems can be used to design a *quantum computer* [15, 16] which has the potential to dramatically outperform its classical counterpart in solving certain problems [17, 18]. At the same time—in contrast to classical information which can be implemented robustly using digital architectures—quantum information is very fragile. As a consequence, methods and technologies for the processing and communication of quantum information have to meet demands profoundly different from their classical counterparts. The development of such technologies is a main challenge of today's quantum optics research.

Along these lines, an important and already advanced application originating from quantum engineering is *quantum key distribution*, a means to achieve unconditionally secure communication of information [19, 20]. Its security is guaranteed by a fundamental principle of quantum physics—the *no-cloning theorem* [21]. The presence of an eavesdropper unavoidably leaves marks that can be detected by the communicating parties during the protocol. Even with an eavesdropper present, secure communication can be guaranteed by modifying the shared key [22].

In order to implement the aforementioned technologies, the ability to faithfully transfer quantum information between potentially remote sites is essential. For classical information, the approach would be to copy and transmit the information, allowing for a new transmission attempt should the previous one fail. Alternatively, repeaters can be used to amplify the signal at intermediate locations. While the aforementioned no-cloning theorem allows for the secure distribution of keys, it prevents the use of classical methods for the communication

of quantum information. Any attempt to measure a quantum state results in an irreversible projection of the state. Therefore, only partial information about an unknown state can be gained, rendering a classical amplification scheme impossible. Consequently, the faithful transfer of quantum information requires a coherent communication channel, in which the quantum states are not disturbed, i.e. they must be decoupled from the environment. Optical photons are the natural choice for the transmission of quantum information. They can be transmitted with relatively low losses and they are compatible with existing telecommunication fiber technology. Their polarization degree of freedom forms an excellent qubit, as decoherence is small in optical fibers and in free space. For simple point-to-point connections, consisting of a send-only emitter and a receive-only detector, the use of purely photonic systems is sufficient and has already found commercial applications in quantum cryptography systems [23, 24]. In order to fully exploit the promising capabilities of quantum information processing, the transfer of quantum states between functional network nodes that are able to send, receive and store quantum information is required. All these properties are provided by optical quantum memories [25, 26]. At the same time, a reversible and efficient interface between the memory and the communication channels is essential. Connecting these nodes leads to the quantum mechanical counterpart of a network—a *quantum network* [27].

The implementation of quantum network nodes and an efficient interface with photonic channels is a major challenge and different approaches are currently being pursued. Systems which are intensely studied include ensembles of particles consisting of gas-phase atoms [25, 28, 29] or solid-state systems [8, 30]. Collective effects in these systems lead to an enhanced interaction between light and matter, however the protocols for generating single excitations are inherently probabilistic [31]. Other strong contenders are single emitters, such as atoms [32], quantum dots [33] or nitrogen-vacancy centers in diamonds [34, 35], which allow for single-photon emission [36] and quantum gate operations [37–39], and which are scalable to larger architectures [40]. Single emitters usually interact only weakly with single photons, also resulting in inherently probabilistic information exchange and low success rates. In particular, the reversible quantum-state mapping between a photon and a single emitter in free space is highly inefficient. In their seminal work [41], Ignacio Cirac, Peter Zoller, Jeff Kimble, and Hideo Mabuchi proposed in 1997 to overcome these problems using network nodes based on single emitters embedded in optical cavities, thus enabling a deterministic approach for the transfer of quantum states between quantum memories. Besides the existence of a deterministic scheme for quantum communication, the use of single particles is appealing as they can be addressed individually, allowing for the realization of deterministic quantum gates [37–39]. In particular, single atoms are very promising for future applications as they are among the physical systems with the longest coherence times [42].

This thesis makes a significant contribution towards a universal quantum network. We have experimentally realized the prototype of an elementary quantum network based on single atoms embedded in optical cavities. Quantum information is exchanged between the stationary nodes in two different ways: Directly, by employing the aforementioned deterministic scheme [41]. And indirectly, by implementing a teleportation protocol using entanglement, a Bell-state measurement and a classical communication channel [43]. The use of high-finesse cavities enables dynamic control of coherent dark states and allows

for an in-principle deterministic and reversible exchange of quantum states between light and matter, thereby representing a highly efficient interface between a single atom and a photon.

In a first experiment, building on the recently achieved faithful mapping of the polarization of a coherent light pulse onto the internal state of a single atom [44], the polarization of a single photon is mapped onto an atom, and back onto a single photon. This experiment is the first to demonstrate the coherent transfer of a qubit encoded in a single photon onto a single atom and meets all requirements for an optical quantum memory [25, 26]. The same mechanism is exploited in a second experiment, in which the transfer of quantum information between two distant and independent nodes is achieved by exchanging single photons [45]. This *direct quantum state transfer* is especially appealing for quantum communication as it is the conceptually most fundamental way to connect different nodes. Because it is intrinsically deterministic, it is a promising approach to realize quantum networks over short distances.

The inevitable losses in any quantum channel render the direct state transfer impractical for global distances. Nevertheless, long-distance quantum communication can be achieved using a *quantum repeater* architecture [46]. In this scheme, entanglement between distant locations is established by first entangling adjacent nodes at intermediate stations and then performing entanglement swapping [47]. Thereby, the time it takes to distribute entanglement scales only polynomially with distance, rather than exponentially. The transfer of a quantum state between the two distant nodes can then be achieved using *quantum teleportation* that exploits the previously established entanglement link as a resource [43]. Once entanglement has been built up, neither the efficiency nor the fidelity of the state transfer depends on the distance. In another experiment presented in this thesis, we perform quantum teleportation between two distant atomic nodes [48]. The strong light-matter interaction provided by the cavities allows us to share an entangled two-particle state efficiently between the two nodes and to implement an all-optical Bell-state measurement. This results in success probabilities exceeding previous demonstrations of long-distance matter-matter teleportation by several orders of magnitude.

This thesis is organized as follows: In **chapter 2** the atom-cavity systems forming the two nodes of the elementary network are described. **Chapter 3** summarizes the theory for the characterization of quantum states and processes. In **chapter 4** the faithful transfer of arbitrary quantum states between the atoms over a distance of 21 m via the exchange of single photons is described. **Chapter 5** contains the experiment on quantum teleportation of arbitrary qubit states between the two atoms.

2. Atom-cavity systems for quantum networking

The experiments presented in this thesis demonstrate the exchange of quantum bits between optical quantum memories at remote locations. Each memory consists of a single neutral ^{87}Rb atom quasi permanently trapped at the center of a high-finesse optical cavity. The systems are located in different laboratories with a distance of $21\,\text{m}$ between the atoms and operate independently. Because the systems have already been described in detail in previous PhD theses [49–52], only an overview of the most important parts and changes to the setups are presented.

The presence of the cavity increases the light-matter interaction strength and enables an efficient and coherent coupling between the atom and single photons in the cavity. By using control laser fields, the motion of the atom can be cooled [53, 54] and its internal states can be manipulated [50, 52]. High resolution imaging of the atoms allows us to detect the number and position of the trapped atoms [50]. A feedback mechanism controls the position of the atom with micrometer precision and restarts the experimental sequence once the atom is lost [55].

2.1. The atomic qubit

^{87}Rb is an alkali metal and thus has only a single valence electron. This results in a relatively simple level structure and makes it suitable for standard laser-cooling techniques. The nuclear spin of this specific isotope is $I = 3/2$, leading to a ground state $5^2S_{1/2}$ with two hyperfine states $F = 1$ and $F = 2$. The D$_1$ and D$_2$ transitions from the ground states to the excited states $5^2P_{1/2}$ and $5^2P_{3/2}$ have transition wavelengths of $780\,\text{nm}$ and $795\,\text{nm}$, respectively, and are easily accessible with standard diode lasers. Details on the full level structure of the two D-lines can be found in Appendix A.

The Zeeman manifold of the stable hyperfine ground states is used to encode the atomic qubits. The Zeeman quantum number m_F refers to the projection of the total angular momentum onto the quantization axis z, which we define to coincide with the optical axis of the cavity. We use different qubit definitions in the two laboratories (Fig. 2.1a). The qubit at *node A* (the "QGate" laboratory) is encoded in $|\!\downarrow\rangle_{\text{A}} \equiv |F = 2, m_F = -1\rangle$ and $|\!\uparrow\rangle_{\text{A}} \equiv |F = 2, m_F = +1\rangle$, whereas at *node B* (the "Pistol" laboratory) the qubit is encoded in $|\!\downarrow\rangle_{\text{B}} \equiv |F = 1, m_F = -1\rangle$ and $|\!\uparrow\rangle_{\text{B}} \equiv |F = 1, m_F = +1\rangle$. The qubit basis states $\{|\!\downarrow\rangle, |\!\uparrow\rangle\}$ form a pseudo-spin-1/2 system and are therefore referred to as the "spin-down"
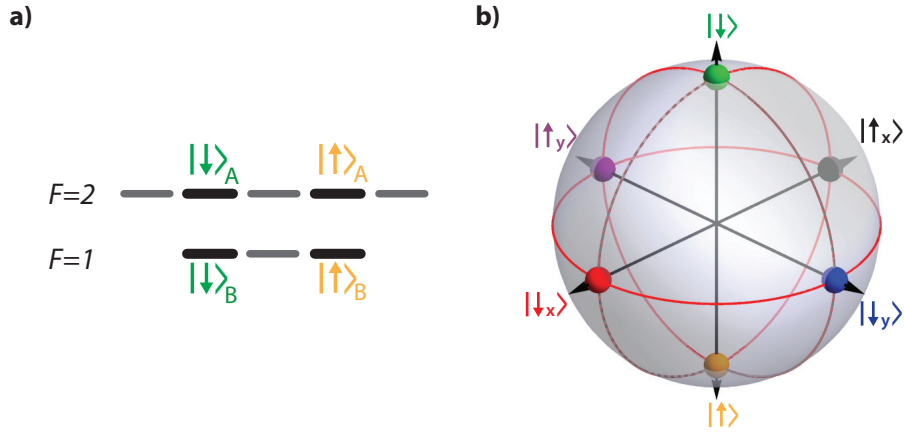
Figure 2.1.: Physical implementation of the atomic qubits at the two nodes. a) The qubit at node A is encoded in the states $|{\downarrow}\rangle_{\mathrm{A}} \equiv |F = 2, m_F = -1\rangle$ and $|{\uparrow}\rangle_{\mathrm{A}} \equiv |F = 2, m_F = +1\rangle$, whereas at node B the qubit is encoded in $|{\downarrow}\rangle_{\mathrm{B}} \equiv |F = 1, m_F = -1\rangle$ and $|{\uparrow}\rangle_{\mathrm{B}} \equiv |F = 1, m_F = +1\rangle$. **b)** Bloch sphere representation of the atomic qubit states. The basis states $|{\downarrow}\rangle$ and $|{\uparrow}\rangle$, which are eigenstates of σ_{z}, are located on the poles. The eigenstates of σ_{x} ($|{\downarrow_{\mathrm{x}}}\rangle, |{\uparrow_{\mathrm{x}}}\rangle$) and σ_{y} ($|{\downarrow_{\mathrm{y}}}\rangle, |{\uparrow_{\mathrm{y}}}\rangle$) lie on the equator.

and "spin-up" states. The basis states are eigenstates of the Pauli operator[1] σ_{z} and are energetically degenerate in the absence of a magnetic field. Any pure qubit state can be written as a superposition of these basis states and can be visualized as a point on the surface of the Bloch sphere [56] (Fig. 2.1b). The eigenstates of the Pauli operators define the six cardinal points of the sphere.

To pump and manipulate the atom we use external cavity diode lasers and a Ti:Sa laser as light sources. All lasers are stabilized to a frequency comb [51] using beat-lock schemes [57, 58], enabling precise locking to an absolutely accurate frequency. The comb teeth are equally spaced with a distance of 250 MHz. Fine-tuning of the individual frequencies of the light fields is achieved using acousto-optical modulators (AOM). With the help of the AOMs, also the power and temporal shape of the fields can be adjusted. The light is combined by using fiber-based beam splitters and is directed to the vacuum chamber, containing the atom-cavity system, using optical fibers.

2.2. The optical cavity

The core of the system is a high-finesse optical cavity (Fig. 2.2). In 2009 one of the cavities (the "QGate") was completely renewed as it suffered from a mirror defect and accompanying high scattering losses [49]. After replacing the cavity, both systems now possess approximately the same parameters which are listed in the following table [51, 59]:

---

[1]The Pauli operators are defined in the computational basis $\{|{\downarrow}\rangle, |{\uparrow}\rangle\}$ as:
$$\sigma_0 \equiv \mathbb{1} = \begin{pmatrix} 1 & 0 \\ 0 & 1 \end{pmatrix}, \quad \sigma_1 \equiv \sigma_{\mathrm{x}} = \begin{pmatrix} 0 & 1 \\ 1 & 0 \end{pmatrix}, \quad \sigma_2 \equiv \sigma_{\mathrm{y}} = \begin{pmatrix} 0 & -i \\ i & 0 \end{pmatrix}, \quad \sigma_3 \equiv \sigma_{\mathrm{z}} = \begin{pmatrix} 1 & 0 \\ 0 & -1 \end{pmatrix}.$$

	node A ("QGate")	node B ("Pistol")
mirror distance $l(\mathrm{\mu m})$	486 ± 0.002	495 ± 0.002
radius of curvature $R(\mathrm{mm})$	50	50
mode waist $w_{0,c}(\mathrm{\mu m})$[1]	30	30
mirror transmissions $T_1/T_2(\mathrm{ppm})$	5.9/99	2/101
free spectral range FSR(GHz)	309 ± 1	303 ± 1
line width $\Delta\nu = \kappa/\pi(\mathrm{MHz})$	4.9 ± 0.1	5.4 ± 0.1
finesse F	60800 ± 1300	56000 ± 1000
round-trip loss $L_{\mathrm{rt}} = 2\pi/F$	103 ± 2	112 ± 2

One important property of the cavities is that the transmission of the mirrors is asymmetric ($T_2 \gg T_1$), such that photons inside the cavity exit the resonator preferentially through one mirror. In combination with low losses, this leads to a high outcoupling efficiency of approximately 90 % into one single free-space optical mode.

The coupling strength between atom and light, and the coupling of both to the environment can be characterized by three parameters. For a given transition with energy $\hbar\omega_c$, the coherent coupling g between atom and cavity is determined by the strength of the atomic transition μ_{ge}, the mode volume V and the position of the atom with respect to the cavity mode $\psi_c(\vec{r})$:

$$g(\vec{r}) = g_0 \cdot \psi_c(\vec{r}) = \sqrt{\frac{\omega_c}{2\varepsilon_0 V \hbar}} \mu_{ge} \psi_c(\vec{r}), \tag{2.1}$$

where ε_0 is the vacuum permittivity. In case of the TEM$_{00}$ mode, the atom-cavity coupling is spatially modulated by

$$\psi_c(\vec{r}) = \cos\left(\frac{\omega_c}{c} z\right) \exp\left(-\frac{x^2 + y^2}{w_{0,c}^2}\right), \tag{2.2}$$

with the speed of light c. To achieve high coupling, the mode volume and therefore, for a given radius of curvature, the mirror distance needs to be as small as possible. The value of $l \approx 0.5\,\mathrm{mm}$ in our system is a compromise between a small cavity length and the need for convenient transversal optical access. For the experimentally relevant transition $5S_{1/2}\,|F = 1\rangle \leftrightarrow 5P_{3/2}\,|F = 1\rangle$, the maximum achievable atom-cavity coupling is $g_0/2\pi = 5.1\,\mathrm{MHz}$. Because the atom is not tightly confined along the cavity axis, the coupling constant fluctuates in time and leads to an average coupling g_{eff} that is approximately a factor of two smaller than the maximum value.

The losses of the system are described by the decay rate of the excited atomic state ($\gamma/2\pi = 3\,\mathrm{MHz}$) and the decay rate of the resonator field ($\kappa/2\pi \approx 2.5\,\mathrm{MHz}$). The resulting cooperativity $C_{\mathrm{eff}} = \frac{g_{\mathrm{eff}}^2}{2\gamma\kappa} \gtrsim 0.3$ indicates that the system is in the intermediate coupling regime of cavity QED.

A cylindrically shaped piezo tube controls the distance between the cavity mirrors and therefore allows for precise tuning of the resonance frequency of the cavity. It is stabilized to a diode laser that is resonant with the cavity, but detuned from the atomic resonance

---

[1]The mode waist is calculated from the the radius of curvature and the mirror distance.
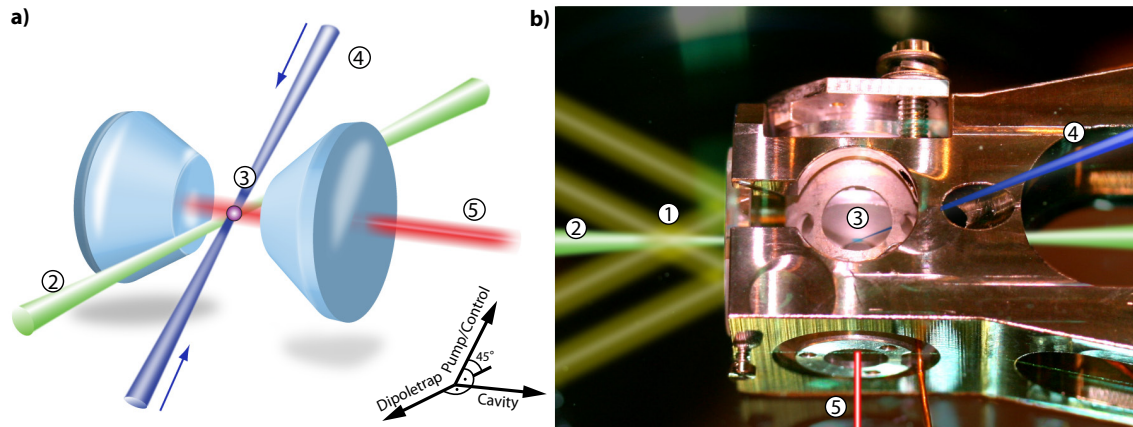
Figure 2.2.: Inside the vacuum chamber. a) Sketch of the atom-cavity system [59]. **b)** Photomontage, showing the actual system and the relevant laser beams. ① Atoms are cooled in a magneto-optical trap (MOT) and guided into the cavity ③ where they are finally trapped using a standing-wave dipole trap ②. The cavity is composed of two coned mirrors facing each other. A laser beam ④ from the side allows for cooling and manipulation of the atoms. Photons ⑤ are coupled into and out of the cavity using the higher transmissive mirror.

by several nanometers, using the Pound-Drever-Hall technique [60]. The cavity at node A is stabilized to a laser operating at 771 nm. For the experiments described in chapter 4, the cavity at node B is stabilized to a laser with a wavelength of 785 nm, whereas for the experiments in chapter 5 a wavelength of 769 nm is used.

2.3. Loading and trapping of single atoms

This section explains the setup used for loading and trapping of single atoms at node A for the experiment described in section 5. The setup at node A used for the experiments from section 4 was presented in [59]. A detailed description of the setup used at node B can be found in [51].

Every experimental sequence starts by loading a cloud of cold ^{87}Rb atoms in a magneto-optical trap (MOT). A diode-pumped, solid-state laser provides light with a wavelength of 1064 nm to create a far-off-resonance trap (FORT). It has a focus between the MOT and the cavity, and acts as an optical tweezer that guides atoms into the cavity region. This transport typically takes 100 ms. After this time, a second beam that is retroreflected forms a one-dimensional optical lattice along the direction of the beam. A sketch of the optical path of the trapping beams is shown in Fig. 2.3. The light is split into two paths using an electro-optical modulator (EOM) and a polarizing beam-splitter (PBS). The beams are coupled into special high-power fibers. This has two advantages. First, any drift of the beam position in front of the fibers does not influence the optical lattice, as the laser power behind the fibers is actively stabilized using the EOM and an acousto-optical modulator (AOM) as actuators. Additionally, in case of laser replacement or change of the optics, no realignment is necessary. Second, the light at the output of the fibers forms a good TEM$_{00}$-mode. This avoids any detrimental effects of bad beam profiles on the
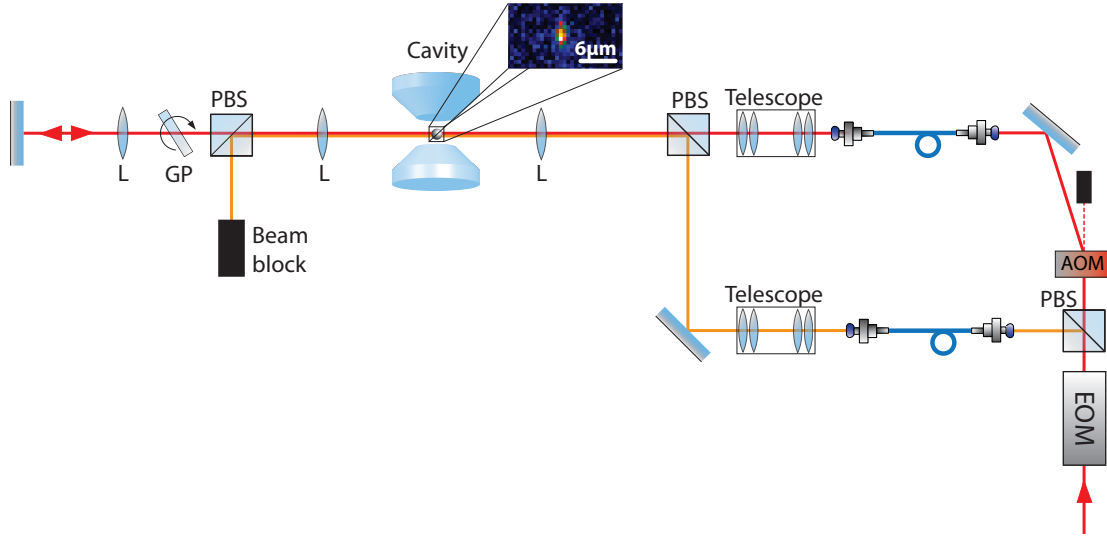
Figure 2.3.: Setup for the far-off-resonance dipole trap. Light from the laser is split into two paths (orange: transfer trap, red: standing-wave trap) using an EOM and a PBS. At the same time, the EOM serves to stabilize the power of the transfer trap. An AOM is used to stabilize the power of the standing-wave trap. The focus diameters and the Rayleigh lengths of the two traps are adjusted by two telescopes. By choosing different divergences of the beams, the position of the foci can independently be adjusted. Using a first lens (L) with a focal length of 15 cm, the beams are focused into the vacuum chamber, and collimated with a second lens behind the chamber. The beam of the standing-wave trap is retroreflected. A tiltable glass plate (GP) is used to shift the lattice along the axis of the beam. The inset shows a typical fluorescence image of a single atom.

geometry of the traps. For retroreflection of the beam, a cat-eye configuration is used: A lens focuses the beam onto a flat mirror. Placing the mirror in the focal plane of that lens guarantees that the reflected beam matches the mode of the incoming beam. This dramatically simplifies the adjustment of the lattice and makes it less sensitive to acoustic noise and thermal drifts.

In addition to the far-off-resonance trap, which forms a standing-wave potential perpendicular to the cavity axis, the light that is used to stabilize the resonator length provides a standing-wave potential along the cavity axis. The parameters of the traps are summarized in the following table:

	FORT	cavity trap
wavelength	1064 nm	771 nm
mode waist	16 µm	30 µm
Rayleigh length	0.8 mm	3.6 mm
trap depth	1.5 mK/W	6.6 mK/W
Typical power	2 W	40 mW

In order to trap the atoms as long as possible, repetitive intervals of cooling with near-resonant light on the closed transition $F = 2 \leftrightarrow F' = 3$ and a repumper on the transition $F = 1 \leftrightarrow F' = 2$ have to be applied. This leads to a Sisyphus-like cooling force [53] that

enables trapping times on the order of one minute, depending on the specific experimental protocol [59].

The atoms can be monitored using a high-resolution imaging system. The central cavity region is imaged onto an EM-CCD camera using an objective with a numerical aperture of 0.4 [50, 61]. A large part of fluorescence light is collected by the objective. A typical image for an exposure time of $\sim 500\,\mathrm{ms}$ is shown as an inset in Fig. 2.3. The imaging system allows us to detect the presence and the position of a single atom. With the help of a tiltable glass plate in front of the retro-reflecting mirror, the atom can be positioned along the dipole trap axis with micrometer precision [55]. Once the atom is lost, the experiment is restarted by loading a MOT and a new transfer attempt.

2.4. Compensating offset magnetic fields

Precise control of the magnetic field at the position of the atoms is essential for all experiments based on qubits encoded in atomic Zeeman states [62]. Fluctuations of the magnetic field lead to decoherence as the relative phase between the qubit eigenstates varies in time. Residual constant magnetic fields lead to an in general unwanted phase evolution and must be minimized. By using a magnetic field sensor that is located directly below the vacuum chamber, constant fields and fluctuations up to a frequency of $1\,\mathrm{kHz}$ can be detected with a sensitivity of $1\,\mathrm{mG}$. The sensor is of great help when it comes to the identification of disturbance sources that cause magnetic field fluctuations, for example power supplies near the vacuum chamber [59].

The method of microwave spectroscopy allows us to measure the magnetic field directly at the location of the atoms [51, 63]. A small external magnetic field B leads to a shift of the Zeeman states with quantum number m_F by

$$\Delta E = \mu_{\mathrm{B}} g_F m_F B, \tag{2.3}$$

with $\mu_{\mathrm{B}} = \frac{e\hbar}{2m_{\mathrm{e}}}$ being the Bohr magneton. The Landé factors g_F have opposite signs for the two ground states: $g_{F=1} = -1/2$ and $g_{F=2} = 1/2$. Consequently, there exist seven possible transition frequencies between the states $F = 1$ and $F = 2$. To measure the magnetic field at the position of the atom, the atom is first prepared in $F = 1$. A microwave pulse with a length of typically $1\,\mathrm{ms}$ induces the transition from $F = 1$ to $F = 2$ if the frequency of the microwave matches the resonance frequency of one of the possible transitions. The efficiency of the transfer is determined by measuring the population in $F = 2$ using cavity enhanced fluorescence detection [64] or photon generation. For the spectroscopic measurement, this scheme is repeated for several seconds during which the frequency of the microwave is gradually changed (see Fig. 2.4b). Offset magnetic fields can be compensated using three pairs of Helmholtz coils surrounding the vacuum chamber. One possible procedure to minimize the field is to measure spectra for different settings of the magnetic field and find the optimal setting iteratively. As this is a time consuming task, we implemented an alternative method that directly yields the value for the compensating field we have to apply, by performing only three scans. Instead of scanning the microwave frequency for a given magnetic field, one can also scan the magnetic field at a constant frequency
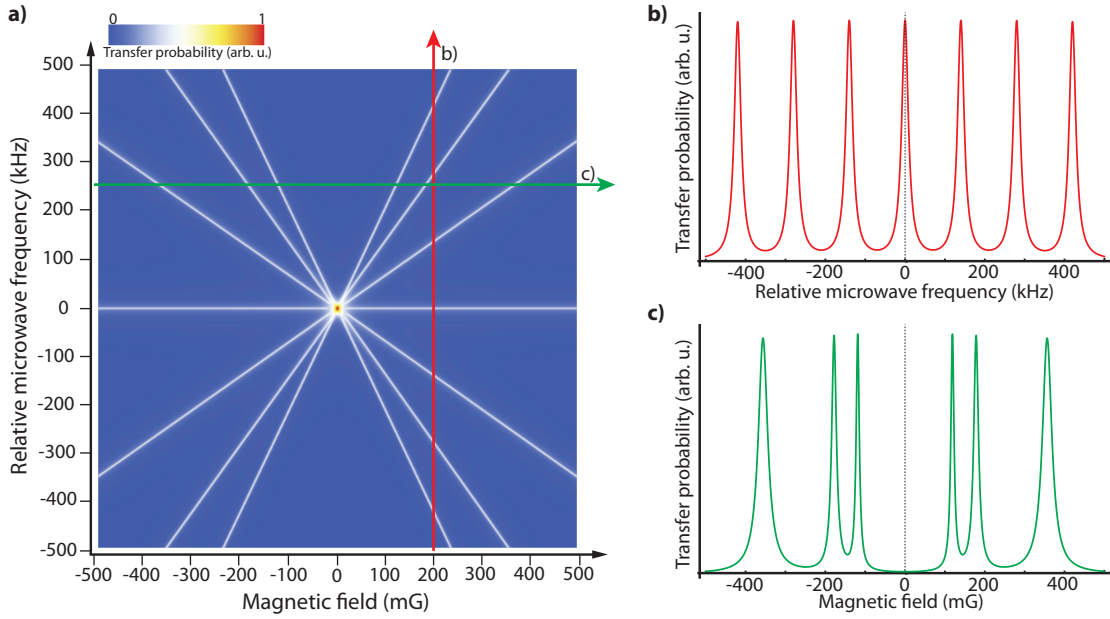
Figure 2.4.: Microwave spectroscopy. a) Transfer probability on the transition $F = 1 \rightarrow F = 2$ induced by a microwave field as a function of the microwave frequency and an externally applied magnetic field according to Eq. (2.3) with $g_F \mu_{\mathrm{B}} = 0.7\,\mathrm{MHz/G}$. **b)** Transfer probability as a function of the microwave frequency for a constant magnetic field of $200\,\mathrm{mG}$. **c)** Transfer probability as a function of the magnetic field for a constant microwave frequency of $250\,\mathrm{kHz}$.

(Fig. 2.4a). An example of the resulting transfer probability as a function of the field is shown in Fig. 2.4c. At the point of symmetry, the magnetic field along the scanned axis is zero. This scan has to be repeated once for each direction in space. A compensation of the magnetic field in all directions can be performed within a few minutes. After compensating the magnetic field, it is possible to achieve a single peak in the spectroscopic measurement. The width is $\sim 10\,\mathrm{kHz}$, corresponding to residual magnetic field fluctuations of $\sim 3\,\mathrm{mG}$. To maintain this small magnetic offset field, the scan must be repeated regularly every few hours to compensate for long-term drifts of the field.

2.5. Analyzing the polarization of a single photon

Central to experiments with polarization qubits is the ability to reconstruct the polarization state of an ensemble of identical single photons. Such a measurement can be realized using a quarter-wave plate ($\lambda/4$), a half-wave plate ($\lambda/2$), a polarizing beam splitter (PBS) and two single-photon detectors (Fig. 2.5a). Because any polarization state of light can be transformed into horizontal (H) or vertical (V) polarization, an arbitrary polarization and its orthogonal complement can be measured with a single-photon detector in both output ports of the PBS [65]. The two orthogonal polarizations define the measurement basis and are set by the orientation of the waveplates. Due to the projective nature of the quantum mechanical measurement one has to perform one and the same measurement on identical copies of the photon to gain enough information about the polarization.

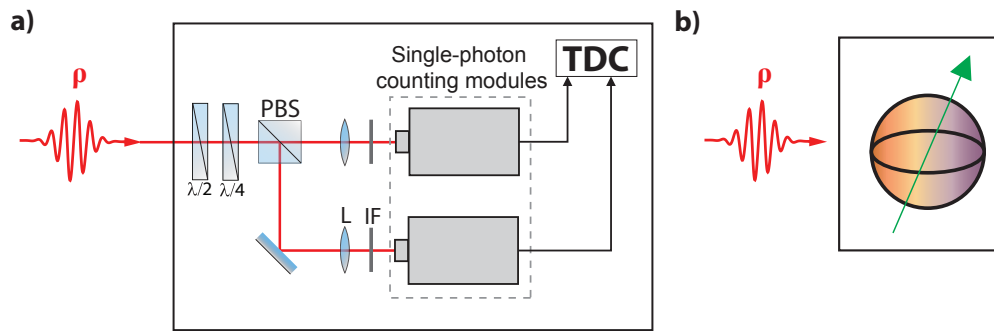**Figure 2.5.: Setup for the detection of the polarization of single photons. a)** The settings
of the waveplates define the measurement basis. Single-photon counting modules monitor the output
ports of the PBS. Two lenses (L) focus the light onto the sensitive area of the detector. Interference
filters (IF) suppress stray light. The output of the single-photon detectors are connected to a
time-to-digital converter (TDC). **b)** Throughout this thesis, the depicted symbol is used for the
setup shown in a).

The PBS has an extinction ratio of $1/1000$ in transmission and $1/200$ for reflected light. The
waveplates have a measured deviation from the desired retardation of $< \lambda/400$. Overall, the
quality of the polarization optics corresponds to a negligible degradation of the measured
fidelities. To switch quickly and reproducibly between different settings of the measurement
basis, the waveplates are mounted in motorized rotation stages. To suppress stray light and
light from the laser used for the stabilization of the cavity, interference filters are placed
behind the output of the cavities and in front of the detectors. In the experiments presented
in this thesis, different types of single-photon counting modules (SPCM) are used. The
detectors SPCM-ARQ16 (Perkin&Elmer) have a quantum efficiency of about $50 \ldots 65\%$ and
a dark-count rate of $25\,\mathrm{Hz}$, whereas the detectors COUNT (Laser Components) typically
have a slightly higher quantum efficiency ($55 \ldots 60\%$) and a lower dark-count rate ($10\,\mathrm{Hz}$).
A detected photon results in a TTL-pulse that is registered by a time-to-digital converter
(TDC)[2]. The temporal resolution of the detection system is $2\,\mathrm{ns}$.

In this thesis, the symbol depicted in Fig. 2.5b is used to represent the described apparatus
for polarization detection.

2.6. Connecting two systems

The two laboratories are connected optically by a fiber of $60\,\mathrm{m}$ length with anti-reflection
coated end-facets.

In each setup, an FPGA-based digital pattern generator is used to control the timing of the
laser pulses and the data recording of the single photon detectors. The jitter between digital
pulses within a sequence is small compared to the temporal resolution of the detection
system. The two generators are synchronized to one another to ensure relative accuracy
between the experimental runs in the two systems.

---

[2]FastComtec P7888

3. Tomography of quantum states and quantum processes

In this thesis, experiments are presented in which qubits are stored in a single atom or transferred between two single atoms. In all of these experiments an initial quantum state is transformed into an output state. These transformations can be abstracted as *quantum processes*. It is possible to quantify such a process by measuring the output states for a finite set of input states. Using the method of *quantum process tomography* it is then possible to predict the outcome of the process for any input state, even if it has not been tested explicitly. In this section, a description of quantum processes and process tomography is given. We restrict ourselves to the relevant case of single qubits.

3.1. Quantum processes of single qubits

A *quantum process* is the transformation of an initial quantum state ρ_{in} (either pure or mixed) into another state ρ_{out}. In general, such a transformation is described by a *completely positive map* $\mathcal{E}$ [56]:

$$\rho_{\mathrm{in}} \rightarrow \rho_{\mathrm{out}} = \mathcal{E}\left(\rho_{\mathrm{in}}\right). \tag{3.1}$$

Once the function $\mathcal{E}$ is known, the outcome of the corresponding quantum process can be predicted for any initial quantum state. In general, the map $\mathcal{E}$ is not unitary as it can also describe loss and decoherence mechanisms. It is convenient to assume that $\mathcal{E}$ does not necessarily preserve the trace. A physical quantum process, however, must not increase the trace, i.e. $0 \leq \mathrm{Tr}[\mathcal{E}(\rho)] \leq 1$ for any state ρ. The (normalized) output state for such a process is then

$$\rho_{\mathrm{out}} = \frac{\mathcal{E}\left(\rho_{\mathrm{in}}\right)}{\mathrm{Tr}\left[\mathcal{E}\left(\rho_{\mathrm{in}}\right)\right]}. \tag{3.2}$$

$\mathrm{Tr}\left[\mathcal{E}\left(\rho_{\mathrm{in}}\right)\right]$ is the probability to find the output state in the Hilbert space $\mathcal{H}$ of the qubit. The normalization according to Eq. (3.2) is implicitly performed in any post-selective measurement, as for example in our experiments which rely on the detection of single photons. During reconstruction of the output states, only those events are considered where a signal was actually present. In that case, $\mathrm{Tr}\left[\mathcal{E}\left(\rho_{\mathrm{in}}\right)\right]$ is the probability to not loose the photon during the process, where ρ_{in} describes the photonic state. If the losses occurring in the process are independent of the input state, i.e. $\mathrm{Tr}\left[\mathcal{E}\left(\rho_{\mathrm{in}}\right)\right]$ is the same for all ρ_{in}, then $\rho_{\mathrm{out}} \propto \mathcal{E}(\rho_{\mathrm{in}})$. In that case, we refer to this process as also being trace preserving.

A useful representation of $\mathcal{E}$ in the case of qubit states is provided by the *process matrix* χ:

$$\mathcal{E}\left(\rho_{\text{in}}\right) = \sum_{m,n=0}^{3} \chi_{mn} \sigma_m \rho_{\text{in}} \sigma_n, \tag{3.3}$$

with the Pauli matrices σ_i. The matrix χ is positive Hermitian by construction and describes the process completely. If the quantum process is the identity operation, i.e. $\rho_{\text{out}} = \rho_{\text{in}}$, all elements of χ are zero except for χ_{00} being equal to 1. Depolarization and dephasing during the process results in the appearance of other diagonal elements, and a reduction of the element χ_{00}. A phase rotation of the qubit leads to non-vanishing elements χ_{30}, χ_{03} and χ_{33} [59]. If the process is a unitary transformation that can be described by one of the Pauli operators σ_i, the corresponding diagonal element χ_{ii} of the process matrix is equal to 1, while all other elements are equal to zero.

3.2. Single qubit tomography

Any qubit density matrix can be written as a superposition of the Pauli matrices [66]:

$$\rho = \frac{1}{2}\sigma_0 + \frac{1}{2}\sum_{i=1}^{3} S_i \sigma_i, \tag{3.4}$$

with the Stokes parameters S_i. The vector $\vec{S} = (S_1, S_2, S_3)$ is called the Stokes vector and describes the state ρ in the three-dimensional Stokes space (see section 3.4). The Stokes parameters can be calculated from the density matrix:

$$S_i = \text{Tr}\left[\sigma_i \rho\right]. \tag{3.5}$$

For all pure states the norm of the vector is $|\vec{S}| = 1$, while for mixed states the norm is $|\vec{S}| < 1$. In analogy to the measurement of the polarization state of light, the state of a qubit can be determined from a set of measurements in three bases. Let $p_{|\downarrow_i\rangle}(p_{|\uparrow_i\rangle})$ be the probability to find the result $|\downarrow_i\rangle$ ($|\uparrow_i\rangle$), when the state ρ is measured in the basis $\{|\downarrow_i\rangle, |\uparrow_i\rangle\}$. These probabilities are related to the Stokes parameters by[1] [65, 67]

$$\begin{aligned}
S_0 &= p_{|\downarrow_{\text{x}}\rangle} + p_{|\uparrow_{\text{x}}\rangle} = p_{|\downarrow_{\text{y}}\rangle} + p_{|\uparrow_{\text{y}}\rangle} = p_{|\downarrow_{\text{z}}\rangle} + p_{|\uparrow_{\text{z}}\rangle} = 1 \\
S_1 &= p_{|\downarrow_{\text{x}}\rangle} - p_{|\uparrow_{\text{x}}\rangle} \\
S_2 &= p_{|\downarrow_{\text{y}}\rangle} - p_{|\uparrow_{\text{y}}\rangle} \\
S_3 &= p_{|\downarrow_{\text{z}}\rangle} - p_{|\uparrow_{\text{z}}\rangle}.
\end{aligned} \tag{3.6}$$

To experimentally determine these probabilities, one has to perform measurements on an ensemble of identical quantum states ρ. Let $N_{|\downarrow_i\rangle}(N_{|\uparrow_i\rangle})$ be the number of detected events of the result $|\downarrow_i\rangle$ ($|\uparrow_i\rangle$). The normalized Stokes parameters can then be calculated using

$$p_{|\downarrow_i\rangle} = \frac{N_{|\downarrow_i\rangle}}{N_{|\downarrow_i\rangle} + N_{|\uparrow_i\rangle}}, \quad p_{|\uparrow_i\rangle} = \frac{N_{|\uparrow_i\rangle}}{N_{|\downarrow_i\rangle} + N_{|\uparrow_i\rangle}}. \tag{3.7}$$

---

[1]The relations from Eq. (3.6) can readily be derived using Eq. (3.5), and $p_{|\downarrow_i\rangle} = \langle\downarrow_i|\rho|\downarrow_i\rangle$ and $p_{|\uparrow_i\rangle} = \langle\uparrow_i|\rho|\uparrow_i\rangle$.

From the experimentally determined Stokes vector $\vec{S}$, the corresponding quantum state of the qubit can be reconstructed using Eq. (3.4). A measurement of the Stokes parameters is therefore equivalent to a reconstruction of the qubit density matrix. This procedure is called *quantum state tomography* [65,67].

The described formalism applies to both, atomic and photonic qubits. In the experiments presented in this thesis, detection of atomic qubit states is performed by mapping them onto polarization states of single photons. The polarization is then detected using the setup described in section 2.5. The relationship between atomic and photonic qubits is given in Appendix B.

3.2.1. State fidelity and visibility

The *state fidelity* $\mathcal{F}_\mathrm{s}$ between an input state ρ_in and an output state ρ_out is defined as the overlap between these two states:

$$\mathcal{F}_\mathrm{s}\left(\rho_\mathrm{in},\rho_\mathrm{out}\right) = \mathrm{Tr}\left[\sqrt{\sqrt{\rho_\mathrm{in}}\rho_\mathrm{out}\sqrt{\rho_\mathrm{in}}}\right]^2. \tag{3.8}$$

In case of the input state being pure ($\rho_\mathrm{in} = |\psi\rangle\langle\psi|$), this expression can be simplified to

$$\mathcal{F}_\mathrm{s}\left(|\psi\rangle,\rho_\mathrm{out}\right) = \langle\psi|\,\rho_\mathrm{out}\,|\psi\rangle. \tag{3.9}$$

In this case, the fidelity is the expectation value of ρ_out in the state $|\psi\rangle$.

If the qubit state is measured in the basis $\{|\psi\rangle,|\psi_\perp\rangle\}$, the *visibility* $V_{|\psi\rangle}$ is defined as the ratio between the number of detected events N as follows:

$$V_{|\psi\rangle} = \frac{N_{|\psi\rangle} - N_{|\psi_\perp\rangle}}{N_{|\psi\rangle} + N_{|\psi_\perp\rangle}}. \tag{3.10}$$

For a qubit, the visibility is related to the fidelity by

$$\mathcal{F}(|\psi\rangle,\rho_\mathrm{out}) = \frac{1}{2}\left(1 + V_{|\psi\rangle}\right). \tag{3.11}$$

3.3. Quantum process tomography

3.3.1. Tomography of trace-preserving processes

Assuming a trace-preserving process, $\mathcal{E}$ can be experimentally determined according to the following recipe known as *standard quantum process tomography* [68]:

- Prepare a set of four linear independent input states $\{\rho_j = |\psi_j\rangle\langle\psi_j|\}$, i.e. a set that forms a complete basis of the space of 2×2 matrices. Such a set is for example given by the states $|\downarrow\rangle, |\downarrow_\mathrm{x}\rangle, |\uparrow_\mathrm{x}\rangle$ and $|\downarrow_\mathrm{y}\rangle$.

- Apply the (unknown) process described by $\mathcal{E}$ to each $\rho_j = |\psi_j\rangle\langle\psi_j|$.

- Reconstruct the output states $\mathcal{E}(\rho_j)$ by performing quantum state tomography as described in section 3.2.

With this set of reconstructed output states it is possible to find an estimator for χ either analytically by inverting the set of linear equations from Eq. (3.3) [68, 69], or numerically by using four or more input states and a maximum-likelihood approach [70, 71]. Performing complete state tomography requires the preparation of a series of identical realizations of $\mathcal{E}(\rho_j)$, and consequently the repeated execution of the aforementioned steps.

One way to compare two processes described by completely positive maps $\mathcal{D}$ and $\mathcal{E}$, is to average the fidelity $\mathcal{F}_\mathrm{s}\left(\mathcal{D}(\rho_\mathrm{in}),\mathcal{E}(\rho_\mathrm{in})\right)$ between the output states over all pure input states $\rho_\mathrm{in} = |\psi\rangle\langle\psi|$,

$$\overline{\mathcal{F}} = \int_{|\psi\rangle} \mathrm{d}\psi\, \mathcal{F}_\mathrm{s}\left(\mathcal{D}(\rho_\mathrm{in}),\mathcal{E}(\rho_\mathrm{in})\right) = \int_{|\psi\rangle} \mathrm{d}\psi\, \langle\psi| U^\dagger \left[\mathcal{E}(|\psi\rangle\langle\psi|)\right] U |\psi\rangle, \qquad (3.12)$$

where the last expression holds if the reference process $\mathcal{D}$ is a unitary process described by the operator U. Typically, the process $\mathcal{E}$ is compared with the identity operation, i.e. $U = \mathbb{1}$ and $\mathcal{D}(\rho_\mathrm{in}) = \rho_\mathrm{in}$. If $\mathcal{E}$ is known, $\overline{\mathcal{F}}$ can be calculated using Eq. (3.12). On the assumption of a trace-preserving process, the average state fidelity can be determined using four pure states forming a regular tetrahedron, or six states forming a regular octahedron on the Bloch sphere [72]:

$$\overline{\mathcal{F}} = \frac{1}{N} \sum_{\substack{\text{tetrahedron/} \\ \text{octahedron}}} \mathcal{F}_\mathrm{s}\left(U\rho_\mathrm{in}U^\dagger,\mathcal{E}(\rho_\mathrm{in})\right). \qquad (3.13)$$

If a tetrahedron (octahedron) is used, it is $N = 4(6)$. A related figure of merit is the *process fidelity* $\mathcal{F}_\mathrm{proc}$. It compares two quantum processes described by corresponding process matrices χ and Λ and is defined as [73]

$$\mathcal{F}_\mathrm{proc} = \mathrm{Tr}\left[\sqrt{\sqrt{\chi}\Lambda\sqrt{\chi}}\right]^2. \qquad (3.14)$$

It is related to the average state fidelity by

$$\overline{\mathcal{F}} = \frac{1}{3}\left(2\mathcal{F}_\mathrm{proc} + 1\right). \qquad (3.15)$$

3.3.2. Tomography of non-trace-preserving processes

If the process $\mathcal{E}$ exhibits state-dependent losses, it does in general not preserve the trace of the input density matrices. The output states then have to be normalized using Eq. (3.2). A reconstruction of the process matrix χ using a complete basis consisting of four input states as in the case of trace-preserving processes is only possible if the success probabilities for these input states are known [74, 75]. In practice, however, a measurement of the efficiencies is prone to errors, as intensity fluctuations falsify the results. Alternatively, instead of using a complete basis set, a set of six states $\{|\mathcal{B}_j\rangle\}$ that form three mutually unbiased bases of the Hilbert space can be used as input states. For example, the eigenstates of the three

Pauli matrices $|\downarrow\rangle, |\uparrow\rangle, |\downarrow_\text{x}\rangle, |\uparrow_\text{x}\rangle, |\downarrow_\text{y}\rangle$ and $|\uparrow_\text{y}\rangle$, which correspond to the six cardinal points on the surface of the Bloch sphere, form such a set. By means of a maximum-likelihood method, the process matrix is correctly reconstructed without prior knowledge of the individual success probabilities.

The expressions for the average state fidelity and the process fidelity from Eq. (3.13) and Eq. (3.14), are only valid for trace-preserving processes. In the following, these formulas are generalized to non-trace-preserving processes.

As mentioned above, the trace of the output density matrix of a non-trace-preserving process is the probability of obtaining the output state $\mathcal{E}(\rho)$ for a given input state ρ. Using Eq. (3.3), it can be written as [76]

$$\text{Tr}\left[\mathcal{E}(\rho)\right] = \text{Tr}\left[\sum_{m,n}\chi_{mn}\sigma_m\rho\sigma_n\right] = \text{Tr}\left[\mathcal{P}\rho\right], \tag{3.16}$$

with the semidefinite positive Hermitian operator

$$\mathcal{P} = \sum_{m,n}\chi_{mn}\sigma_n\sigma_m \leq \mathbb{1}. \tag{3.17}$$

If the process $\mathcal{E}$, described by the process matrix χ, does not preserve the trace, the relation $\mathcal{P} < \mathbb{1}$ holds. Because of $\text{Tr}[\sigma_n\sigma_m] = 2\delta_{mn}$, the condition for the process being non-trace-preserving can equivalently be expressed as $\text{Tr}[\chi] = \frac{1}{2}\text{Tr}[\mathcal{P}] < 1$. Because $\mathcal{P}$ is Hermitian it can be diagonalized and therefore be written as $\mathcal{P} = \sum_i \lambda_i |\lambda_i\rangle\langle\lambda_i|$ with the eigenstates $|\lambda_i\rangle$ and corresponding eigenvalues λ_i. Eq. (3.16) then becomes

$$\text{Tr}\left[\mathcal{P}\rho\right] = \sum_i\sum_k\langle\lambda_i|\rho|\lambda_k\rangle\langle\lambda_k|\rho|\lambda_i\rangle = \lambda_1\langle\lambda_1|\rho|\lambda_1\rangle + \lambda_2\langle\lambda_2|\rho|\lambda_2\rangle. \tag{3.18}$$

The success probabilities for input states that are eigenstates of $\mathcal{P}$ are thus the corresponding eigenvalues λ_1 and λ_2, respectively. Input states that are in a superposition of the eigenstates with equal amplitudes all have the same success probability of $\frac{1}{2}(\lambda_1 + \lambda_2)$. Once the process matrix has been experimentally determined using quantum process tomography, the operator $\mathcal{P}$ can be calculated according to Eq. (3.17). Input states that are oriented along the eigenvectors of this operator are subjected to pure damping, i.e. they preserve their orientation in Stokes space but have different probabilities (λ_1 and λ_2) of being transmitted through the process. States that do not coincide with one of the eigenstates are subjected to damping and rotation that do not preserve angles.

The expression for the process fidelity as given in Eq. (3.14) is generalized by normalizing the matrices χ and Λ by dividing them by their respective traces [74],

$$\mathcal{F}_\text{proc} = \frac{\text{Tr}\left[\sqrt{\sqrt{\chi}\Lambda\sqrt{\chi}}\right]^2}{\text{Tr}[\chi]\text{Tr}[\Lambda]} = \text{Tr}\left[\sqrt{\sqrt{\chi'}\Lambda'\sqrt{\chi'}}\right]^2, \tag{3.19}$$

with $\chi' = \frac{\chi}{\text{Tr}[\chi]}$ and $\Lambda' = \frac{\Lambda}{\text{Tr}[\Lambda]}$. The processes described by χ' and Λ' can be regarded as trace preserving. However, they do not correspond to a physical quantum process since the success probability is larger than 1 for some input states (the corresponding operator $\mathcal{P}$ has at least one eigenvalue larger than 1).

To generalize Eq. (3.13), we use the theory of "state 2-designs". A state 2-design is a set of K states $\{|\psi_j\rangle \in \mathcal{H}, j = 1 \ldots K\}$ satisfying [77,78]

$$\int \mathrm{d}\psi \, \langle\psi| \mathcal{A}_1 |\psi\rangle \langle\psi| \mathcal{A}_2 |\psi\rangle = \frac{1}{K} \sum_{j=1}^{K} \langle\psi_j| \mathcal{A}_1 |\psi_j\rangle \langle\psi_j| \mathcal{A}_2 |\psi_j\rangle, \qquad (3.20)$$

for all operators $\mathcal{A}_1, \mathcal{A}_2$. By making the substitutions $\mathcal{A}_1 = \mathbb{1}$ and $\mathcal{A}_2 = U^\dagger \frac{\mathcal{E}(|\psi\rangle\langle\psi|)}{\mathrm{Tr}[\mathcal{E}(|\psi\rangle\langle\psi|)]} U$ it immediately follows:

$$\overline{\mathcal{F}} = \int_{|\psi\rangle} \mathrm{d}\psi \, \langle\psi| U^\dagger \frac{\mathcal{E}(|\psi\rangle\langle\psi|)}{\mathrm{Tr}[\mathcal{E}(|\psi\rangle\langle\psi|)]} U |\psi\rangle = \frac{1}{K} \sum_{j=1}^{K} \langle\psi_j| U^\dagger \frac{\mathcal{E}(|\psi\rangle\langle\psi|)}{\mathrm{Tr}[\mathcal{E}(|\psi\rangle\langle\psi|)]} U |\psi_j\rangle. \qquad (3.21)$$

For the case of single qubits, a 2-design is formed by the six eigenstates of the Pauli operators $\sigma_{\mathrm{x}}, \sigma_{\mathrm{y}}$ and σ_{z} [79]. These eigenstates form a set of three mutually unbiased bases. The extension of Eq. (3.13) to the case of non-trace-preserving processes is therefore to average over the output states that are normalized by their respective traces. The relation in Eq. (3.15) remains valid [80].

3.4. Visualization of quantum states and processes

Single qubit processes can be visualized using the Bloch sphere. As was mentioned in section 3.2, any qubit density matrix can be described in the three-dimensional Stokes space using the Stokes vector $\vec{S}$ [Eq. (3.4)]. Pure states with $|\vec{S}| = 1$ lie on the surface of the unit Bloch sphere, while mixed states ($|\vec{S}| < 1$) are located inside the unit sphere. For completely mixed states, the density matrix is $\rho = \frac{1}{2}\mathbb{1}_2 = \frac{1}{2}\sigma_0$ and consequently $\vec{S} = 0$. These states are therefore at the center of the sphere.

Performing a complete tomography of a qubit process is equivalent to reconstructing the Bloch sphere. In the typical case, the input states are a set of discrete pure states. The corresponding Bloch sphere is therefore the unit sphere. As explained above, quantum state tomography of the output states of a complete set of input states results in a complete quantum process tomography and fully characterizes the process. The resulting Bloch sphere allows for an intuitive graphical representation of the process by showing the effect of the process on arbitrary input states. If the process is trace preserving, the transformation of the states in Stokes space can be described by

$$\vec{S} \quad \xrightarrow{\mathcal{E}} \quad \mathbb{M}\vec{S} + \vec{c}.$$

The matrix $\mathbb{M}$ induces a compression and rotation of the sphere, which is shifted along the vector $\vec{c}$. Non-trace-preservation leads to anisotropic deformations. An example of a quantum process in Stokes space is shown in Fig. 3.1.

The description of quantum processes is of course not restricted to atomic qubits. Indeed, the same formalism applies also to photonic qubits. In the context of polarization states of light, the term *Poincaré sphere* rather than Bloch sphere is used. In the experiment described in this thesis, the reversible mapping between atomic spin-states and photonic polarization-states is demonstrated. Therefore, a one-to-one correspondence between Poincaré and Bloch sphere exists (see Appendix B), and they are treated equivalently.
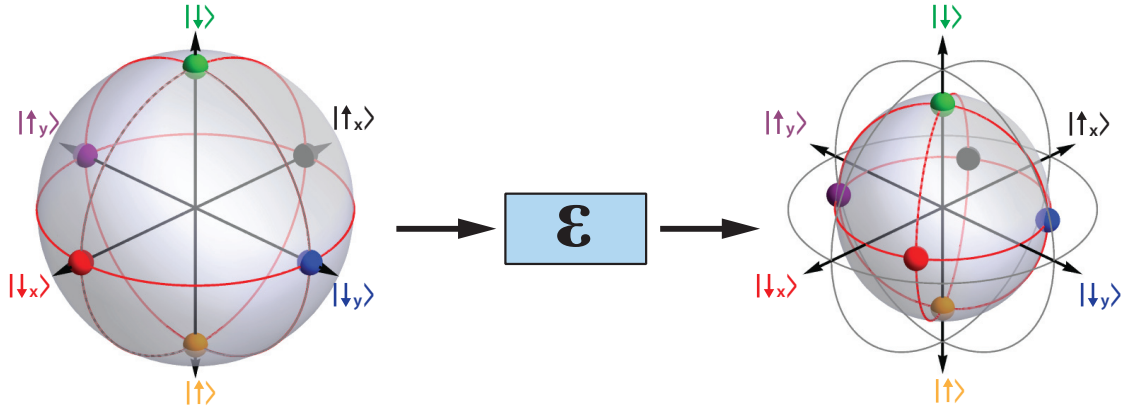
Figure 3.1.: Visualization of a quantum process for qubits. Any qubit state can be represented by a point in Stokes space (colored spheres). Pure states lie on the surface of the unit Bloch sphere, mixed states lie inside. The qubit eigenstates $|\downarrow\rangle$ and $|\uparrow\rangle$ lie on the poles. The figure shows an example of a quantum process acting on pure input states. The effect on arbitrary input states is immediately visible from the deformation and rotation of the sphere.

3.5. Characterization of entanglement

One of the most remarkable and counterintuitive features of quantum mechanics is the existence of *entanglement*. The notion of entanglement was defined by Erwin Schrödinger and he stated in a seminal work in 1935 [81]: "I would not call [entanglement] *one* but rather *the* characteristic trait of quantum mechanics, the one that enforces its entire departure from classical lines of thought." Besides its fundamental importance for the understanding of nature, entanglement is of high relevance in the context of quantum communication [43, 82] and quantum metrology [5].

The experiments presented in this thesis solely deal with bipartite entanglement. Consider two particles A and B with corresponding Hilbert spaces $\mathcal{H}_A$ and $\mathcal{H}_B$. A state ρ from the two-particle Hilbert space $\mathcal{H} = \mathcal{H}_A \otimes \mathcal{H}_B$ is called separable, if it can be expressed in the form

$$\rho = \sum_i p_i \rho_i^A \otimes \rho_i^B, \tag{3.22}$$

with $\sum_i p_i = 1$ and $p_i \geq 0$. $\rho_i^A (\rho_i^B)$ is a density operator that describes the single-particle state in $\mathcal{H}_A (\mathcal{H}_B)$. A state ρ is said to be entangled, if and only if it is not separable.

Criteria exist that enable us to experimentally test whether a state ρ is entangled or separable. The most obvious way is to reconstruct the density matrix of the two-particle state ρ. This can be done by first reconstructing the individual single-particle states by means of quantum state tomography (see section 3.2), and then correlating measurement results obtained in different bases (see for example [50]). The degree of entanglement can then be quantified by means of several measures [83, 84]. Furthermore, the fidelity, which measures the overlap of the generated with an assumed ideal entangled state, can be computed. If the fidelity is above a certain threshold, the state ρ is non-separable. While the full density matrix provides complete information about the quantum state, its

tomographic reconstruction requires a big experimental effort. In the case of a two-qubit state, correlation measurements in nine different combinations of basis settings are required.

It is, however, possible to detect whether a given state is entangled or not with fewer number of measurements, using a so-called entanglement witness [85]. An entanglement witness $\mathcal{W}$ is a Hermitian operator with the following properties:

- $\mathrm{Tr}[\mathcal{W}\rho] < 0$ if ρ is entangled,
- $\mathrm{Tr}[\mathcal{W}\rho_{\mathrm{sep}}] \geq 0$ for all separable states ρ_{sep}.

It is worth mentioning that for a given operator $\mathcal{W}$ entangled states with $\mathrm{Tr}[\mathcal{W}\rho] \geq 0$ exist. The condition $\mathrm{Tr}[\mathcal{W}\rho] < 0$ therefore is a sufficient condition for entanglement, it is, however, not necessary. To construct such an operator $\mathcal{W}$, a priori knowledge of the ideally generated state is required. In the case of the maximally entangled Bell state $|\Psi^-\rangle = \frac{1}{\sqrt{2}}\left(|\downarrow_z\uparrow_z\rangle - |\uparrow_z\downarrow_z\rangle\right)$, with the qubit basis states $\{|\downarrow_z\rangle, |\uparrow_z\rangle\}$,

$$
\begin{aligned}
\mathcal{W} = \frac{1}{2} \big(&|\downarrow_z\downarrow_z\rangle \langle\downarrow_z\downarrow_z| + |\uparrow_z\uparrow_z\rangle \langle\uparrow_z\uparrow_z| + |\downarrow_y\downarrow_y\rangle \langle\downarrow_y\downarrow_y| + |\uparrow_y\uparrow_y\rangle \langle\uparrow_y\uparrow_y| \\
&+ |\downarrow_x\downarrow_x\rangle \langle\downarrow_x\downarrow_x| + |\uparrow_x\uparrow_x\rangle \langle\uparrow_x\uparrow_x| - \mathbb{1} \big)
\end{aligned}
\tag{3.23}
$$

is an entanglement witness [52, 86, 87]. For example $|\downarrow_i\downarrow_i\rangle \langle\downarrow_i\downarrow_i|$ is the projector onto the pure two-qubit state $|\downarrow_i\downarrow_i\rangle$, in which both qubits point into the same direction i in Stokes space. Projective measurements of ρ now allow us to determine the expectation value of $\mathcal{W}$. Let $p_{|\downarrow_i\downarrow_i\rangle}(p_{|\uparrow_i\uparrow_i\rangle})$ be the probability of detecting both qubits in the state $|\downarrow_i\rangle$ $(|\uparrow_i\rangle)$, when the individual qubits are measured in the basis $\{|\downarrow_i\rangle, |\uparrow_i\rangle\}$. The expectation value then becomes

$$
\begin{aligned}
\langle\mathcal{W}\rangle = \mathrm{Tr}[\mathcal{W}\rho] = \frac{1}{2} \big(&p_{|\downarrow_z\downarrow_z\rangle} + p_{|\uparrow_z\uparrow_z\rangle} + p_{|\downarrow_y\downarrow_y\rangle} + p_{|\uparrow_y\uparrow_y\rangle} \\
&+ p_{|\downarrow_x\downarrow_x\rangle} + p_{|\uparrow_x\uparrow_x\rangle} - 1 \big).
\end{aligned}
\tag{3.24}
$$

$\langle\mathcal{W}\rangle$ can consequently be determined by measuring correlations in only three different bases.

The witness $\langle\mathcal{W}\rangle$ is directly related to the fidelity, defined as the overlap between the generated state ρ and the ideal state $|\Psi^-\rangle$ [cf. Eq. (3.9)]: $\mathcal{F}(|\Psi^-\rangle, \rho) = \langle\Psi^-|\rho|\Psi^-\rangle$. It can readily be shown that [52]

$$
\mathcal{F} = \frac{1}{2} - \langle\mathcal{W}\rangle.
\tag{3.25}
$$

A state with $\mathcal{F} > 1/2$, and equivalently $\langle\mathcal{W}\rangle < 0$, indicates non-separability of the measured state.

4. Direct quantum state transfer

The ability to map a quantum state from a single atom onto a single photon and vice versa, is an essential ingredient for the realization of a quantum network based on atoms and photons [27]. A first step towards this goal was the experiment described in [88] where a weak coherent laser pulse was stored in a single Cs atom. The first demonstration of storage and retrieval of a qubit in a single atom was achieved in our experiment [44] by mapping the polarization of a coherent pulse onto the internal state of a single atom, and back onto the polarization of a single photon [89]. The next step is the experimental demonstration of the storage process using true single photons, which is covered in this chapter. By exploiting this technique, the realization of a prototypical quantum network is demonstrated. Quantum information is transferred between two atoms, each coupled to a high-finesse optical cavity, via the exchange of single photons [41]. An arbitrary qubit state, stored in atomic Zeeman states, is mapped onto the polarization of a single photon. This photon is sent to the second atom located in another laboratory, where it is coherently absorbed by the atom. This completes the qubit transfer from one atom to the other.

In the first part of this chapter, the theoretical background for the generation and absorption of single photons in an atom-cavity system based on a stimulated Raman adiabatic passage is briefly explained. After demonstrating the coherent storage of single photons in a single atom, the experimental implementation of the state transfer is described and the results are discussed.

4.1. Generation and storage of single photons using an adiabatic passage

The strong light-matter interaction between a single photon and a single atom, provided by an optical cavity, can be exploited to efficiently transfer atomic onto photonic states and vice versa. By employing a *vacuum-stimulated Raman adiabatic passage* (vSTIRAP), a single photon is coherently generated in a well-defined spatial mode of the cavity [90]. Atom-cavity systems can therefore serve as highly efficient single-photon sources [91, 92]. The same mechanism can be used to coherently store photons, impinging onto the cavity, in an atom. To understand the principle of the vSTIRAP, the description is first restricted to a three-level system in a Λ-type configuration (Fig. 4.1). In addition, any dissipation in terms of coupling to the environment is initially neglected. We consider an atom with
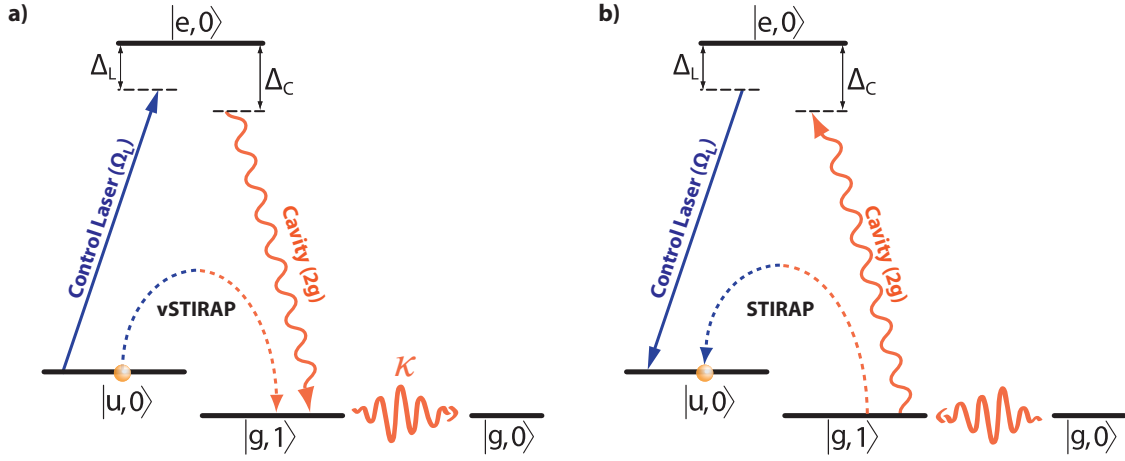
Figure 4.1.: Atom with a Λ-type level scheme coupled to a cavity and an external laser field. A classical laser field with Rabi frequency Ω_L couples the atomic ground state $|u\rangle$ to the excited state $|e\rangle$. The mode of the cavity with vacuum Rabi-frequency $2g$ couples the ground state $|g\rangle$ to the excited state $|e\rangle$. Δ_L (Δ_C) is the detuning of the laser (cavity) field to the respective transition. **a) Single-photon generation.** After initializing the system in $|u,0\rangle$, a vSTIRAP drives the system to the state $|g,1\rangle$, thereby creating a single excitation of the cavity field. The excitation decays with a rate κ. This results in a single photon being emitted in a well-defined spatial mode. The scheme can be repeated by re-initializing the system in $|u,0\rangle$. **b) Single-photon storage.** The system is initially prepared in the state $|g,0\rangle$. A photon entering the cavity, along with a control field, drives an adiabatic passage to the state $|u,0\rangle$.

two electronic ground-states $|g\rangle$ and $|u\rangle$, and one excited state $|e\rangle$. The mode of the cavity couples the states $|g\rangle$ and $|e\rangle$ with the *vacuum Rabi-frequency* $2g$. An external laser field couples the state $|u\rangle$ to the excited state $|e\rangle$ with *control Rabi-frequency* Ω_L. Δ_C and Δ_L are the detunings from the respective transition. The excited state is chosen to be the state with zero energy. Transforming the system to the interaction-picture and using the rotating-wave approximation results in the interaction Hamiltonian [93]

$$H_{\text{int}} = -\hbar \left(g\sigma_{eg}a + \frac{\Omega_c}{2}\sigma_{eu} + \text{H.c.} \right). \tag{4.1}$$

The atomic and cavity part of the Hamiltonian read

$$H_{\text{atom}} = -\hbar\Delta_L\sigma_{uu}, \quad H_{\text{cavity}} = -\hbar\Delta_C a^\dagger a. \tag{4.2}$$

The operator $\sigma_{fi} = |f\rangle\langle i|$ couples the atomic states $|i\rangle$ and $|f\rangle$ for $i \neq f$. For $i = f$ it is the population operator. a ($a^\dagger$) is the annihilation (creation) operator of a photon in the cavity. The state of the combined atom-cavity system is a product state $|x,n\rangle$ with the atomic state $|x\rangle$ ($x \in \{g, u, e\}$), and $|n\rangle$ ($n \in \mathbb{N}$) representing the number of quanta in the cavity. In the following, we restrict ourselves to the subspace with zero or one excitation in the cavity ($n = 0,1$). In the basis $\{|g,1\rangle, |u,0\rangle, |e,0\rangle\}$ the matrix representation of the Hamiltonian is

$$H = H_{\text{atom}} + H_{\text{cavity}} + H_{\text{int}} = -\frac{\hbar}{2}\begin{pmatrix} 2\Delta_C & 0 & 2g \\ 0 & 2\Delta_L & \Omega_L \\ 2g & \Omega_L & 0 \end{pmatrix}. \tag{4.3}$$

In the case of two-photon resonance ($\Delta_L = \Delta_C = \Delta$), one eigenstate of the Hamiltonian is found to be the *dark state*

$$|\varphi_0\rangle = \cos(\theta)\,|u,0\rangle - \sin(\theta)\,|g,1\rangle. \tag{4.4}$$

It is called *dark* because it does not contain any contribution of the excited state $|e\rangle$. As long as the system remains in this state, no light can be emitted via spontaneous decay; the atom stays "dark". The *mixing angle*

$$\tan(\theta) = \frac{\Omega_L}{2g} \tag{4.5}$$

determines the relative amplitude between the states $|u,0\rangle$ and $|g,1\rangle$. For $\Omega_L/2g \to 0$ the dark state is equal to $|u,0\rangle$, while in the other limiting case $\Omega_L/2g \to \infty$ it is equal to $|g,1\rangle$.

The idea of photon generation is to initialize the system in $|u,0\rangle$ and then to transfer the system to the state $|g,1\rangle$ via an adiabatic passage (Fig. 4.1a):

$$|u,0\rangle \xrightarrow{\Omega_L/2g\to\infty} |g,1\rangle. \tag{4.6}$$

This results in a single excitation of the cavity field. The dynamics of the photon generation process is governed by an interplay of temporal amplitude of the control field, atomic transition strengths and frequency detunings [92]. In the idealized description, all dissipative processes have been disregarded. In the real-world experiment, however, the atom and the cavity couple to an external reservoir with rates γ and κ respectively. The cavity decay leads to dissipation of excited states $|n\rangle$ to the vacuum state $|0\rangle$ with rate κ. This mechanism couples cavity excitations to well-defined free-space modes. Similarly, excited atomic states decay to the ground states with a rate γ. In the vSTIRAP scheme the transfer of Eq. (4.6) has to occur adiabatically, such that the system remains in the dark state $|\varphi_0\rangle$ at all times. The condition for adiabaticity can be expressed as follows [93]:

$$\frac{g^2}{\gamma} \gg \dot{\theta} + \frac{\kappa}{2}. \tag{4.7}$$

This relation requires the cooperativity C to be larger than 1, and the mixing angle θ to change slowly in time. If the condition is not fulfilled, the dark state $|\varphi_0\rangle$ is not an eigenstate at all times and the excited state $|e\rangle$ can be populated. This leads to spontaneous atomic decay and loss of photons into free space.

An important feature of the vSTIRAP is that it allows several important properties of the photons to be controlled. The detuning Δ directly sets the frequency of the emitted photons [94], while the temporal envelope of the applied control laser pulse $\Omega_L(t)$ determines the temporal envelope of the photonic wave packet [95]. Moreover, by state-selective coupling of the atom to the cavity it is possible to produce photons with a pre-defined polarization [96, 97]. Similarly, quantum states can be mapped coherently from atomic spin-states onto photonic polarization-states [44]. This wide range of possibilities enabled by the vSTIRAP makes it extremely useful in quantum information experiments. In particular, the adiabatic passage can be employed to generate entanglement between an atom and a photon [89, 98]. This will be used to prepare the atomic qubit in the

state-transfer experiment (section 4.3). Moreover, such a hybrid entangled state is the basis for the distribution of entanglement over large distances, as the photonic part of the state can be transferred to remote locations with high speed and low losses. This is an essential ingredient in the teleportation experiment described in chapter 5.

The task of mapping a photonic onto an atomic state can be conceived as the time-reversal of the photon-generation process (Fig. 4.1b). To this end, the atom is initially prepared in $|g\rangle$ rather than in $|u\rangle$, and the control field is turned on with a Rabi-frequency $\Omega_L \gg 2g$. Decreasing the Rabi-frequency of the control laser adiabatically while a photon is in the cavity drives the system via an adiabatic passage and results in the state $|u,0\rangle$:

$$|g,1\rangle \xrightarrow{\Omega_L/2g \to 0} |u,0\rangle .\tag{4.8}$$

The atomic state is transferred from $|g\rangle$ to $|u\rangle$ and the photon is annihilated.

4.2. A single-atom quantum memory

In this chapter, the implementation of an optical quantum memory based on a single atom coupled to a cavity is explained. We use one of the atom-cavity systems to generate a stream of single photons (node B) and store them coherently in the atom of the second apparatus (node A). After a user-defined storage time, the atom is read out by transferring the atomic state onto the polarization state of a single photon. We analyze the storage-retrieval process by performing quantum process tomography. The measured efficiency and fidelity are compatible with the values obtained from measurements with coherent pulses [44].

Before the experimental implementation and results are discussed, a concise theoretical description of the storage and readout process is given.

4.2.1. Coherent mapping between photonic and atomic states

As was described in section 4.1, the adiabatic passage can be used to efficiently and coherently map single photons onto a single atom. To map a polarization qubit and not only a photonic excitation onto the single atom, the scheme must be extended to a *double Λ-type* system (Fig. 4.2a). The qubit of the photon is encoded in a superposition of right-circular ($|\circlearrowright\rangle$) and left-circular ($|\circlearrowleft\rangle$) polarization. The cavity supports two frequency-degenerate and orthogonal polarization modes. We define the quantization axis to be the cavity axis thus the two modes are circular polarizations, which correspond to atomic σ^+ and σ^- transitions:

$$|\Psi_{\text{photon}}\rangle = \alpha |\circlearrowright\rangle + \beta |\circlearrowleft\rangle \longrightarrow \alpha |\sigma^-\rangle + \beta |\sigma^+\rangle ,\tag{4.9}$$

with complex parameters α and β, and $|\alpha|^2 + |\beta|^2 = 1$. In order to store the photonic qubit in the atom, the $\sigma^\pm$ components have to be mapped coherently onto atomic states. Figure 4.2a shows the implementation of the storage scheme in ^{87}Rb. A photon with a polarization corresponding to a $\sigma^\pm$ transition couples the state $5S_{1/2}|F=1,m_F=0\rangle$ to the state $5P_{3/2}|F=1,m_F=\pm 1\rangle'$, while the control field couples the states $5S_{1/2}|F=2,m_F=\pm 1\rangle$
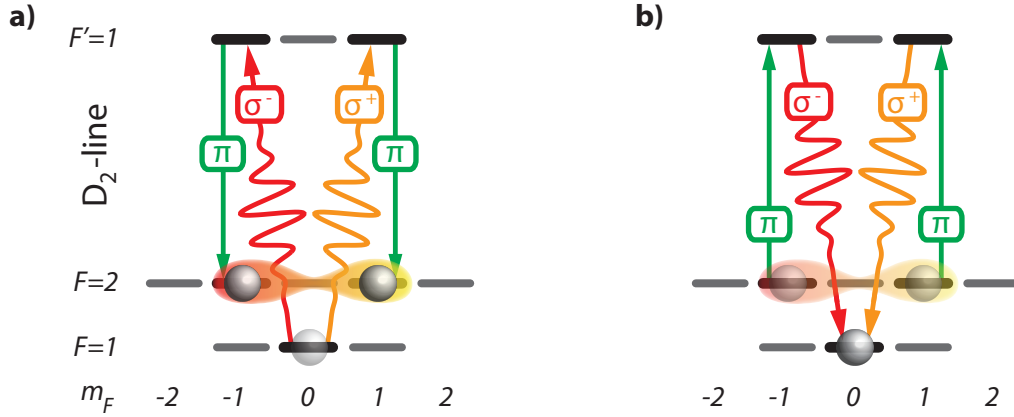
Figure 4.2.: A single-atom quantum memory implemented in ^{87}Rb. a) After preparing the atom in $|1,0\rangle$, the polarization of a single photon is mapped onto a superposition of the states $|2, \pm 1\rangle$ using a vSTIRAP. The polarization components $\sigma^{\pm}$ couple the initial state to the excited states $|1, \pm 1\rangle'$. These states in turn are coupled to the ground states $|2, \pm 1\rangle$ by the π-polarized control field. **b)** Readout of the atom maps the superposition of $|2, \pm 1\rangle$ onto a superposition of the polarization components $\sigma^{\pm}$.

and $5P_{3/2} |F = 1, m_F = \pm 1\rangle'$. This forms two Λ-type systems with a commonly shared ground state $|1,0\rangle$.

Storage is accomplished by preparing the atom in $|1,0\rangle$ and driving a STIRAP with initially one photon and a control laser field with $\Omega_L \gg 2g$. According to Eq. (4.8), ramping the control Rabi-frequency down to zero causes a change of the atomic hyperfine state and the annihilation of the photon. Therefore, the components of the photon driving the $\sigma^{\pm}$ transitions are mapped onto the atomic states $|2, \pm 1\rangle$. Because the two pathways are indistinguishable, no information about the incident polarization is gained and the state does not collapse. This results in phase preservation of the superposition state from Eq. (4.9). We thus denote this mapping process as *coherent storage*. A photon in a superposition of $|\circlearrowright\rangle$ and $|\circlearrowleft\rangle$ is consequently mapped onto an atomic superposition according to

$$\alpha |\circlearrowright\rangle + \beta |\circlearrowleft\rangle \quad \longrightarrow \quad \alpha |2, -1\rangle + \beta |2, +1\rangle. \tag{4.10}$$

To read out the qubit, the storage process is reversed (Fig. 4.2b). After an arbitrary storage time the Rabi frequency of the control laser is increased, driving a vSTIRAP according to Eq. (4.6). Consequently the atomic superposition $\alpha |2, -1\rangle + \beta |2, +1\rangle$ is converted back onto the polarization of another photon with polarization state $\alpha |\circlearrowright\rangle + \beta |\circlearrowleft\rangle$.

4.2.2. Experimental setup

After the theoretical description of the coherent mapping between atomic and photonic states, we now experimentally demonstrate that single photons can be stored in and retrieved from a single atom while preserving their polarization state. To this end, we generate single photons in one atom-cavity system (node B) and coherently store them in the second system (node A). The cavity and the control field are in two-photon resonance
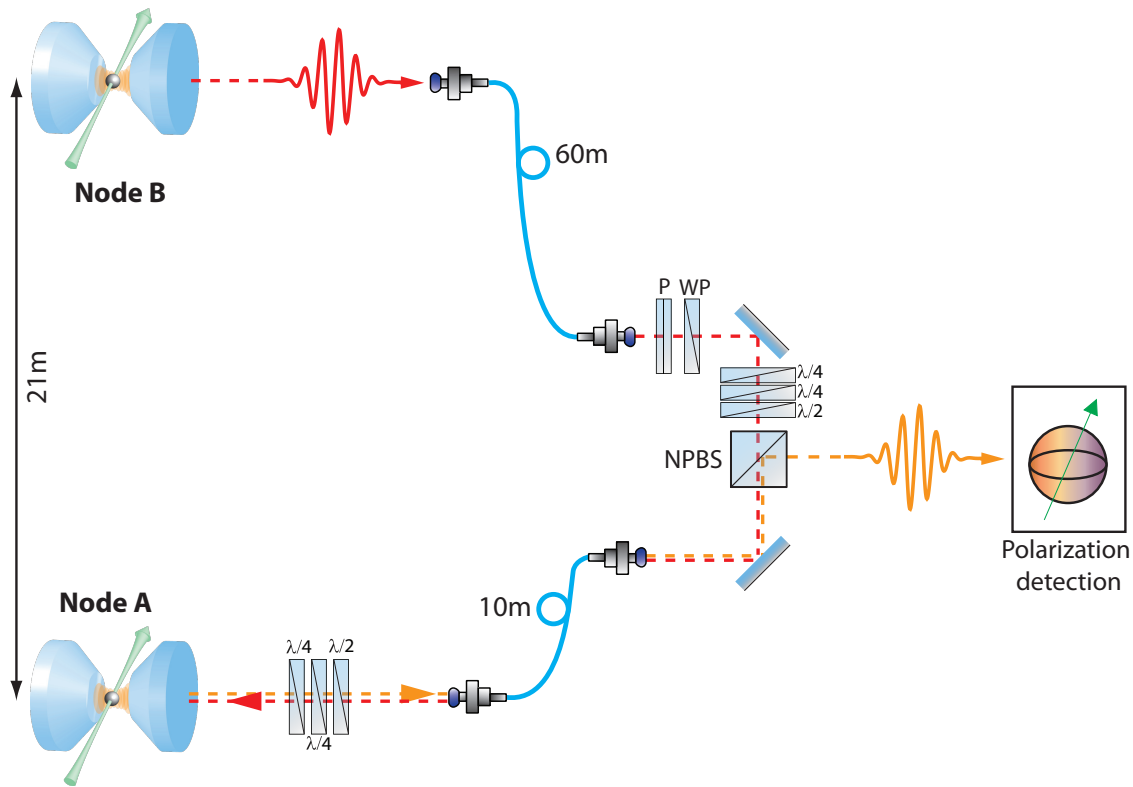
Figure 4.3.: Setup for the characterization of the single-atom quantum memory with single photons. Unpolarized single photons are generated at node B using vSTIRAP (red). These photons are sent to the laboratory of node A via an optical fiber with a length of 60 m. A combination of a polarizer (P) and a waveplate (WP) sets the polarization of the photons. The polarized photons are coherently absorbed in the atom at node A. After storage, the atomic state is measured by mapping it onto the polarization of another single photon (orange) and detecting the polarization. Polarization compensation is achieved using half-wave ($\lambda/2$) and quarter-wave ($\lambda/4$) plates.

($\Delta_C = \Delta_L$), and are 170 MHz blue detuned with respect to the transition of the free atom at both nodes. The Stark shifts of the relevant transitions are 150 MHz ($|2, \pm 1\rangle \leftrightarrow |1, \pm 1\rangle'$ at node A) and 120 MHz ($|2,0\rangle \leftrightarrow |1,0\rangle'$ at node B), respectively. The control laser and cavity resonance are therefore effectively 20 MHz (node A) and 50 MHz (node B) blue detuned from the atom.

A sketch of the setup used to connect the systems and to detect the polarization state of the photons read out from atom A is shown in Fig. 4.3. The two laboratories are linked by an optical fiber with a total length of 60 m. In order to characterize the storage process by means of quantum process tomography, it is necessary to measure the output of the memory for a set of specific input states (see section 3.3). Since we generate single photons with random polarization at node B using vSTIRAP (see section 4.1 and 4.3.1.1), we use a combination of a polarizer and waveplates (either $\lambda/4$, $\lambda/2$, or both) to set the polarization of the incoming photons to a well-defined value. Obviously, the use of the polarizer reduces the rate of incoming photons by a factor of 2. The polarized photons are sent to the cavity

at node A via another fiber with a length of 10 m. To be able to connect the two cavity modes and to detect light coming from the cavity at node A, a non-polarizing beam splitter (NPBS) is placed in between the two fibers. 50 % of the light coming from node B is directed to node A, while 50 % of the light coming from node A is directed to the detection setup. Thus, light read out from atom A after the storage process and light emitted from node B that is reflected off the cavity at node A can be detected and analyzed.

Compensation of unwanted polarization rotations. During transmission of the photon between the two atoms and during transmission of the read-out photon from node B to the detectors, it experiences a change in polarization as some optical components in the beam path are birefringent. The overall change in polarization is a unitary transformation and can therefore be compensated using waveplates. Two combinations of waveplates, each comprised of two quarter-wave and one half-wave plate (see Fig. 4.3), are used to reverse this transformation. To calibrate the compensation, we use polarizers with well-defined settings as a reference, which we place at the output of the cavities. The waveplates are adjusted such that the polarization of light emerging from node B behind the polarizer is the same as in front of the cavity at node A. At the same time, the polarization of light in front of the detection setup has to be the same as the polarization of light emerging from node A behind the polarizer. The compensation has to be performed for two different polarizer settings, corresponding to polarization states which encompass a right angle with respect to each other on the Poincaré sphere, e.g. H and D [99].

4.2.3. Experimental implementation

The experimental sequence used for photon storage is shown in the inset of Fig. 4.4. The individual steps are explained in the following.

Optical pumping at node A. The storage scheme described in section 4.2.1 requires the atom to be initialized in the state $|1,0\rangle$. We achieve this by optical pumping. The transition $|1,0\rangle \leftrightarrow |1,0\rangle'$ is forbidden due to dipole selection rules (see for example [100]), whereas for the states $|1, \pm 1\rangle$ a π-transition to the $F' = 1$ states is allowed. By applying a π-polarized laser resonant with the $F = 1 \leftrightarrow F' = 1$ transition on the D_2-line, the atomic population consequently accumulates in $|1,0\rangle$. As the atom can also decay to $F = 2$, we apply a π-polarized repump laser resonant with the transition $F = 2 \leftrightarrow F' = 1$. This brings population from the $F = 2$ states back into the cycle of optical pumping. The repumper is in two-photon resonance with the cavity field and 20 MHz blue detuned from the Stark-shifted atomic $F = 2 \leftrightarrow F = 1$ transition. In the experiment, we apply a sequence of five consecutive pulses with a length of 2 µs each. The efficiency of the process, i.e. the fraction of population in the state $|1,0\rangle$ after optical pumping, can be experimentally estimated and is found to be $> 90\%$ [59].

Photon generation at node B. After pumping atom B into the state $|2,0\rangle$, the generation of a single photon into the cavity mode is triggered by applying a π-polarized control laser
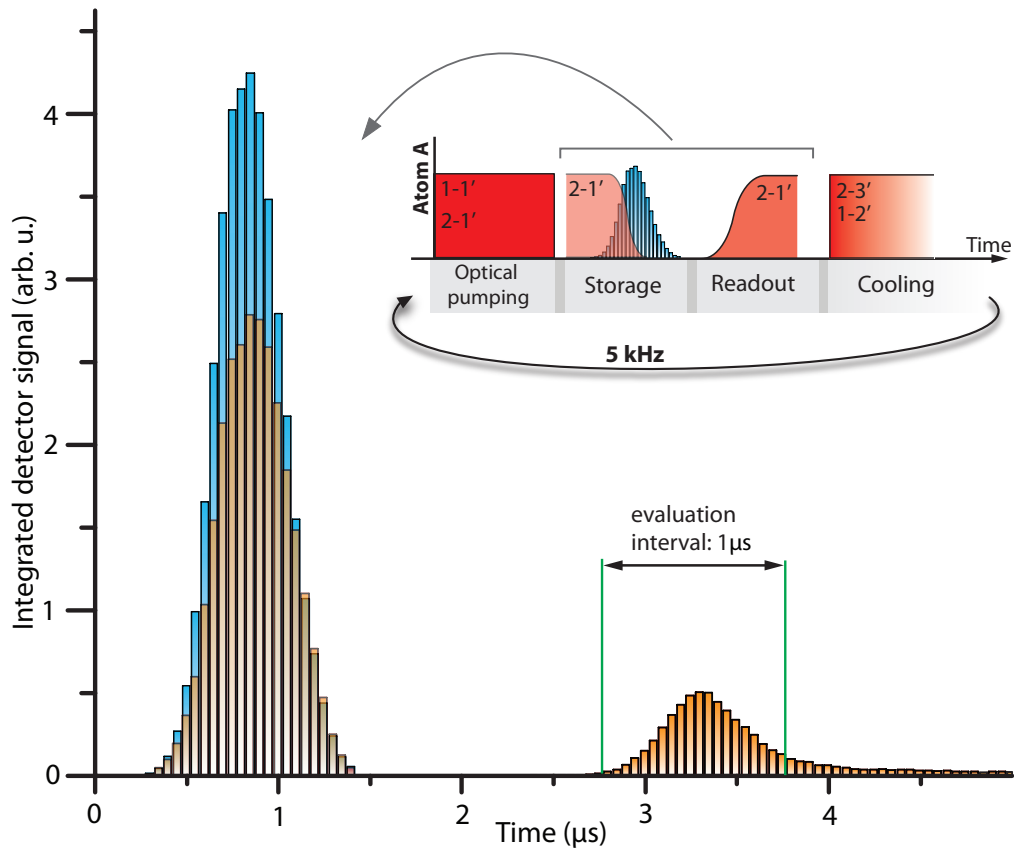
Figure 4.4.: Storage and retrieval of single photons in a single atom. Integrated arrival time histograms of photons for the storage (0 µs - 1.5 µs) and readout process (2.5 µs - 4.5 µs). The blue bars correspond to the reference photon, which is reflected off the cavity while the control field is switched off. The data shown in orange are recorded during storage and readout. A part of the photon is reflected off the cavity without storage. The inset shows a schematic of the experimental sequence of the quantum memory at node A, including optical pumping, storage and cooling. The experiment is repeated at a rate of 5 kHz.

pulse onto the atom, which is in two-photon resonance with the cavity[1]. The procedure of optical pumping and photon generation is performed twice. The first photon is intended to be stored in the atom of node A. The second photon is reflected off the cavity at node A without storage and serves as a reference to determine the storage efficiency. The photon generation efficiency into the cavity mode was measured to be 33 %. With a probability of 15 %, this photon is transmitted through the optics (including two fibers, the polarizer and the NPBS) to the cavity at node A.

Storage.   After optical pumping, the control laser at node A is switched on. As soon as the photon from node B enters the cavity at node A, the control intensity is ramped down. The temporal course of the Rabi-frequency follows approximately a $\cos^2$-function with a

---

[1]Details on optical pumping to $|2,0\rangle$ can be found in section 4.3.2 and [52].

total switching time of $\sim 0.5\,\mu s$. The timing of the control ramp is adjusted with respect to the arrival time of the photon and is optimized for maximum storage efficiency. During this stage, the polarization of the photon is mapped onto a superposition of the atomic Zeeman states $|2, \pm 1\rangle$ [Eq. (4.10)].

Readout.   After a chosen storage time of $2.5\,\mu s$, the control field is ramped up again and a single photon is generated. Thereby, the qubit stored in the atom is mapped back onto the polarization of the photon. Its polarization state is then detected and compared with the polarization of the original photon to analyze the fidelity of the quantum memory.

4.2.4. Experimental results

Efficiency

An important figure of merit of a quantum memory is the efficiency of the storage and retrieval process. We determine its value by comparing the number of read-out photons with the number of reference photons. Reference photons impinging onto the cavity enter the resonator and experience losses due to absorption and transmission through the high-reflective mirror. These photons leave the cavity from the high-transmissive mirror with a measured probability of 0.75. Transmission losses from the cavity to the detectors are the same for both, read-out photons and reference photons. The signal of the reference must therefore be scaled by the factor $1/0.75$.

Figure 4.4 shows the arrival-time histogram of photons for the quantum memory experiment. The data are integrated over a total measurement time of $\sim 12\,h$. The ratio of the counts from the read-out photon (within the depicted evaluation interval with a length of $1\,\mu s$) to the counts from the reference photon (blue bars) is measured to be $(14.1 \pm 0.8)\,\%$. Rescaling the reference counts by the factor of $1/0.75$ results in a storage-retrieval efficiency of $(10.6 \pm 0.7)\,\%$. This value is the probability for a single photon that is in front of the cavity to be stored, retrieved and to leave the cavity through the output coupler. This value therefore characterizes not only the efficiency of the storage-retrieval process in the atom, but of the whole memory, comprised of atom and cavity. With an independently measured photon production efficiency of $60\,\%$ at node A, the storage efficiency can be estimated to be $18\,\%$.

Fidelity

In order to determine the fidelity of the storage and retrieval process, we use a set of four input polarization states $|H\rangle$, $|V\rangle$, $|A\rangle$ and $|L\rangle$, and measure the corresponding photonic output density matrices using quantum state tomography (section 3.2). Under the assumption of a trace-preserving process, the Bloch sphere and the process matrix can be reconstructed by means of process tomography (Fig. 4.5). The average state fidelity with respect to the ideal input states is measured to be $\overline{\mathcal{F}} = (92.2 \pm 0.4)\,\%$, and clearly exceeds the value of $2/3$ that could be achieved by a classical intercept and resend method [101]. The dominant element in the process matrix is χ_{00}, representing the good preservation of
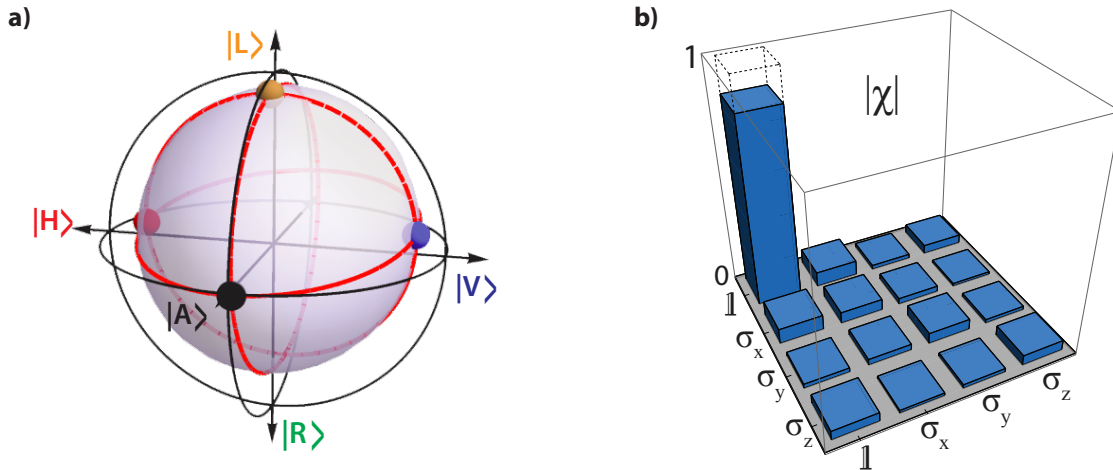
a)

b)

Figure 4.5.: Quantum process tomography of the single-atom quantum memory. The data are shown for the retrieved photons after storage in the atom. **a)** Reconstructed Bloch sphere. The small deformation of the unit sphere proves that the coherence of the polarization states is well-preserved during the storage and retrieval process. **b)** Absolute value of the elements of the corresponding process matrix. The dominant element χ_{00} indicates that the process is well described by the identity operation. The dashed bar corresponds to the matrix element of the identity operation ($\chi_{00} = 1$).

coherence during storage and readout. It can be seen from the reconstructed Bloch sphere that the measured output states are close to the ideal input states. The main deviation from the unit sphere (corresponding to an ideal quantum process) is a small loss in volume.

In the first demonstration of the single-atom quantum memory using weak coherent pulses, an average fidelity of 93 % was achieved [44]. After optimizing the process of optical pumping, this value could be increased to ≈ 98 %. The obtained fidelity for the measurement with single photons, however, is significantly smaller. This fact can be explained by the relatively low rate of detected photons after readout of the memory and resulting increased influence of non-perfect optical pumping to $F = 1$. The probability to detect a photon after storage and retrieval per experimental run is approximately $P_{\mathrm{p}} = 1 \cdot 10^{-3}$. This value results from the probabilities of the individual steps in the protocol, including photon generation at node B, transmission to the cavity at node A, storage and retrieval of the photon, and measurement in the single-photon detector. Occasionally it happens that after optical pumping, atom A remains in the hyperfine state $F = 2$. This may result in the generation of a photon in the readout process, which has a polarization independent of the incoming photon. The probability for this event to occur was measured by performing the experimental protocol as shown in Fig. 4.4 without an incoming photon. We find that with a probability of $P_{\mathrm{d}} = 1 \cdot 10^{-4}$ a signal in the detector is registered. As this is an experimentally determined value, it already includes electronic dark-counts that occur with a probability of $\approx 1.5 \cdot 10^{-5}$ within the 1 µs long evaluation interval. The percentage of detrimental events relative to events stemming from storing single photons is thus $P_{\mathrm{d}}/P_{\mathrm{p}} = 10$ %. By assuming that a photon generated from an atom that has not been properly optically pumped is randomly polarized, this results in a decrease of the fidelity by 5 percentage points. The low overall count rate can therefore explain the reduction
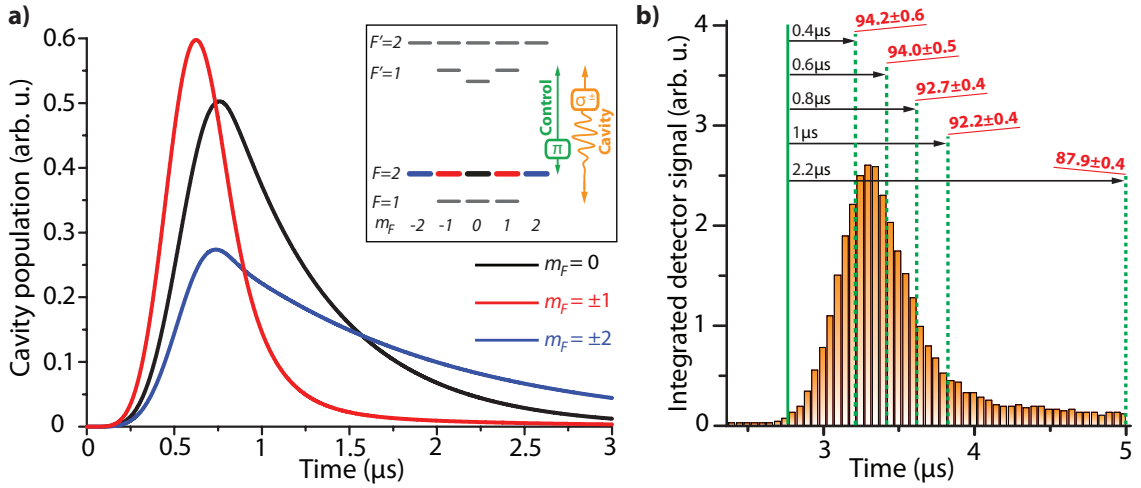
Figure 4.6.: Storage-retrieval fidelity for different evaluation intervals. **a)** Numerical simulations of the wave packet envelope of single photons generated into the cavity for different initial atomic states of the $F = 2$ manifold. The temporal evolution depends on the quantum number m_F. The inset shows the atomic levels and couplings used in the simulation (see Appendix C for details). The efficiencies are $70\,\%$ ($m_F = 0$), $48\,\%$ ($m_F = \pm 1$) and $56\,\%$ ($m_F = \pm 2$). **b)** Experimentally obtained fidelities for different subsets of the read-out photon data (cf. Fig. 4.4). By cutting the photon at earlier positions, the fidelity is increased.

of the fidelity compared to measurements with coherent pulses. This in turn means that the performance of the storage process with single photons compared to the previous demonstration with coherent pulses [44] is about the same.

The fidelity is limited by non-perfect optical pumping of atom A to the state $|1,0\rangle$ before storage. Off-resonant excitations of excited $F' = 0$ and $F' = 2$ states ultimately limit the quality of the pumping process. In addition, a not perfectly π-polarized laser causes deviations from the ideal transition scheme shown in Fig. 4.2. Both effects may lead to a preparation of the atom in the states $|1, \pm 1\rangle$. In the ideal storage scheme, the atom is transferred to a superposition of the states $|2, \pm 1\rangle$. The aforementioned imperfections, however, can result in the population of the other Zeeman states of the $F = 2$ manifold. The polarization of photons read out from these states is in general uncorrelated to the polarization of the stored photon. Non-ideal optical pumping thus reduces the measured storage-retrieval fidelity. Because the transition strength of the control field depends on the quantum number m_F, the dynamics of the photon emission process depends on the atomic state. This is illustrated with a simulation of the photon generation process[2], shown in Fig. 4.6a. Photons emitted from the states $|2, \pm 1\rangle$ have a nearly symmetric shape and represent the largest contribution to the measured read-out photons (see Fig. 4.4 and Fig. 4.6b). In contrast, population of the states $m_F = 0$ and $m_F = \pm 2$ leads to delayed photon emission. The reason is that the control field, which couples the states $F = 2$ and $F' = 1$, is near-resonant with respect to the excited states $|1, \pm 1\rangle'$ and is off-resonant to the states $|1,0\rangle'$ and $|2, \pm 2\rangle'$. By post-selecting subsets of data based on early photon arrival times it is therefore possible to filter out those events in which the atom was transferred

---

[2]Details on the simulation can be found in Appendix C.

to the states $|2,0\rangle$ or $|2,\pm 2\rangle$ during storage. As was discussed above, population of these states is caused by non-ideal optical pumping. The mentioned post selection therefore removes events in which initialization to $|1,0\rangle$ was not perfect. This filtering is demonstrated with data of the read-out photons of the storage experiment. The resulting fidelities for different evaluation intervals is shown in Fig. 4.6b. For example, by taking only $0.4\,\mu$s of the read-out photon into account, the fidelity has a value of $(94.2 \pm 0.6)\,\%$. By performing no post selection and taking $2.2\,\mu$s of the data into account, the measured fidelity is reduced to $(87.9 \pm 0.4)\,\%$. This clearly demonstrates that delayed photon emission leads to a decreased fidelity as expected from the discussion above.

4.3. Quantum state transfer between single atoms

In the previous section the reversible mapping of a quantum state between a single photon and a single atom with high fidelity was demonstrated. This process is the essential ingredient for a quantum network in which individual atomic nodes are connected via the exchange of photons. Such a connection between two individual atoms at distant locations is demonstrated in this chapter. Initially, the atom at node B holds a qubit $|\varphi\rangle_{\rm B}$. This state is mapped coherently to the polarization state of a single photon. The photon is then transmitted to the receiver at node A. At the receiving site, the polarization of the photon is mapped onto the internal atomic state and the transfer of the qubit $|\varphi\rangle_{\rm B}$ from atom B to atom A is thereby completed. This *direct quantum state transfer* between two remote atoms is demonstrated in the following.

The first part of this chapter explains how the atom at the sender site is prepared in a well-defined qubit state using a projective measurement. The second part covers the description of the experimental implementation. Finally, the efficiency and the fidelity of the state transfer is analyzed and discussed.

4.3.1. Initialization of the atomic qubit

To perform tomography of the state transfer process, we prepare atom B in a well-defined qubit state and analyze the transferred state at atom A using state tomography (see section 3.3). The qubit at node B can be written as a superposition of two states:

$$|\varphi\rangle_{\rm B} = \alpha\,|{\downarrow}\rangle_{\rm B} + \beta\,|{\uparrow}\rangle_{\rm B}\,, \quad |\alpha|^2 + |\beta|^2 = 1. \tag{4.11}$$

Physically, qubit B is encoded in the states $|{\downarrow}\rangle_{\rm B} \equiv |F = 1,m_F = -1\rangle_{\rm B}$ and $|{\uparrow}\rangle_{\rm B} \equiv |F = 1,m_F = +1\rangle_{\rm B}$ of the ^{87}Rb ground state $5S_{1/2}$. In order to prepare the state $|\varphi\rangle_{\rm B}$, first entanglement between the spin state of the atom and the polarization state of a single photon is generated. As a second step, this photon is measured in a polarization-sensitive detector. This heralds the projection of the atom onto a well-defined state. In the following, this preparation technique is described in detail.
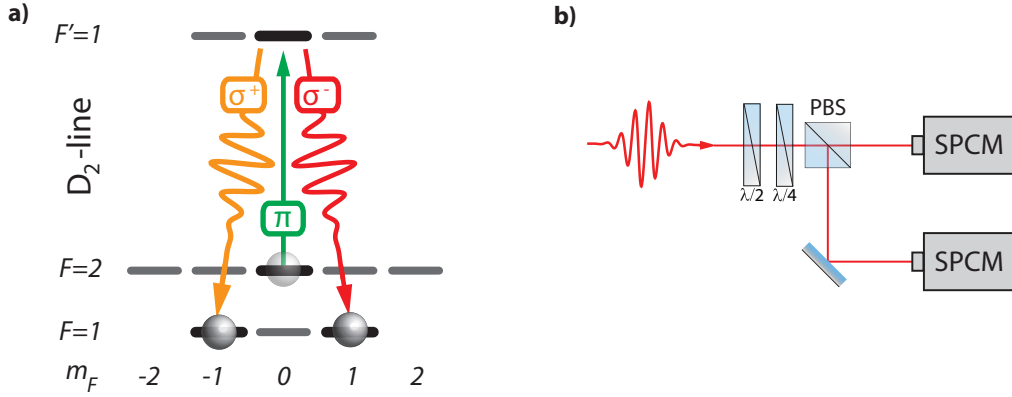
Figure 4.7.: Atomic state preparation via a projective measurement. a) Entanglement is generated between the spin state of a single atom and the polarization of a single photon. The atom is initialized in the state $|2,0\rangle$. A π-polarized control laser pulse near-resonant with the $F = 2 \leftrightarrow F' = 1$ transition drives an adiabatic passage along two possible paths ($\sigma^{\pm}$), thereby generating entanglement between the atomic Zeeman state and the photonic polarization. **b)** The photon is measured in a detection setup (see section 2.5). This projects the atom into a well-defined state, depending on the basis and the measurement outcome (Tab. 4.1).

4.3.1.1. Generation of atom-photon entanglement

The adiabatic passage described in section 4.1 can be exploited to efficiently create single photons that are entangled with the spin state of a single atom [52, 89, 98]. To this end, the scheme with three levels is extended to the configuration shown in Fig. 4.7a. The cavity is near-resonant with the $F = 1 \leftrightarrow F' = 1$ transition on the D_2-line[3]. Atom B is initially prepared in the state $|F = 2, m_F = 0\rangle$. Application of a π-polarized control field that is on two-photon resonance with the cavity ($\Delta_C = \Delta_L$) couples this state to $|F = 1, m_F = 0\rangle'$. This drives an adiabatic passage and consequently the emission of a single photon B' from the cavity. There are two equally probable and indistinguishable paths for the passage. The first one is the transfer to the atomic $|1, -1\rangle$ state while emitting a $|\circlearrowleft\rangle$ photon, the second one is the transfer to the state $|1, +1\rangle$ upon emission of a $|\circlearrowright\rangle$ photon. This results in a superposition of the two paths and therefore the maximally entangled Bell state

$$\left|\Psi_{B\otimes B'}^{-}\right\rangle = \frac{1}{\sqrt{2}}\left(|\downarrow\rangle_B |\circlearrowleft\rangle_{B'} - |\uparrow\rangle_B |\circlearrowright\rangle_{B'}\right), \tag{4.12}$$

between the internal state of the atom and the polarization of the photon. The relative phase between the two terms is given by the Clebsch-Gordan coefficients of the involved atomic transitions.

---

[3]The scheme to generate entanglement works for both, the D_1 and the D_2-line [52]. In the experiments described here, the D_2-line is used for the generation of entanglement due to its higher coupling strengths on the relevant transitions.

4.3.1.2. Projective measurement

The photon B$'$ is sent to a detection setup (see Fig. 4.7b), where it is registered in one of the two single-photon detectors. Let $|\varphi_d\rangle = \alpha_d |\circlearrowright\rangle + \beta_d |\circlearrowleft\rangle$ describe the state that is measured by one of the detectors. The parameters α_d and β_d are set by the orientation of the waveplates in front of the polarizing beam splitter (see Tab. 4.1). For example, the state H corresponds to $\alpha_d = \beta_d = 1/\sqrt{2}$. A registered photon in the detector that corresponds to the state $|\varphi_d\rangle$ projects $\left|\Psi^-_{\mathrm{B}\otimes\mathrm{B}'}\right\rangle$ onto (after renormalization):

$$(\alpha_d^* \langle\circlearrowright| + \beta_d^* \langle\circlearrowleft|) \left|\Psi^-_{\mathrm{B}\otimes\mathrm{B}'}\right\rangle \longrightarrow \beta_d^* |\downarrow\rangle_\mathrm{B} - \alpha_d^* |\uparrow\rangle_\mathrm{B} \equiv |\varphi\rangle_\mathrm{B}. \tag{4.13}$$

The density matrix of the state $|\varphi\rangle_\mathrm{B}$ in terms of α_d and β_d reads:

$$|\varphi\rangle_\mathrm{B} \langle\varphi|_\mathrm{B} = \begin{pmatrix} |\beta_d|^2 & -\alpha_d^*\beta_d \\ -\alpha_d\beta_d^* & |\alpha_d|^2 \end{pmatrix}. \tag{4.14}$$

A registered photon in one of the detectors thus heralds the preparation of a well-defined atomic state (see Tab. 4.1). As the outcome of the measurement is random and the detection efficiency is smaller than 1, this preparation is a probabilistic process.

Obviously, the quality of the preparation stage depends on the fidelity of the entangled atom-photon state. To find a relation between the fidelity of the initially entangled atom-photon state and the fidelity of the atomic state prepared by the projective measurement, we assume that a non-unity fidelity of the entangled state can be described by a partially mixed state. The density matrix of the atom-photon state ρ_ent then reads

$$\rho_\mathrm{ent} = p_\mathrm{ent} \left|\Psi^-_{\mathrm{B}\otimes\mathrm{B}'}\right\rangle \left\langle\Psi^-_{\mathrm{B}\otimes\mathrm{B}'}\right| + \frac{1}{4}(1 - p_\mathrm{ent}) \mathbb{1}_4. \tag{4.15}$$

p_ent is the probability that the entangled state is the ideal, maximally entangled Bell state $\left|\Psi^-_{\mathrm{B}\otimes\mathrm{B}'}\right\rangle$. The entanglement fidelity with respect to the ideal state is then

$$\mathcal{F}_\mathrm{ent} = \left\langle\Psi^-_{\mathrm{B}\otimes\mathrm{B}'}\right| \rho_\mathrm{ent} \left|\Psi^-_{\mathrm{B}\otimes\mathrm{B}'}\right\rangle = \frac{1}{4} + \frac{3}{4}p_\mathrm{ent}. \tag{4.16}$$

We are interested in the atomic state after the photonic part of ρ_ent has been measured. The density matrix of the projected system, ρ_m, can be calculated using the formula[4] [56]

$$\rho_\mathrm{m} = \frac{P_\mathrm{m}\rho_\mathrm{ent}P_\mathrm{m}}{\mathrm{Tr}\,[P_\mathrm{m}\rho_\mathrm{ent}]}, \tag{4.17}$$

where P_m is a Hermitian operator that describes the measurement. It is a projection operator that acts on the state space of the system being measured. Here, the photonic part of ρ_ent is measured to be in the state $|\varphi_d\rangle$, while the atomic part is left unaffected. The operator P_m for the total system is thus

$$P_\mathrm{m} = \mathbb{1}_2 \otimes |\varphi_d\rangle \langle\varphi_d|. \tag{4.18}$$

---

[4] After projection of the atom-photon state the photon is destroyed. The calculation of ρ_m, however, assumes the photon being in the eigenstate of the measurement operator. The correct result for the atomic state is obtained after taking the partial trace in Eq. (4.20).

Polarization	α_d	β_d	Atomic qubit
R ($\circlearrowright$)	1	0	$\lvert\uparrow\rangle$
L ($\circlearrowleft$)	0	1	$\lvert\downarrow\rangle$
H	$1/\sqrt{2}$	$1/\sqrt{2}$	$\lvert\uparrow_{\mathrm{x}}\rangle = \frac{1}{\sqrt{2}}\left(\lvert\downarrow\rangle - \lvert\uparrow\rangle\right)$
V	$1/\sqrt{2}$	$-1/\sqrt{2}$	$\lvert\downarrow_{\mathrm{x}}\rangle = \frac{1}{\sqrt{2}}\left(\lvert\downarrow\rangle + \lvert\uparrow\rangle\right)$
D	$1/\sqrt{2}$	$i/\sqrt{2}$	$\lvert\downarrow_{\mathrm{y}}\rangle = \frac{1}{\sqrt{2}}\left(\lvert\downarrow\rangle + i\lvert\uparrow\rangle\right)$
A	$1/\sqrt{2}$	$-i/\sqrt{2}$	$\lvert\uparrow_{\mathrm{y}}\rangle = \frac{1}{\sqrt{2}}\left(\lvert\downarrow\rangle - i\lvert\uparrow\rangle\right)$

Table 4.1.: Outcome of the polarization measurement and resulting atomic state after projecting the entangled state of Eq. (4.12) according to Eq. (4.13).

Evaluating the expression from Eq. (4.17) results in

$$
\rho_{\mathrm{m}} = p_{\mathrm{ent}} \begin{pmatrix} |\alpha_d|^2|\beta_d|^2 & \alpha_d\beta_d^*|\beta_d|^2 & -\alpha_d\beta_d^*|\alpha_d|^2 & -\alpha_d^2(\beta_d^*)^2 \\ \alpha_d^*\beta_d|\beta_d|^2 & |\beta_d|^4 & -|\alpha_d|^2|\beta_d|^2 & -\alpha_d\beta_d^*|\beta_d|^2 \\ -\alpha_d^*\beta_d|\alpha_d|^2 & -|\alpha_d|^2|\beta_d|^2 & |\alpha_d|^4 & \alpha_d\beta_d^*|\alpha_d|^2 \\ -(\alpha_d^*)^2\beta_d^2 & -\alpha_d^*\beta_d|\beta_d|^2 & \alpha_d^*\beta_d|\alpha_d|^2 & |\alpha_d|^2|\beta_d|^2 \end{pmatrix}
$$
$$
+ \frac{1}{4}(1 - p_{\mathrm{ent}})\left[\mathbb{1}_2 \otimes \lvert\varphi_d\rangle\langle\varphi_d\rvert\right], \tag{4.19}
$$

where the matrix is written in the basis $\{\lvert\downarrow\circlearrowleft\rangle, \lvert\downarrow\circlearrowright\rangle, \lvert\uparrow\circlearrowleft\rangle, \lvert\uparrow\circlearrowright\rangle\}$. Because we are only interested in the atomic part of the state, we have to take the partial trace over the photonic subsystem:

$$
\rho_{\mathrm{B}} = \mathrm{Tr}_{\mathrm{B}'}\left[\rho_{\mathrm{m}}\right] = p_{\mathrm{ent}} \begin{pmatrix} |\beta_d|^2 & -\alpha_d^*\beta_d \\ -\alpha_d\beta_d^* & |\alpha_d|^2 \end{pmatrix} + \frac{1}{2}(1 - p_{\mathrm{ent}})\mathbb{1}_2
$$
$$
= p_{\mathrm{ent}}\lvert\varphi\rangle_{\mathrm{B}}\langle\varphi\rvert_{\mathrm{B}} + \frac{1}{2}(1 - p_{\mathrm{ent}})\mathbb{1}_2. \tag{4.20}
$$

The fidelity with respect to the state $\lvert\varphi\rangle_{\mathrm{B}}$ finally becomes

$$
\mathcal{F}_{\mathrm{sp}} = \mathrm{Tr}\left[\lvert\varphi\rangle_{\mathrm{B}}, \rho_{\mathrm{B}}\right] = \frac{1}{4}\left(3p_{\mathrm{ent}} + 1\right) = \frac{1}{3}\left(2\mathcal{F}_{\mathrm{ent}} + 1\right). \tag{4.21}
$$

The result is a simple linear relation between the entanglement fidelity and the state fidelity.

4.3.2. Experimental sequence and implementation

In this section, the individual steps to realize the direct quantum state transfer are described (see Fig. 4.8 and Fig. 4.9). Each experimental run starts with the probabilistic loading of single atoms from a MOT into the cavity in both systems. As soon as a single atom is present in each cavity the protocol is started.

State preparation at node B

The atomic qubit at node B is initialized using the probabilistic scheme described in section 4.3.1. To generate entanglement between the atom and a photon, preparation of the atom in the state $\lvert 2,0\rangle$ is required. This is achieved by optical pumping. A π-polarized laser that is near-resonant with the $F = 2 \leftrightarrow F' = 2$ transition on the D_1-line pumps the atom to
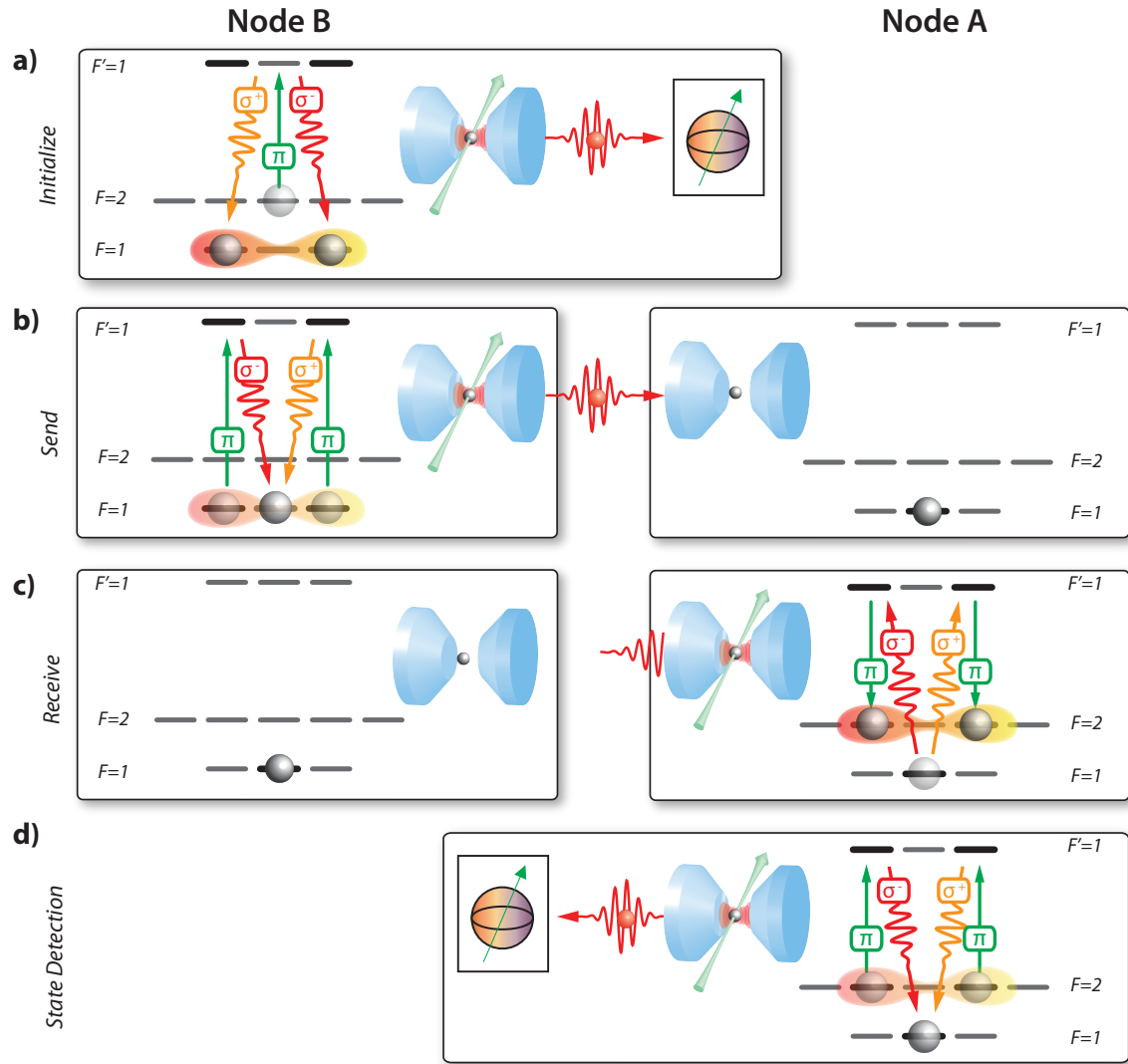
Figure 4.8.: Protocol to demonstrate the direct quantum state transfer. a) At node B, a qubit is encoded in the states $|\downarrow\rangle_B \equiv |1,-1\rangle_B$ and $|\uparrow\rangle_B \equiv |1,+1\rangle_B$ of a single atom. State preparation is achieved using a projective measurement. **b)** The qubit is mapped onto the polarization of a single photon, which is sent to node A. **c)** The photonic polarization is mapped onto a superposition of Zeeman states of atom A, thereby completing the quantum state transfer between the atoms. **d)** Atomic state detection of atom A is performed by mapping the internal state onto the polarization of a photon which is subsequently detected.

the desired state: Because the transition $|2,0\rangle \leftrightarrow |2,0\rangle'$ is not allowed according to dipole selection-rules [100], population accumulates in $|2,0\rangle$. As the $F=2 \leftrightarrow F'=2$ transition is not closed, population can also decay to $F=1$. Another laser that is near-resonant with the $F=1 \leftrightarrow F'=2$ transition on the D_2-line serves as a repumper. The cavity and the control field are $170\,\text{MHz}$ blue detuned with respect to the transition of the free atom. Because the atom experiences a Stark shift of $120\,\text{MHz}$ in the present standing-wave trap,
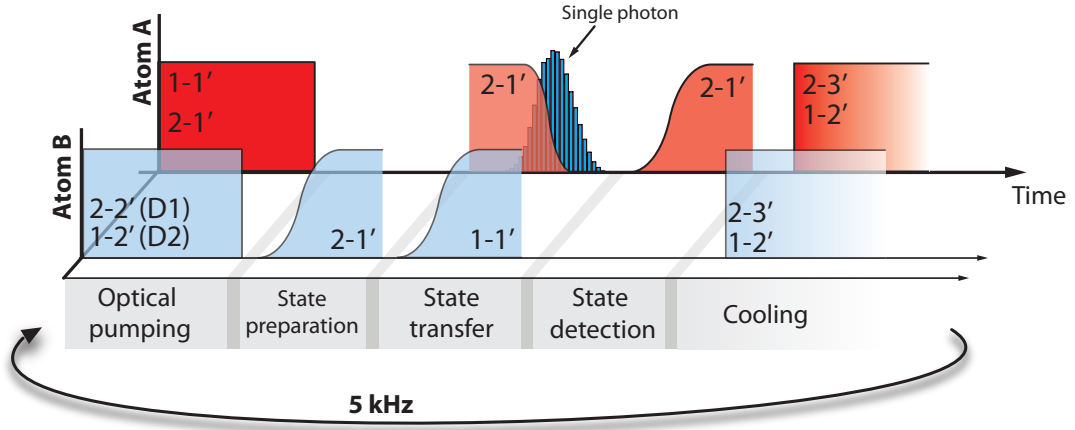
Figure 4.9.: Schematic of the experimental sequence for the demonstration of the direct state transfer. First, the individual atoms are prepared in the states $|1,0\rangle$ (node A) and $|2,0\rangle$ (node B) using optical pumping. The atomic qubit at node B is then initialized by generating atom-photon entanglement and subsequent detection of the photon. This state is mapped onto a photon, which is coherently absorbed in atom A. The state of atom A is detected by mapping its state onto the polarization of another single photon. After each experimental sequence, a cooling interval ($\approx 150\,\mu s$) is applied to the atoms.

the control laser and cavity resonance are effectively $50\,\mathrm{MHz}$ blue detuned from the atom. The fields used for optical pumping are blue detuned by approximately $20\,\mathrm{MHz}$.

Following optical pumping a π-polarized control laser pulse, coupling the $F = 2 \leftrightarrow F' = 1$ states of the D_2-line, is applied to the atom and triggers the generation of a single photon in the cavity and ideally results in the entangled state of Eq. (4.12). The photonic part of this state is measured in a polarization-sensitive detection setup (Fig. 4.8a). The outcome of this measurement heralds the successful preparation of the atom in a well-defined state (see Tab. 4.1).

The fidelity of the preparation can be estimated by measuring the entanglement fidelity and using Eq. (4.21). We achieve this by mapping the atom-photon entanglement onto a photon-photon entanglement [52, 89, 98]. The application of a π-polarized laser pulse coupling the states $F = 1 \leftrightarrow F' = 1$ drives a vSTIRAP and triggers the emission of another photon. The photons are detected in three different polarization bases. Correlating these measurement results allows us to determine the entanglement witness and therefore the fidelity with the $|\Psi^-\rangle$ Bell state (see section 3.5). We find an average value of $\mathcal{F}_{\mathrm{ent}} = 93\,\%$, corresponding to a fidelity of the initial state of $\mathcal{F}_{\mathrm{B}} = 95\,\%$.

Optical pumping at node A

Atom A is initialized in state $|1,0\rangle$ using the procedure described in section 4.2.3. The fidelity of the quantum memory is determined by storing and retrieving weak coherent pulses with a mean photon number of 1 [44]. Measurements with a set of well-defined polarization states allow us to perform process tomography of the storage and retrieval process, as was done with single photons in section 4.2 [44, 59]. The use of coherent pulses

to analyze the performance of the memory is much more convenient than the use of single photons. The average fidelity over the measurement time of ~ 12 hours is found to be $\mathcal{F}_{\mathrm{s}} = 95\,\%$.

Quantum state transfer

We apply another adiabatic passage using a π-polarized control laser pulse that is near-resonant with the $F = 1 \leftrightarrow F' = 1$ transition and in resonance with the cavity field at node B. This maps the atomic qubit of node B onto the polarization of a single photon (Fig. 4.8b):

$$\alpha \left| \downarrow \right\rangle_{\mathrm{B}} + \beta \left| \uparrow \right\rangle_{\mathrm{B}} \quad \longrightarrow \quad \alpha \left| \circlearrowright \right\rangle + \beta \left| \circlearrowleft \right\rangle .$$

This process leaves the atom in state $\left| 1,0 \right\rangle$. The mapping process is the same as we use to characterize the fidelity of the entangled state (see above). The quality of this process is thus included in the aforementioned fidelity of $\mathcal{F}_{\mathrm{B}} = 95\,\%$. The photon is sent to atom A via the optical fiber. As soon as it enters the cavity of node A, the power of the control field is ramped down to zero. The temporal course of the control power follows approximately a $\cos^2$-shape with a total switching time of $\sim 1\mu$s. This drives a STIRAP and coherently maps the photon onto the atom, thereby completing the transfer of the quantum state (Fig. 4.8c).

State detection

To verify the state transfer, the state of atom A is read out by mapping it onto the polarization of another single photon (Fig. 4.8d). This enables us to measure the atomic quantum state by detecting the photon in a polarization-sensitive detection setup. To perform complete quantum process tomography, we compare the set of six states $\{ \left| \mathcal{B}_i \right\rangle \} = \{ \left| \downarrow \right\rangle , \left| \uparrow \right\rangle , \left| \downarrow_{\mathrm{x}} \right\rangle , \left| \uparrow_{\mathrm{x}} \right\rangle , \left| \downarrow_{\mathrm{y}} \right\rangle , \left| \uparrow_{\mathrm{y}} \right\rangle \}$, initially prepared at node B and forming three mutually unbiased bases, with the read-out states from node A (see section 3.3).

State preparation and state detection are performed in independent detection setups (see Fig. 4.12). To prepare the input states, we switch between three different settings of the measurement basis in detection setup 2: $H/V, D/A$ and R/L. A first photon emitted from node B and registered in one of the detectors heralds the initialization of the atomic qubit B in a well-defined state (see section 4.3.1 and Tab. 4.1). To reconstruct the state of the atomic qubit at node A after the state transfer is finished, we perform complete state tomography by measuring the read-out photons from node A in three different bases ($H/V, D/A$ and R/L) in detection setup 1. Thus, measurements of nine different combinations of the bases in the two detection setups are required.

4.3.3. Experimental setup

As becomes clear from the steps involved in the protocol, the first photon from node B, enabling the initialization of the atomic qubit, must be directed to a detection setup, while the second photon must be coupled into the cavity of node A. Additionally, a photon from
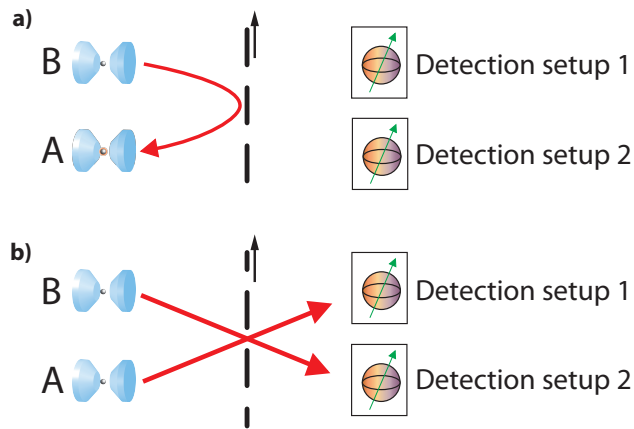
Figure 4.10.: Principle of the mechanical switch. a) State in which the two cavity nodes are directly connected. **b)** State in which the output modes of the cavities are connected to separate detection setups.

node A that is used for state detection must be directed to another detection setup. To this end, a fast-moving mirror is used to switch the network between two configurations. The network nodes are either connected directly by a fiber path or the nodes are disconnected and photons coming from each node are guided to separate detection setups. The principle is illustrated in Fig. 4.10.

To implement a mirror that is able to switch between the two configurations within a few microseconds, we use a commercially available computer hard disk [102]. Equidistant slits with a rectangular shape are milled close to the edge of the disk (see Fig. 4.11a). The disk is gold coated such that the remaining bars between the slits reflect impinging light efficiently. Because the disk rotates at a constant speed of 7200 revolutions per minute, the length of the bars determines the time during which the disk is in the "reflecting mode". It is chosen such that this time is ≈ 5 µs. Adjacent bars have a temporal distance of 200 µs. This allows us to run the experimental protocol at a rate of 5 kHz. The temporal dependence of the reflection properties of the disk is shown in Fig. 4.11b. The reflected light is detected at the output of a fiber. Therefore, the measured reflection already includes the fiber coupling efficiency. The different colors correspond to light reflected from a set of randomly chosen bars. The slight variations in the length of the bars are due to imperfections during manufacturing of the slits. They are, however, small compared to the average length of
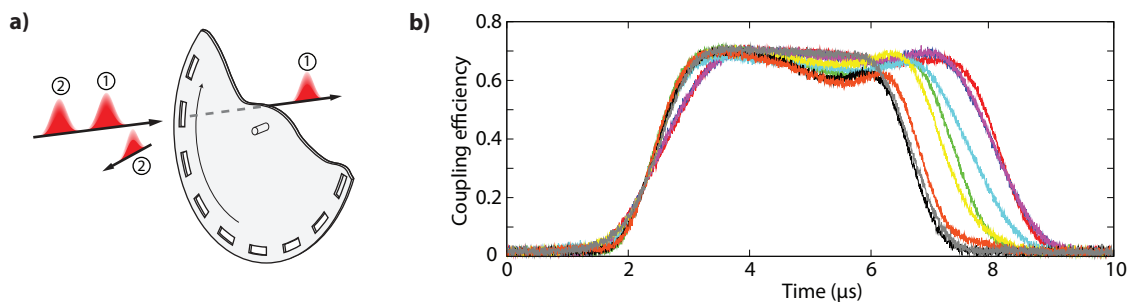

Figure 4.11.: A fast-moving mirror based on a computer hard disk. a) Sketch of the rotating disk. A first photon is transmitted through a slit, a second, later one is reflected off one of the bars. **b)** Fiber coupling efficiency (including reflection) for different bars of the disk. The disk rotates at a speed of 7200 revolutions per minute.
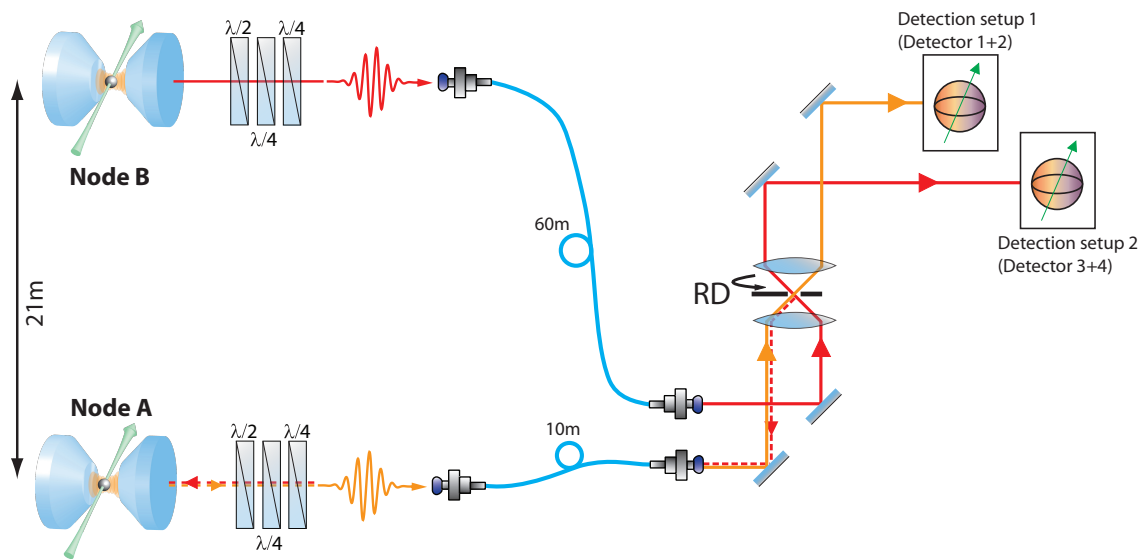
Figure 4.12.: Experimental setup used to perform the direct quantum state transfer.
A single photon that is entangled with atom B is measured in detection setup 2 (solid red line).
This projects atom B into a well-defined state. This state is mapped onto the polarization of
another single photon that is transmitted to the cavity at node A and coherently absorbed in the
atom (dashed red line). To measure the state of atom A after the state transfer is completed, a
vSTIRAP maps this state onto the polarization of a photon, which is measured in detection setup 1
(orange line). Waveplates ($\lambda/2, \lambda/4$) are used to compensate for unwanted polarization rotations.
RD: Rotating disk that serves as a fast-moving mirror (cf. Fig. 4.11).

the bars. The differences of the measured reflection as a function of time are caused by
the surface of the disk not being perfectly flat. The average coupling efficiency (including
reflection off the disk) is $\approx 60\,\%$ and, most importantly, no polarizing effects could be
observed. A light barrier, made up of an auxiliary laser and a photodiode, generates a
digital signal that is used to trigger the experimental sequence in both laboratories. This
ensures that the experiments are synchronized with respect to the state of the rotating
disk.

A detailed sketch of the setup that is used to connect the two laboratories and to perform
the projective state preparation and state detection is shown in Fig. 4.12. Compensation of
unwanted polarization rotations is performed using waveplates as was explained in section
4.2.2. The polarization behind the cavity at node B must match the polarization in front of
the cavity at node A and the polarization in front of detection setup 2. At the same time,
the polarization behind the cavity at node A must be the same as in front of detection
setup 1.

4.3.4. Experimental results

Efficiency

The probability of the state transfer to succeed is given by the probability to generate a single photon at node B, and to transmit it to and store it at node A. η_B is the efficiency for the generation of a single photon into the cavity mode of node B, and S is the probability of atom A to coherently absorb a photon that impinges onto the cavity. Conditioned on the successful initialization of atom B (see section 4.3.1), the probability P_trans to transfer the state of atom B to atom A is

$$P_\mathrm{trans} = \eta_\mathrm{B} T_\mathrm{out} T_\mathrm{AB} S, \tag{4.22}$$

where $T_\mathrm{out} = 0.9$ is the directionality of the cavity and T_AB is the transmission probability between the cavities. While the photon generation efficiency η_B and the transmission T_AB can easily be inferred from independent measurements, determination of the storage efficiency S is tricky. Because of the fast-moving mirror, a reference photon as in the memory experiment described in section 4.2.4 cannot be used. Therefore, the storage efficiency S must be calculated indirectly. This is done by tracing back the storage efficiency to quantities that are experimentally accessible.

The photon that is entangled with atom B and used for state preparation is generated with an efficiency η_B1. The probability η_B1^D to detect this first photon in detection setup 2 is

$$\eta_\mathrm{B1}^D = \eta_\mathrm{B1} T_\mathrm{out} \varepsilon_\mathrm{B}^D, \tag{4.23}$$

with ε_B^D being the probability to detect a single photon that has left the cavity. ε_B^D includes transmission losses and the quantum efficiency of the detectors. After the state transfer, the state of atom A is read out by mapping it onto the polarization of a photon. The overall probability to detect a read-out photon from atom A is

$$\eta_\mathrm{A}^D = P_\mathrm{trans} \eta_\mathrm{A} T_\mathrm{out} \varepsilon_\mathrm{A}^D. \tag{4.24}$$

After a successful state transfer (with probability P_trans), the atom-photon state mapping results in the generation of a single photon with efficiency η_A. The photon is eventually detected with a probability of ε_A^D. A quantity that can be measured is the ratio $\eta_\mathrm{A}^D/\eta_\mathrm{B1}^D$, as both, the read-out photon from node A as well as the photon from node B used for state preparation, are registered by the single-photon detectors:

$$\frac{\eta_\mathrm{A}^D}{\eta_\mathrm{B1}^D} = \frac{\eta_\mathrm{B} T_\mathrm{out} T_\mathrm{AB} S \eta_\mathrm{A} \varepsilon_\mathrm{A}^D}{\eta_\mathrm{B1} \varepsilon_\mathrm{B}^D} \quad \Leftrightarrow \quad S = \frac{\eta_\mathrm{A}^D}{\eta_\mathrm{B1}^D} \frac{\eta_\mathrm{B1} \varepsilon_\mathrm{B}^D}{\eta_\mathrm{B} \eta_\mathrm{A} \varepsilon_\mathrm{A}^D T_\mathrm{out} T_\mathrm{AB}}. \tag{4.25}$$

Using the values given in Table 4.2 and $\eta_\mathrm{A}^D/\eta_\mathrm{B1}^D = 4.2 \cdot 10^{-3}$, the storage efficiency is calculated to be $S = 22.5\,\%$. With the help of Eq. (4.22), we then find the probability for a state transfer to succeed to be $P_\mathrm{trans} = 0.24\,\%$.

It must be noted that the Rabi frequency of the control field used to read out atom B, and consequently the value of η_B, is deliberately kept low to suppress off-resonant excitations to the nearby state $|0,0\rangle'$. This state is only $72\,\mathrm{MHz}$ detuned from the transition

Quantity	Value	Meaning
η_{B1}	0.4	Generation efficiency of photon 1 at node B.
η_{B}	0.03	Generation efficiency of photon 2 at node B.
η_{A}	0.6	Generation efficiency of the read-out photon at node A.
$\varepsilon_{\mathrm{B}}^{D}$	0.34	Detection efficiency at node B. Includes fiber coupling, transmission losses and quantum efficiency of the detectors.
$\varepsilon_{\mathrm{A}}^{D}$	0.39	Detection efficiency at node A. Includes fiber coupling, transmission losses and quantum efficiency of the detectors.
T_{out}	0.9	Outcoupling efficiency of the cavities into one single mode.
T_{AB}	0.4	Transmission between node B and A. Measured from before fiber input at node B to fiber output at node A. Includes reflection off the fast-moving mirror.

Table 4.2.: Efficiencies for the individual steps involved in the state transfer experiment.

$F = 1 \leftrightarrow F' = 1$, which is addressed by the control laser to generate the photon (see Appendix A). It could therefore happen that accidentally randomly polarized photons are emitted, which would then spoil the measured fidelity. The comparatively low generation efficiency reduces the state-transfer probability in the current implementation.

As the experiment is repeated at a rate of $f_{\mathrm{rep}} = 5\,\mathrm{kHz}$, the state transfer efficiency could theoretically allow for a rate of transferred states of approximately $10\,\mathrm{Hz}$. Taking into account that not always a single atom is present in both labs, this rate is reduced. For the current data that were taken over $\sim 18\,\mathrm{h}$, the combined duty cycle (that is the fraction of time during which a single atom is trapped and localized at the center of the cavity mode of both nodes) was measured to be $D \approx 0.2$. This results in an effective rate for the state transfer of 2 per second.

The above calculation assumes that atom B has already been initialized by projective state preparation. This requires the generation and detection of one single photon from atom B. The probability of this preparation stage is given by $P_{\mathrm{prep}} = \eta_{\mathrm{B1}} T_{\mathrm{out}} \varepsilon_{\mathrm{B}}^{D} = 12\,\%$. After the state transfer is finished, the state of atom A is read out by mapping its spin state onto the polarization of another photon, which is subsequently detected. The probability of the state detection is $P_{\mathrm{det}} = \eta_{\mathrm{A}} T_{\mathrm{out}} \varepsilon_{\mathrm{A}}^{D} = 21\,\%$. The probability of a successfully verified attempt, each consisting of state preparation at node B, quantum state transfer and state detection at node A is $P_{\mathrm{c}} = P_{\mathrm{prep}} P_{\mathrm{trans}} P_{\mathrm{det}} = 6 \cdot 10^{-5}$. The overall rate of verified attempts is then $P_{\mathrm{c}} D \cdot 5\,\mathrm{kHz} \approx 3$ per minute.

Fidelity

The crucial benchmark for any qubit state transfer is that the qubit at the sender site has a large fidelity with the qubit at the receiver site. The individual fidelities of the output states with the set of six ideal input states $\{|\mathcal{B}_i\rangle\}$ are listed in Tab. 4.3. The average state fidelity is found to be $\overline{\mathcal{F}} = (83.7 \pm 0.9)\,\%$.

Using the reconstructed output states, we perform complete process tomography (section

Input state	Fidelity (%)
$\vert\downarrow\rangle$	85.1 ± 2.3
$\vert\uparrow\rangle$	85.2 ± 2.3
$\vert\downarrow_{\mathrm{y}}\rangle = \frac{1}{\sqrt{2}}\left(\vert\downarrow\rangle + i\vert\uparrow\rangle\right)$	78.9 ± 2.2
$\vert\uparrow_{\mathrm{y}}\rangle = \frac{1}{\sqrt{2}}\left(\vert\downarrow\rangle - i\vert\uparrow\rangle\right)$	86.0 ± 1.8
$\vert\downarrow_{\mathrm{x}}\rangle = \frac{1}{\sqrt{2}}\left(\vert\downarrow\rangle + \vert\uparrow\rangle\right)$	83.2 ± 2.3
$\vert\uparrow_{\mathrm{x}}\rangle = \frac{1}{\sqrt{2}}\left(\vert\downarrow\rangle - \vert\uparrow\rangle\right)$	83.5 ± 2.2
Average	$\mathbf{83.7 \pm 0.9}$

Table 4.3.: Individual state fidelities of atom A after state transfer for six mutually unbiased input states of node B. The quoted errors are the statistical standard error.

3.3). The resulting Bloch sphere, visualizing the effect of the process on arbitrary input states, and the process matrix χ are shown in Fig. 4.13. The process fidelity that we obtain from a maximum-likelihood fit is $\mathcal{F}_{\mathrm{proc}} = \chi_{00} = 75.5\,\%$. This corresponds to an average state fidelity of $83.7\,\%$, which is in excellent agreement with $\overline{\mathcal{F}}$ obtained from the individual states. This proves the very good quality of the fit. The fidelity clearly exceeds the classical threshold of $2/3$.

The measured fidelity contains imperfections of the individual steps used to perform and analyze the direct state transfer. Non-perfect state preparation at node B and unwanted events during state detection at node A, caused by non-perfect optical pumping and detector dark counts, reduce the measured value. To estimate the influence of these two imperfections on the total fidelity, we assume that the initially prepared state at node B, ρ_{B}, can be expressed as a partially mixed state

$$\rho_{\mathrm{B}} = p_{\mathrm{B}}\,\vert\varphi\rangle\,\langle\varphi\vert + \frac{1}{2}(1 - p_{\mathrm{B}})\mathbb{1}_2, \qquad (4.26)$$

with p_B being the probability that the ideal state $\vert\varphi\rangle$ has been prepared. The state fidelity is $\mathcal{F}_{\mathrm{B}} = \langle\varphi\vert\,\rho_{\mathrm{B}}\,\vert\varphi\rangle = \frac{1}{2}\left(p_{\mathrm{B}} + 1\right)$. The storage process of this state in atom A is now modeled as follows: The memory transforms the pure part of Eq. (4.26) into the partially mixed state $\rho = p_{\mathrm{s}}\,\vert\varphi\rangle\,\langle\varphi\vert + \frac{1}{2}(1 - p_{\mathrm{s}})\mathbb{1}_2$, with the probability for perfect storage p_{s} being related to the fidelity of the memory by $\mathcal{F}_{\mathrm{s}} = \frac{1}{2}\left(p_{\mathrm{s}} + 1\right)$. The mixed part of the input state remains mixed after storage and retrieval from the memory. The photonic output state of the memory at node A then becomes

$$\rho_{\mathrm{out}} = p_{\mathrm{B}}p_{\mathrm{s}}\,\vert\varphi\rangle\,\langle\varphi\vert + \frac{1}{2}(1 - p_{\mathrm{B}}p_{\mathrm{s}})\mathbb{1}_2. \qquad (4.27)$$

As was explained in section 4.2.4, with a probability of $P_{\mathrm{d}} = 10^{-4}$ a photon with random polarization is registered during state detection of atom A. The reason is non-perfect optical pumping at node A, where the atom remains in the ground state $F = 2$. This may lead to the production of a photon during readout even when no photon was stored. P_{d} also includes electronic dark-counts. The probability for a joint occurrence between this deleterious event and a photon being detected during state preparation[5], which heralds

---

[5]The probabilities for correlated detections between an electronic dark-count during state preparation and a signal during state detection, as well as correlations between two dark-counts are several orders of magnitude smaller and are therefore neglected.
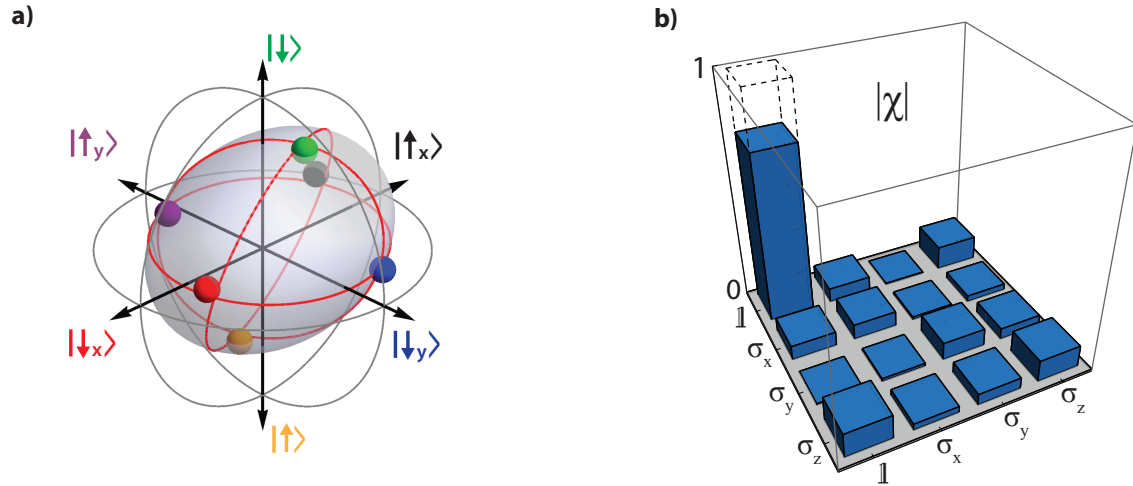
a)

b)

Figure 4.13.: Quantum process tomography results. The figure shows two equivalent representations of the tomography result. **a)** Visualization of the process in Stokes space. The sphere shows the effect of the process on arbitrary input states. The colored spheres correspond to the reconstructed output states for the six input states $\{|\mathcal{B}_i\rangle\}$. **b)** Reconstructed process matrix χ. The dominant element is χ_{00}. The dashed bar corresponds to the matrix element of the ideal process ($\chi_{00} = 1$).

the successful initialization, is $P_{\mathrm{d}}P_{\mathrm{prep}} = 1.2 \cdot 10^{-5}$. As derived above, the probability for the occurrence of an event that is taken into account for evaluation is $P_{\mathrm{c}} = 6 \cdot 10^{-5}$. The percentage of spurious events is therefore $p_{\mathrm{d}} = P_{\mathrm{d}}P_{\mathrm{prep}}/P_{\mathrm{c}} = 20\,\%$. The output state is accompanied by these random events and the detected state thus is

$$\rho_{\mathrm{det}} = p_{\mathrm{B}}p_{\mathrm{s}}(1 - p_{\mathrm{d}})\,|\varphi\rangle\langle\varphi| + \frac{1}{2}\left[(1 - p_{\mathrm{B}}p_{\mathrm{s}}(1 - p_{\mathrm{d}}))\right]\mathbb{1}_2. \tag{4.28}$$

The independently measured values $\mathcal{F}_{\mathrm{B}} = 95\,\%$ and $\mathcal{F}_{\mathrm{s}} = 95\,\%$ (see section 4.3.2) correspond to $p_{\mathrm{B}} = p_{\mathrm{s}} = 0.9$. The fidelity of the state ρ_{det} is $\mathcal{F}_{\mathrm{det}} = \langle\varphi|\,\rho_{\mathrm{det}}\,|\varphi\rangle = \frac{1}{2}\left(p_{\mathrm{B}}p_{\mathrm{s}}(1 - p_{\mathrm{d}}) + 1\right) = 82.4\,\%$ and agrees very well with the measured average state fidelity of $\overline{\mathcal{F}} = 83.7\,\%$.

As was already discussed in section 4.2.4 for the quantum memory experiment, the fidelity may be increased by improving the process of optical pumping at both nodes. First, this would enhance the fidelity of the storage and retrieval process at node A and would reduce the number of spurious events caused by non-perfect hyperfine pumping. Second, also the fidelity of the atom-photon entangled state and consequently the fidelity of the qubit preparation at node B would increase.

4.4. Generation of remote atom-atom entanglement

The previously demonstrated transfer of a quantum state by transmission of a single photon can be employed to generate entanglement between two distant atoms. This requires the combination of two steps. First, entanglement between an atom and a photon is generated

locally at node B. Second, the photon is sent to the atom at node A where it is coherently absorbed, thereby converting the atom-photon entanglement into entanglement between the two atoms. The fidelity of the generated state with respect to the ideal $|\Psi^-\rangle$ Bell state is determined by reconstructing the density matrix of the entangled state. We find a value of $\mathcal{F} = (85.0 \pm 1.3)\,\%$, which clearly exceeds the classical limit of $50\,\%$. The success probability of entanglement creation is given by the product of the photon generation efficiency at node B, the probability with which the photon is delivered to node A and its storage efficiency at node A. We find a value of $2\,\%$ for the combined process, yielding a rate of ~ 30 entanglement creations per second. Compared to experiments with single particles in free space [103], the efficiency is increased by six orders of magnitude, while the rate is increased by four orders of magnitude.

Another important figure of merit for the characterization of entangled states is its coherence time. After entanglement generation, we observe non-classical correlations for up to $100\,\mu\mathrm{s}$. The entanglement distribution time is $\sim 1\,\mu\mathrm{s}$, and is given by the time needed to generate a single photon at node B, transmit it to and store it at node A. The coherence time exceeds this time by two orders of magnitude and translates into a maximum possible entangled node distance of a $20\,\mathrm{km}$ optical fiber path.

A detailed analysis of this experiment will be subject of another PhD thesis by one of my colleagues.

5. Quantum teleportation

The content of this chapter has partially been published in:
Efficient teleportation between remote single-atom quantum memories.
C. Nölleke, A. Neuzner, A. Reiserer, C. Hahn, G. Rempe and S. Ritter, *Physical Review Letters* **110**, 140403 (2013).

The experiments described in the previous chapter demonstrate the faithful transfer of qubits between nodes in a quantum network using the direct transmission of a photon. The elegance of this protocol stems from its simplicity, as it only requires the transfer of a single photon carrying the information. However, the efficiency of the protocol drops exponentially with the distance between the nodes. In addition, it is in general more difficult to maintain a high fidelity with increasing distance, because even the small interaction of the photon with the environment causes irreversible decoherence and dephasing. A possible solution to this problem is based on the use of quantum repeaters [31, 46] to establish entanglement between widely separated nodes. This entanglement can then be used as a resource for the transfer of quantum information via teleportation [43, 104, 105] (see Fig. 5.1). This results in the communication time for the quantum information to scale only polynomially with distance [29]. Moreover, the quantum state to be transferred does not have to travel the whole distance via an error-prone channel, but is teleported "through" a quantum channel that is generated in a heralded way. Any loss that occurs while establishing the entanglement does not affect the fidelity of the state transfer.

A simple numerical example illustrates the need for such a device. Assume we want to transfer a qubit from Munich to Hamburg (distance $\sim 600\,\mathrm{km}$). The transmission probability T for photons through an optical fiber with length L is

$$T = 10^{-\frac{\alpha L}{10}}, \tag{5.1}$$

where α is the absorption coefficient. Suppose that photons at the telecom wavelength of $1550\,\mathrm{nm}$, at which absorption is minimized ($\alpha = 0.2\,\mathrm{dB/km}$), are used. Even with a perfect single-photon source in Munich operating at a rate of $10\,\mathrm{GHz}$ the rate of arriving photons in Hamburg would be less than one per minute.

In the repeater scheme, first adjacent quantum memories are entangled pairwise in parallel using a repeat-until-success scheme. Then, entanglement swapping [47] between these links is performed to generate entanglement between remote stations (Fig. 5.1b). The time it takes to establish entanglement scales polynomially with distance [29]. At large distances, a quantum repeater will therefore outperform any direct entanglement generation attempt, which scales exponentially. As the quantum information is naturally distributed using photonic carriers, the ability to generate atom-photon entanglement is an indispensable prerequisite. The additional elements required for a quantum repeater will add extra
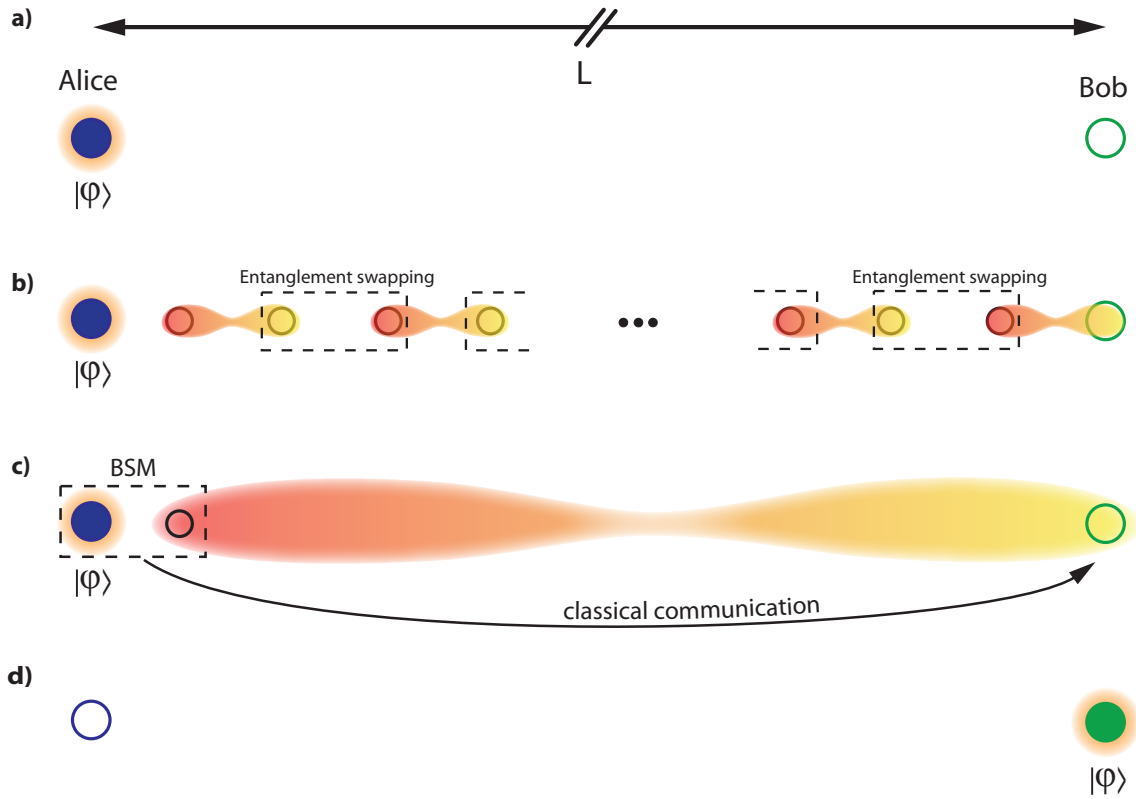
Figure 5.1.: Quantum state transfer using teleportation in a quantum repeater architecture. a) Alice wants to transfer a quantum state $|\varphi\rangle$, stored in a quantum memory, over a long distance L to Bob. **b)** Long-distance entanglement between Alice and Bob is generated by first entangling memories at intermediate locations and successive entanglement swapping operations. **c), d)** This entanglement link is then used as a resource for teleportation: A Bell-state measurement (BSM) between Alice's quantum state and one part of the entangled pair, together with classical communication of the BSM result, allows Bob to recover the state $|\varphi\rangle$ at his site.

sources of errors, resulting in a decrease of fidelity. Thus, in a practical repeater scheme, entanglement purification is necessary to obtain highly entangled states from a large number of less entangled ones [104, 106, 107].

In this chapter, we demonstrate quantum teleportation between remote single-atom quantum memories. The atoms are coupled to high-finesse optical cavities, enabling us to efficiently generate atom-photon entanglement and to efficiently map atomic onto photonic qubits. The required Bell-state measurement is implemented using linear optics and photon detection only.

The chapter is organized as follows. First, the general principle of quantum teleportation is reviewed. The specific implementation of the protocol in our experiment requires the detection of the Bell state of two photons. This is achieved using two-photon interference. Therefore, the physics of this effect is discussed, with a focus on time-resolved two-photon interference, which allows us to implement a herald for teleportation events with increased fidelity. After explaining the protocol that we use to teleport qubits between two atoms

trapped in optical cavities, the experimental implementation is described in detail. The teleportation channel is analyzed by performing a complete quantum process tomography, whose results are discussed.

5.1. Principle of quantum teleportation

The teleportation protocol aims at the transfer of quantum information between two separate parties. The sender at node A (called Alice) holds a potentially unknown qubit state $|\varphi\rangle_A$. She aims to send this state to the remote receiver at node B (called Bob). For any classical information the approach would be to copy and transmit it via a classical communication channel, allowing for a new transmission attempt should the previous one fail. Similarly, a classical repeater copies and amplifies the signal at intermediate locations. Quantum mechanics forbids to create a perfect copy of a quantum state due to the no-cloning theorem [21]. Nevertheless, one could still try to measure the quantum state and send this result to the receiver. For this scenario, the maximum achievable average state fidelity is 2/3 [101]. This is due to the fact that with a single measurement it is only possible to extract partial information of the actual quantum state. The classical limit for the process fidelity is 1/2.

In quantum teleportation, sender and receiver need to share an entangled pair. By performing a Bell-state measurement and classical communication of the measurement result, it is then possible to use this entanglement to transfer the initial quantum state from Alice to Bob. The qubit $|\varphi\rangle_A$ held by Alice is a superposition of two basis states $|\downarrow\rangle_A$ and $|\uparrow\rangle_A$:

$$|\varphi\rangle_A = \alpha |\downarrow\rangle_A + \beta |\uparrow\rangle_A \,, \tag{5.2}$$

with complex parameters α and β, and $|\alpha|^2 + |\beta|^2 = 1$. In the teleportation protocol originally proposed in [43], Bob holds a qubit that is maximally entangled with an ancilla qubit C. The latter is in possession of Alice (see Fig. 5.2). We assume this state to be the $|\Psi^-\rangle$ Bell state[1]:

$$\left|\Psi^-\right\rangle_{BC} = \frac{1}{\sqrt{2}} \left(|\downarrow\rangle_B |\uparrow\rangle_C - |\uparrow\rangle_B |\downarrow\rangle_C \right). \tag{5.3}$$

The three-particle state of the qubits A, B and C is

$$|\varphi\rangle_A \otimes \left|\Psi^-\right\rangle_{BC} = \left(\alpha |\downarrow\rangle_A + \beta |\uparrow\rangle_A\right) \otimes \frac{1}{\sqrt{2}} \left(|\downarrow\rangle_B |\uparrow\rangle_C - |\uparrow\rangle_B |\downarrow\rangle_C \right). \tag{5.4}$$

This can be rewritten in terms of the four maximally entangled Bell states $|\Phi^\pm\rangle_{AC} = \frac{1}{\sqrt{2}} \left(|\downarrow\rangle_A |\downarrow\rangle_C \pm |\uparrow\rangle_A |\uparrow\rangle_C \right)$ and $|\Psi^\pm\rangle_{AC} = \frac{1}{\sqrt{2}} \left(|\downarrow\rangle_A |\uparrow\rangle_C \pm |\uparrow\rangle_A |\downarrow\rangle_C \right)$ of A and C:

$$\begin{aligned}
|\varphi\rangle_A \left|\Psi^-\right\rangle_{BC} = &\frac{1}{2} \left(\left|\Phi^+\right\rangle_{AC} \sigma_x \sigma_z |\varphi\rangle_B \right) + \frac{1}{2} \left(\left|\Phi^-\right\rangle_{AC} \sigma_x |\varphi\rangle_B \right) \\
&- \frac{1}{2} \left(\left|\Psi^+\right\rangle_{AC} \sigma_z |\varphi\rangle_B \right) - \frac{1}{2} \left(\left|\Psi^-\right\rangle_{AC} |\varphi\rangle_B \right).
\end{aligned} \tag{5.5}$$

---

[1]Quantum teleportation is not restricted to this specific state. Indeed, any maximally entangled state would work. More general, any bipartite entangled state that violates the CHSH inequality is useful for teleportation [108], the reverse statement, however, is in general not true [109].

Figure 5.2.: Principle of quantum teleportation. Alice (A) holds a quantum state $|\varphi\rangle_A$ that she aims to teleport to Bob (B). He sends an ancilla qubit C that is entangled with his qubit over to Alice. She then performs a Bell-state measurement (BSM) between her qubit and the ancilla. The result of this measurement is communicated to Bob via a classical channel. Depending on the outcome of the BSM, Bob performs a unitary operation U on his qubit to recover the state $|\varphi\rangle$. If the result of the BSM is the $|\Psi^-\rangle$ Bell state, the initial state is directly recovered, i.e. $U = \mathbb{1}$.
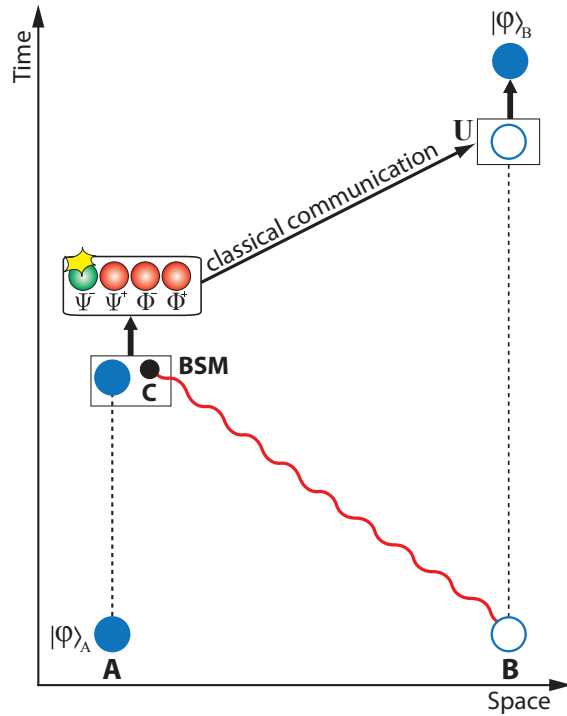
A joint Bell-state measurement of the qubits A and C, i.e. a projective measurement onto the states $|\Phi^\pm\rangle_{AC}$ and $|\Psi^\pm\rangle_{AC}$, projects Bob's qubit onto the initial state $|\varphi\rangle$ of Alice's qubit up to a unitary transformation, expressed in terms of the Pauli operators σ_x and σ_z, and an irrelevant global phase. σ_x corresponds to a spin flip, whereas σ_z induces a phase change of π in the qubit $|\varphi\rangle$. The exact transformation depends on the detected Bell state. As the outcome of the projective Bell-state measurement is random, Alice needs to communicate the result of her measurement (2 bits of classical information encoding one out of the four possible results) to Bob. He then uses this information to perform the inverse unitary transformation, thereby retrieving the initial state from Alice. If the result of the Bell-state measurement is the $|\Psi^-\rangle_{AC}$ state, the necessary operation is the identity operation, i.e. Bob needs to do nothing since the initial state is directly recovered.

After teleportation, Alice's node is disentangled from the system. It is therefore not possible for Alice to retrieve any information about her state after teleportation has been completed. It is important to mention that neither the quantum channel (the shared entangled pair) nor the classical communication channel alone carries any information about the quantum state to be teleported. It is the combination of both that is necessary for a successful state transfer.

Since its proposal in 1993, quantum teleportation was successfully implemented in various physical systems. The first realization was achieved with photonic qubits in 1997 [110–112]. Because of their prospects in quantum computation [113] and communication [10], purely photonic systems are still an active field of research. One important application is the distribution of secret keys in quantum cryptography. Teleportation can help to extend the

distance over which keys can be distributed in a quantum-relay configuration[2] [114, 115], however still with a limited maximal range [116]. Recently, the current record in distance of 143 km has been demonstrated by teleporting photonic quantum states between two Canary Islands [117]. The current approach to bridge even larger distances is to use free-space transmission [118, 119] with the ultimate goal to use outer space as the communication channel [120]. Without atmosphere, the photonic states would be subjected to less harmful effects that cause loss and decoherence, compared to fiber-based or earth-bound line-of-sight transmission. Regarding the physical implementation of the photonic qubit, robustness against inevitable loss during propagation is essential. A widely used degree of freedom is polarization[3], however, teleportation between photons using time-bin qubits has also been demonstrated [122]. Qubits encoded in either of these two discrete degrees of freedom are robust, in the sense that photon loss does not compromise the fidelity but only reduces the efficiency of the protocol. Other studied degrees of freedom for the encoding of quantum information are continuous variables [123]. While they allow for the realization of deterministic protocols [112, 124, 125], transmission losses induce inevitable decoherence and limit the achievable fidelity [126, 127].

Purely photonic systems cannot be utilized for the implementation of a quantum repeater because quantum memories require a material quantum system to be involved. Teleportation between material qubits was first achieved with trapped ions using a deterministic protocol [128, 129], albeit over a distance limited to a few micrometers owing to the short-range Coulomb interaction. More recently, deterministic teleportation between artificial qubits on the same chip has been realized [130]. As was mentioned above, the transfer of quantum information over large distances requires the combination of stationary quantum memories and entanglement between light and matter (see Tab. 5.1). Along these lines, quantum teleportation from light onto an ensemble of atoms has been demonstrated [124, 131]. The first experiment demonstrating teleportation between remote material systems was between two single ions separated by about one meter [132]. The low efficiency due to the limited light-matter interaction in free space, however, prevents scaling of that approach to larger networks.

So far, experiments on long-distance teleportation suffered from low success probabilities. The collection efficiency of single photons generated by single emitters in free space constitutes a significant bottleneck towards the achievement of macroscopic success probabilities. There are two approaches to overcome this fundamental problem. The first is to take advantage of collective excitations that lead to an enhanced coupling to light and directed emission of photons [135–137]. This was used in a recent experiment, which demonstrated teleportation between two cold atomic ensembles at a distance of approximately 1 m [134]. The second approach, which is the one we pursue, is to embed single atoms in optical cavities. This dramatically increases the light-matter coupling and enables a coherent

---

[2]A *quantum relay* works in the same way as a quantum repeater only without memories and entanglement purification. It can therefore not help to beat the exponential scaling of transmission losses, but can increase the signal-to-noise ratio in QKD protocols.

[3]An interesting observation in this context is, that radiation from the Big Bang is still partially polarized [121], indicating the potential of polarization qubits in terms of decoherence.

Sender	Receiver	Reference	Distance	Efficiency	Rate	Fidelity
Atom	Atom	[133]	$\sim \text{nm}$	1 ①	n/a	~ 0.9
		[128, 129]	$\sim \upmu\text{m}$	1 ①	$\sim 300\,\text{s}^{-1}$	~ 0.8
		[132]	$1\,\text{m}$	$2.2 \cdot 10^{-8}$	$1/12\,\text{min}^{-1}$	0.9
		[48] ②	$21\,\text{m}$	$0.1\,\%$	$10\,\text{s}^{-1}$	~ 0.8
Photon	Ensemble	[131]	$7\,\text{m}$	10^{-6}	n/a	n/a ③
Ensemble	Ensemble	[134]	$1\,\text{m}$	$0.5 \cdot 10^{-4}$	n/a	0.95
SSQC	SSQC	[130]	$6\,\text{mm}$	0.7 ①	$40 \cdot 10^3\,\text{s}^{-1}$	0.73

Table 5.1.: Experimental demonstrations of teleportation of discrete qubits involving quantum memories. Remarks: ① deterministic scheme, ② this work, ③ No full process tomography is performed. Quantum nature of the teleportation channel is not unambiguously proven. SSQC: Solid state quantum circuit.

exchange between the internal state of an atom and the polarization of a photon. Moreover, it leads to preferred emission of photons into one well-defined spatial mode.

In the teleportation experiment described in this chapter, we aim to transfer a qubit from an atom at node A (the sender) to an atom at node B (the receiver), which is located in another laboratory at a distance of 21 m. We generate a single photon at node B in a way that the photonic polarization is entangled with the internal Zeeman state of the atom. The qubit state of node A is coherently mapped onto the polarization of another photon. The Bell-state measurement is then performed between the two photons.

5.2. Optical Bell-state analyzer for polarization qubits

The central ingredient in the teleportation protocol is the Bell-state measurement between the qubit of the sender and one part of the entangled pair [cf. Eq. (5.5)]. In our implementation, we perform this measurement between photonic-polarization qubits by employing two-photon interference and polarization-sensitive photodetection [138, 139].

In section 5.2.1, the theoretical background of the effect of two-photon interference is reviewed. A simplified model that allows us to understand the basic principle of this effect is presented. Following the description of the implementation of the Bell-state analyzer with linear optics and single-photon detectors in section 5.2.2, the model for two-photon interference is extended in section 5.2.3 to deal with imperfections in the experiment and to take temporal aspects into account.

5.2.1. Fundamentals of two-photon interference

We use the Fock-state picture to describe the effect of two-photon quantum interference. In this picture, the spatio-temporal mode i of the electromagnetic field is expressed in terms of states $|n\rangle$, with n being the number of photons in the mode. The photon-creation and
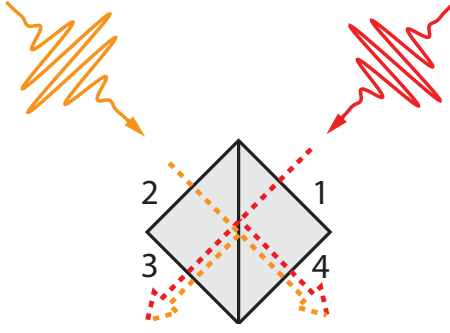
Figure 5.3.: Two-photon interference on a non-polarizing beam splitter. Single photons enter the beam splitter in the modes 1 and 2. The NPBS mixes the input modes and gives rise to interference.

-annihilation operators $a_i^\dagger$ (a_i) create (annihilate) a single photon in the mode i. These operators obey the bosonic commutation relations

$$[a_i, a_j] = 0, \quad [a_i^\dagger, a_j^\dagger] = 0,$$
$$[a_i, a_i^\dagger] = 1, \quad [a_i, a_j^\dagger] = 0,$$

for orthogonal modes[4] i and j. We write the photonic quantum state as $|\Psi\rangle = |n_i, m_j\rangle$, with $n_i (m_j)$ being the number of quanta in the mode $i(j)$.

We consider the situation shown in Fig. 5.3. Two single photons in the same temporal mode impinge on a non-polarizing beam splitter (NPBS), one in each of the spatial modes 1 and 2. As known from classical optics, the beam splitter mixes these input modes to output modes 3 and 4 [140]. In quantum mechanics this corresponds to a unitary evolution of the field operators described by the unitary operator U:

$$\begin{pmatrix} a_3 \\ a_4 \end{pmatrix} = U \begin{pmatrix} a_1 \\ a_2 \end{pmatrix} U^\dagger = \mathcal{B} \begin{pmatrix} a_1 \\ a_2 \end{pmatrix}. \tag{5.6}$$

For an ideal and symmetric beam splitter the unitary matrix $\mathcal{B}$ reads [141]:

$$\mathcal{B} = \frac{1}{\sqrt{2}} \begin{pmatrix} 1 & 1 \\ -1 & 1 \end{pmatrix}. \tag{5.7}$$

The negative sign in the element $\mathcal{B}_{21}$ corresponds to a phase shift of π that a classical light wave experiences upon reflection off a beam splitter relative to a wave that is transmitted[5].

The input state $|\Psi_{\mathrm{in}}\rangle$ can be written in terms of creation operators that act on the vacuum state $|0\rangle \equiv |0_1, 0_2\rangle$:

$$|\Psi_{\mathrm{in}}\rangle = |1_1, 1_2\rangle = a_1^\dagger a_2^\dagger |0\rangle. \tag{5.8}$$

In the Schrödinger picture, the action of the NPBS is a unitary operation U that evolves the initial state into an output state according to[6]

$$|\Psi_{\mathrm{out}}\rangle = U |\Psi_{\mathrm{in}}\rangle = U \left(a_1^\dagger a_2^\dagger \right) |0\rangle = \left(U a_1^\dagger U^\dagger \right) \left(U a_2^\dagger U^\dagger \right) |0\rangle. \tag{5.9}$$

---

[4]Modes in different ports of the NPBS are orthogonal.

[5]The entries in the off-diagonal elements of the matrix $\mathcal{B}$ are a matter of definition. In general, the phase difference between reflected and transmitted part must be equal to π [142].

[6]In the Schrödinger picture the modes themselves do not change. This means that modes 1 and 2 describe both, the input and output modes.
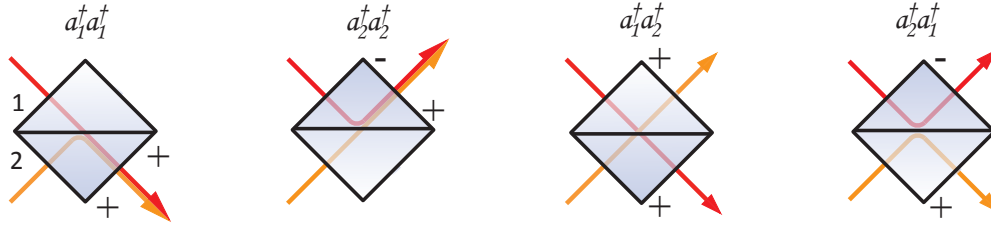
Figure 5.4.: Illustration of two-photon interference on a beam splitter. If two photons impinge on the beam splitter, one in each input mode, there are four possible paths for the photons to pass through the beam splitter. In the first two cases, the photons leave from the same output port. In the last two cases, the photons leave from different ports. The last two cases are indistinguishable and their amplitudes have opposite signs, so that they interfere destructively.

The last conversion uses $U^\dagger U = \mathbb{1}$ and $U\left|0\right\rangle = U^\dagger\left|0\right\rangle = \left|0\right\rangle$. Using Eq. (5.6), this becomes

$$\left|\Psi_{\mathrm{out}}\right\rangle = \frac{1}{\sqrt{2}}\left[\left(a_1^\dagger\right)^2 - \left(a_2^\dagger\right)^2 + a_1^\dagger a_2^\dagger - a_2^\dagger a_1^\dagger\right]\left|0\right\rangle. \tag{5.10}$$

The meaning of this equation is illustrated in Fig. 5.4. Each term corresponds to one possible path of the two photons passing through the beam splitter. The states created by $a_1^\dagger a_2^\dagger$ and $a_2^\dagger a_1^\dagger$ are identical and interfere destructively due to their relative phase of π. This quantum interference effect is known as the *Hong-Ou-Mandel effect* [143]: identical photons impinging on a non-polarizing beam splitter coalesce, so that the output state becomes

$$\left|\Psi_{\mathrm{out}}\right\rangle = \frac{1}{\sqrt{2}}\left[\left|2_1,0_2\right\rangle - \left|0_1,2_2\right\rangle\right]. \tag{5.11}$$

The two photons leave the beam splitter paired from only one (random) output port. Therefore, the strategy to experimentally verify the Hong-Ou-Mandel effect is to measure correlations between photon detections in the two output ports of the beam splitter. The absence of coincident photodetections then proves the underlying effect of quantum interference.

This effect can also be seen as a consequence of the bosonic nature of the photons. The last two terms of Eq. (5.10) are equal to the bosonic commutator $[a_1^\dagger, a_2^\dagger]$ and therefore vanish. In case of fermions, the first two terms of Eq. (5.10) would be equal to zero, resulting in anti-coalescence of the particles.

5.2.2. Linear-optics Bell-state analyzer

After we analyzed the interference of two single photons at a beam splitter, we will now broaden the focus and analyze the interference properties of non-separable polarization states. This will conclude in the identification of an NPBS as a powerful Bell-state filter [138, 139].

The four Bell states $\{\left|\Psi^\pm\right\rangle, \left|\Phi^\pm\right\rangle\}$ form a basis of the four-dimensional Hilbert space of a two-qubit system, the so-called *Bell basis* [144]. The $\left|\Psi^-\right\rangle$ state is antisymmetric, whereas the other three are symmetric under particle exchange. The total wavefunction describing

two photons must obey bosonic quantum statistics, i.e. it has to be symmetric under exchange of the two photons. Considering the spatial and polarization degree of freedom, there are two possibilities to achieve this symmetry: Either both parts are symmetric or both parts are antisymmetric. This results in four possible input states at the NPBS:

$$\left|\Psi^-\right\rangle_{\mathrm{total}} = \left|\Psi^-\right\rangle_{\mathrm{pol}} \otimes \frac{1}{\sqrt{2}}\left(\left|1_1,1_2\right\rangle - \left|1_2,1_1\right\rangle\right) = \left|\Psi^-\right\rangle_{\mathrm{pol}} \otimes \left|\Psi^{\mathrm{as}}\right\rangle_{\mathrm{sp}}$$

$$\left|\Psi^+\right\rangle_{\mathrm{total}} = \left|\Psi^+\right\rangle_{\mathrm{pol}} \otimes \frac{1}{\sqrt{2}}\left(\left|1_1,1_2\right\rangle + \left|1_2,1_1\right\rangle\right) = \left|\Psi^+\right\rangle_{\mathrm{pol}} \otimes \left|\Psi^{\mathrm{s}}\right\rangle_{\mathrm{sp}}$$

$$\left|\Phi^-\right\rangle_{\mathrm{total}} = \left|\Phi^-\right\rangle_{\mathrm{pol}} \otimes \frac{1}{\sqrt{2}}\left(\left|1_1,1_2\right\rangle + \left|1_2,1_1\right\rangle\right) = \left|\Phi^-\right\rangle_{\mathrm{pol}} \otimes \left|\Psi^{\mathrm{s}}\right\rangle_{\mathrm{sp}}$$

$$\left|\Phi^+\right\rangle_{\mathrm{total}} = \left|\Phi^+\right\rangle_{\mathrm{pol}} \otimes \frac{1}{\sqrt{2}}\left(\left|1_1,1_2\right\rangle + \left|1_2,1_1\right\rangle\right) = \left|\Phi^+\right\rangle_{\mathrm{pol}} \otimes \left|\Psi^{\mathrm{s}}\right\rangle_{\mathrm{sp}}.$$

The subscripts *pol* and *sp* denote the polarization and spatial part of the wave function. All of these four states are symmetric. The state $\left|\Psi^-\right\rangle_{\mathrm{total}}$ is the only one that has an antisymmetric spatial part $\left|\Psi^{\mathrm{as}}\right\rangle_{\mathrm{sp}}$ while the other three are accompanied by a symmetric spatial part $\left|\Psi^{\mathrm{s}}\right\rangle_{\mathrm{sp}}$. Using the unitary beam splitter transformation from Eq. (5.7), it immediately follows that a symmetric spatial part leads to Hong-Ou-Mandel interference (coalescence) while an antisymmetric spatial part leads to photons always leaving the beam splitter from different output ports (anti-coalescence):

$$U\left|\Psi^{\mathrm{s}}\right\rangle_{\mathrm{sp}} = \frac{1}{\sqrt{2}}\left(\left|1_1,1_1\right\rangle - \left|1_2,1_2\right\rangle\right) \quad \text{(coalescence)}$$

$$U\left|\Psi^{\mathrm{as}}\right\rangle_{\mathrm{sp}} = \frac{1}{\sqrt{2}}\left(\left|1_1,1_2\right\rangle - \left|1_2,1_1\right\rangle\right) \quad \text{(anti-coalescence).}$$

Consequently, if a pair of photons leaves the beam splitter from different ports, their spatial wavefunction must have been antisymmetric. In this case, owing to the bosonic nature of photons, their polarization state must have been antisymmetric as well. For photons leaving the beam splitter from the same output port, their polarization state is either $\left|\Psi^+\right\rangle_{\mathrm{pol}}, \left|\Phi^-\right\rangle_{\mathrm{pol}}$ or $\left|\Phi^+\right\rangle_{\mathrm{pol}}$. Of these states, the $\left|\Psi^+\right\rangle_{\mathrm{pol}}$ state has the unique feature that it leads to correlations between orthogonal polarization states of the two photons. Polarization-sensitive detection of the photons, for example by placing a polarizing beam splitter and two single-photon detectors in each output port of the NPBS, thus allows us to additionally identify the $\left|\Psi^+\right\rangle_{\mathrm{pol}}$ state. A sketch of such a Bell-state analyzer is shown in Fig. 5.5. Correlations between orthogonal polarizations in different output ports of the NPBS correspond to the $\left|\Psi^-\right\rangle_{\mathrm{pol}}$ state. Correlations between orthogonal polarizations in the same output port of the NPBS correspond to the $\left|\Psi^+\right\rangle_{\mathrm{pol}}$ state. Photons in the states $\left|\Phi^-\right\rangle_{\mathrm{pol}}$ and $\left|\Phi^+\right\rangle_{\mathrm{pol}}$ leave the NPBS from the same output port. As these photons possess identical polarizations, there is no way to unambiguously identify these states using only linear optics.

The ability of the NPBS to filter $\left|\Psi^-\right\rangle_{\mathrm{pol}}$ states can also be understood intuitively. Assuming perfect Hong-Ou-Mandel interference, photons leaving from different ports must have been orthogonally polarized (otherwise the interference results in photons leaving the beam splitter in pairs). The beam splitter erases the which-way information of the photons such that behind the beam splitter it is impossible to tell which photon has passed through the

Figure 5.5.: Scheme of an all-optical Bell-state analyzer for polarization qubits. Two photons are superimposed on an NPBS. A PBS and two single-photon detectors in each output port of the NPBS allow us to discriminate between horizontally (H) and vertically (V) polarized photons. Correlations between different detectors (indicated by the wires) either herald a $|\Psi^-\rangle_{\text{pol}}$ or a $|\Psi^+\rangle_{\text{pol}}$ state. Correlations between detectors corresponding to parallel polarized photons in different output ports of the NPBS only occur if the two-photon interference is not perfect.
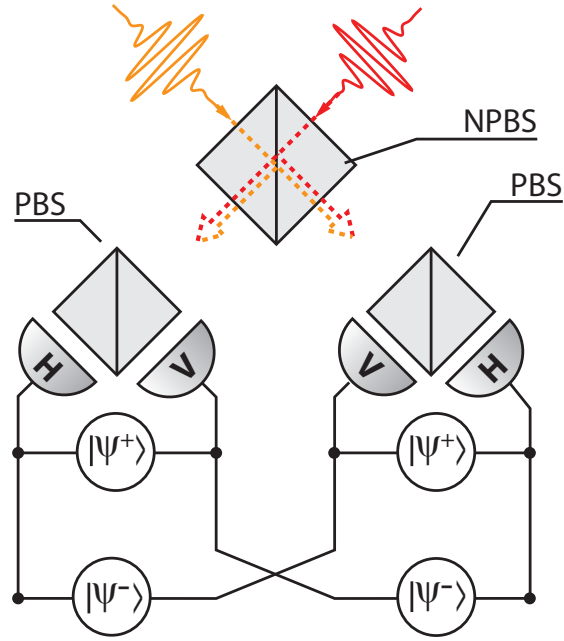
beam splitter along which path. As a consequence, the state behind the beam splitter is a superposition of these two pathways with a relative phase of π, given by the matrix from Eq. (5.7).

The representation of the Bell states depends on the chosen polarization basis. In our case, we use the H/V-basis, corresponding to the atomic basis $\{|\downarrow_{\text{x}}\rangle, |\uparrow_{\text{x}}\rangle\}$ (see Appendix B). This differs from the computational basis $\{|\downarrow\rangle, |\uparrow\rangle\}$ corresponding to the polarization basis R/L, which was used in the derivation of Eq. (5.5). Rewriting Eq. (5.5) with the Bell states defined in the basis $\{|\downarrow_{\text{x}}\rangle, |\uparrow_{\text{x}}\rangle\}$ $[|\Phi^\pm\rangle_{\text{AC}} = \frac{1}{\sqrt{2}}(|\downarrow_{\text{x}}\rangle_{\text{A}} |\downarrow_{\text{x}}\rangle_{\text{C}} \pm |\uparrow_{\text{x}}\rangle_{\text{A}} |\uparrow_{\text{x}}\rangle_{\text{C}})$ and $|\Psi^\pm\rangle_{\text{AC}} = \frac{1}{\sqrt{2}}(|\downarrow_{\text{x}}\rangle_{\text{A}} |\uparrow_{\text{x}}\rangle_{\text{C}} \pm |\uparrow_{\text{x}}\rangle_{\text{A}} |\downarrow_{\text{x}}\rangle_{\text{C}})]$ results in:

$$
\begin{aligned}
|\varphi\rangle_{\text{A}} |\Psi^-\rangle_{\text{BC}} = \frac{1}{2} \left(|\Phi^+\rangle_{\text{AC}} \, \sigma_{\text{x}}\sigma_{\text{z}} |\varphi\rangle_{\text{B}} \right) - \frac{1}{2} \left(|\Phi^-\rangle_{\text{AC}} \, \sigma_{\text{z}} |\varphi\rangle_{\text{B}} \right) \\
+ \frac{1}{2} \left(|\Psi^+\rangle_{\text{AC}} \, \sigma_{\text{x}} |\varphi\rangle_{\text{B}} \right) - \frac{1}{2} \left(|\Psi^-\rangle_{\text{AC}} \, |\varphi\rangle_{\text{B}} \right).
\end{aligned}
\tag{5.12}
$$

Therefore, detection of a $|\Psi^+\rangle$ event in the described Bell-state analyzer during the teleportation protocol projects the state of atom B to the state $\sigma_{\text{x}} |\varphi\rangle_{\text{B}}$. Because the $|\Psi^-\rangle$ is invariant under change of the qubit basis, detection of this state always directly heralds the successful state transfer, independent of the measurement basis.

In the teleportation protocol (see section 5.3.1), the photon at one input of the NPBS is randomly polarized as it is part of an entangled Bell state. Therefore, each of the four outcomes of the Bell-state measurement is equally probable. As only two out of the four photonic Bell states can be identified unambiguously, the maximum achievable efficiency for teleportation using a linear-optics Bell-state measurement is limited to 50 % [145]. Because only detection of the $|\Psi^-\rangle$ Bell state directly projects the receiver state to the input state, teleportation without a local operation at the receiver site is limited to an efficiency of 1/4.

5.2.3. Time-resolved two-photon interference

The simple model of two-photon interference presented in section 5.2.1 assumes that the photons are identical in all their properties, i.e. in polarization, frequency and temporal mode. This assumption, however, is not fulfilled in our experiment. To explain our results, the model is extended according to previous studies [141, 146]. Special emphasis is put on the ability to evaluate the effect of two-photon interference in a time-resolved manner. The photonic wave packets generated in our system typically exceed the temporal resolution of the detection system. Therefore, the interference properties of single photons can be studied "within their wave packet". This serves as a diagnostic tool for coherence properties in quantum interference experiments.

The operator $a^\dagger$ defined above creates a single photon with a delta-like frequency spectrum and is thus not defined in time. While the use of these operators allows for an understanding of the physics of interference between two identical photons, a quantitative description of non-identical photons requires a realistic model of the photonic modes. Such modes can in general be described by a complex function ξ with real amplitude ε and phase ϕ:

$$\xi_k(q) = \varepsilon_k(q)\, \mathrm{e}^{-i\phi_k(q)}\,. \tag{5.13}$$

This *spatio-temporal mode function* depends on the spatio-temporal coordinate $q = t - z/c$. We are interested in the mode function at the position of the NPBS, which we set to $z = 0$, so that $q = t$. The index k is used to label the modes. The corresponding operator that creates a single photon in the mode ξ_k is denoted by $c_k^\dagger$:

$$\left|1_{\xi_k}\right\rangle = c_k^\dagger\left|0\right\rangle. \tag{5.14}$$

We now investigate correlations between the output modes of the beam splitter. For this purpose we use a *second-order correlation function* that is defined as [147]

$$G^{(2)}(t_1,t_2) = \mathrm{Tr}\left[\rho_\mathrm{in} A_{3,4}(t_1,t_2)\right], \tag{5.15}$$

with the input state ρ_in and the operator

$$A_{3,4} = a_3^\dagger a_4^\dagger a_4 a_3. \tag{5.16}$$

$G^{(2)}(t_1,t_2)$ is the quantum mechanical version of the classical intensity correlation function $\langle I_1(t_1)I_2(t_2)\rangle_t$.

The detection and analysis of two-photon interference requires the measurement of correlations between two detection events in different output ports of the beam splitter. The probability to detect such a correlation is given by the *joint-detection probability* $P^{(2)}$. This quantity is the probability to detect a first photon at time t_0 in one output port of the NPBS and a second photon at a time $t_0 + \tau$ in the other port. For our purposes, only the time difference τ is relevant. In the case of photons with a temporal length that is large compared to the temporal resolution t_res of the detectors, $P^{(2)}(\tau)$ is related to the second-order correlation function by

$$P^{(2)}(\tau) = \eta_D t_\mathrm{res}\int \mathrm{d}t_0\, G^{(2)}(t_0,t_0+\tau). \tag{5.17}$$

η_D is the product of the quantum efficiencies of the two detectors.

To gain some insight about the joint-detection probability $P^{(2)}(\tau)$ we discuss two important examples.

Identically polarized photons. We consider two photons in the mode ξ_k with parallel polarizations, one at each input k of the NPBS. The input state then reads $\rho_{\text{in}} = \left|1_{\xi_1},1_{\xi_2}\right\rangle\left\langle1_{\xi_1},1_{\xi_2}\right|$. By using Eq. (5.14) and Eq. (5.15) it can be shown that [141]

$$G_{\parallel}^{(2)}(t_1,t_2) = \frac{1}{4}\left|\xi_1(t_1)\xi_2(t_2) - \xi_2(t_1)\xi_1(t_2)\right|^2. \tag{5.18}$$

If the mode functions are identical, i.e. $\xi_1(t) = \xi_2(t)$ for all times t, $G_{\parallel}^{(2)}$ and consequently $P_{\parallel}^{(2)}(\tau)$ is zero for all values of τ. This is the result of perfect Hong-Ou-Mandel interference, according to Eq. (5.11). Different mode functions lead to values greater than zero for $G_{\parallel}^{(2)}$. For $\tau = t_2 - t_1 = 0$, however, the correlation function is always zero even if the mode functions differ.

Perpendicularly polarized photons. We now assume the photons to have orthogonal polarizations. The state of the photons is then not only described by the mode function, but also by the state of polarization, for example $\updownarrow$ and $\leftrightarrow$. With the input state $\rho_{\text{in}} = \left|1_{\xi_1}^{\leftrightarrow},1_{\xi_2}^{\updownarrow}\right\rangle\left\langle1_{\xi_1}^{\leftrightarrow},1_{\xi_2}^{\updownarrow}\right|$, the correlation function is calculated to be [141]

$$G_{\perp}^{(2)}(t_1,t_2) = \frac{1}{4}\left(\left|\xi_1(t_1)\xi_2(t_2)\right|^2 + \left|\xi_1(t_2)\xi_2(t_1)\right|^2\right). \tag{5.19}$$

$G_{\perp}^{(2)}$ is always larger than zero, unless either $\xi_1(t)$ or $\xi_2(t)$ is equal to zero at all times.

As becomes clear from these examples, perfect Hong-Ou-Mandel interference is only observed for parallel polarized photons with identical mode functions (i.e. perfectly indistinguishable photons). Any mismatch in the mode functions leads to a reduction of this coalescence effect. In the case of orthogonal polarizations, the photons are fully distinguishable and do not show interference. To derive a figure of merit for the degree of two-photon interference, we compare the number of interfering photons with the number of non-interfering photons. A convenient way to achieve this, is to measure the correlation function for photons with orthogonal polarization as a reference. Comparing the correlation function for parallel polarized photons to the reference directly yields a figure of merit for the indistinguishability of the photons. We define the *contrast* $C(\tau)$ as

$$C(\tau) = 1 - \frac{P_{\parallel}^{(2)}(\tau)}{P_{\perp}^{(2)}(\tau)} = \frac{P_{\perp}^{(2)}(\tau) - P_{\parallel}^{(2)}(\tau)}{P_{\perp}^{(2)}(\tau)}. \tag{5.20}$$

Integrated over the whole photonic wavepacket the *integrated contrast* becomes

$$C = 1 - \frac{\int P_{\parallel}^{(2)}(\tau)\mathrm{d}\tau}{\int P_{\perp}^{(2)}(\tau)\mathrm{d}\tau}. \tag{5.21}$$

$P_\parallel^{(2)}$ is only smaller than $P_\perp^{(2)}$ if the photons interfere destructively. Consequently, a contrast $C > 0$ unambiguously proves quantum interference and that the photons are, at least partially, indistinguishable.

To measure the correlation functions we have to prepare an ensemble of photonic input states $\rho_{\text{in}} = \left|1_{\xi_1}, 1_{\xi_2}\right\rangle \left\langle 1_{\xi_1}, 1_{\xi_2}\right|$ and average over correlations between detection events in different NPBS ports of the whole ensemble. This requires a perfect single-photon source as only then all photons in the ensemble can be described by the same state vector $\left|1_\xi\right\rangle$. In a realistic experiment, a stream of single photons shows a variation (or jitter) in the parameters of the mode function, so-called shot-to-shot variations. Let ϑ describe one or more parameters that are affected by jitter. The variation of ϑ in the ensemble can be described by a normalized distribution function $f(\vartheta)$. The density operator of such an ensemble is then written as [140]

$$\rho = \int \mathrm{d}\vartheta f(\vartheta) \left|1_\xi\right\rangle \left\langle 1_\xi\right|. \tag{5.22}$$

At the input of the beam splitter, there are two photon streams (one at each input port) such that the input state becomes

$$\rho_{\text{in}} = \iint \mathrm{d}\vartheta_1 \mathrm{d}\vartheta_2 f_1(\vartheta_1) f_2(\vartheta_2) \left|1_{\xi_1}, 1_{\xi_2}\right\rangle \left\langle 1_{\xi_1}, 1_{\xi_2}\right|. \tag{5.23}$$

For the following discussion we assume a Gaussian envelope for the photonic mode functions:

$$\xi_k(t) = \sqrt[4]{\frac{2}{\pi \delta t^2}} \exp\left[-\frac{(t - \tau_k)^2}{\delta t^2}\right] \exp\left[i\omega_k(t - \tau_k)\right]. \tag{5.24}$$

δt is the half $1/\mathrm{e}$-width of the Gaussian envelope[7] and is called the *photon length*. ω_k is the frequency of the photon and τ_k its *emission time*. This time is equivalent to the time where the mode function has its maximum at the position of the beam splitter. Furthermore we assume that both streams show Gaussian variations in the emission time, characterized by the same width $\Delta\tau$ of the distribution. The jitter can then be described by a variation of the *arrival-time delay* $\delta\tau = \tau_2 - \tau_1$ (equivalent to a delay of the emission times) between the two photons using the normalized Gaussian distribution

$$f(\delta\tau) = \frac{1}{\sqrt{\pi}\Delta\tau} \exp\left[-\frac{\delta\tau^2}{\Delta\tau^2}\right]. \tag{5.25}$$

By using Eq. (5.23), Eq. (5.17) and Eq. (5.15), the joint-detection probability for parallel and orthogonally polarized photons can be calculated[8]:

$$P_\parallel^{(2)}(\tau) = \frac{1}{2\sqrt{\pi}\sqrt{\delta t^2 + \Delta\tau^2}} \left(1 - \exp\left[-\frac{\tau^2}{\delta t^2 + \delta t^4/\Delta\tau^2}\right]\right) \cdot \exp\left[-\frac{\tau^2}{\delta t^2 + \Delta\tau^2}\right] \tag{5.26}$$

$$P_\perp^{(2)}(\tau) = \frac{1}{2\sqrt{\pi}\sqrt{\delta t^2 + \Delta\tau^2}} \exp\left[-\frac{\tau^2}{\delta t^2 + \Delta\tau^2}\right]. \tag{5.27}$$

---

[7] The full width at half-maximum (FWHM) is related to δt by $\mathrm{FWHM} = 2\sqrt{\ln(2)}\delta t$.

[8] The quantum efficiency η_D and the resolution t_{res} of the detectors are ignored as these quantities cancel out when the contrast is calculated.

Figure 5.6.: Joint-detection proba-bility as a function of the detection-time difference τ for photon streams that show a variation in their emission time. The figure shows the joint-detection probability for orthogonally polarized photons (red dashed line) according to Eq. (5.27) and for parallel polarized photons (blue dashed line) according to Eq. (5.26). The variation of the emission time is $\Delta\tau = 1.5\delta t$.
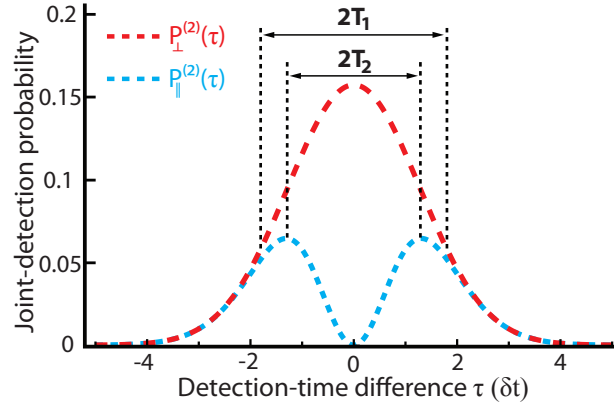
This result is plotted in Fig. 5.6. The width T_1 of the Gaussian-shaped peak for the case of orthogonally polarized photons is the result of convoluting the photonic wave packet with width δt, with the distribution function of the arrival-time variation with width $\Delta\tau$:

$$T_1 = \sqrt{\delta t^2 + \Delta\tau^2}. \tag{5.28}$$

The presence of arrival-time variations results in a characteristic double peak structure of the joint-detection probability of identically polarized photons. The width of the dip in the function $P_\parallel^{(2)}(\tau)$ is given by the temporal distance between the maxima of the two peaks:

$$T_2 = \sqrt{\delta t^2 + \frac{\delta t^4}{\Delta\tau^2}} = \frac{\delta t}{\Delta\tau}T_1. \tag{5.29}$$

By assuming that a variation in the emission time is the main mechanism reducing the interference contrast, it is therefore possible to determine the width of this jitter $\Delta\tau$ as well as the actual length of the individual photon wavepackets δt. The integrated contrast becomes

$$C = \frac{\delta t}{\sqrt{\delta t^2 + \Delta\tau^2}}. \tag{5.30}$$

The occurrence of emission-time jitter thus reduces the achievable contrast.

5.3. Teleportation between remote single atoms

After the theoretical foundations have been laid, we now turn to the implementation of our teleportation experiment. Following the description of the specific protocol, a simple formula relating the fidelity of the teleportation process to the fidelities of entanglement generation, state mapping and interference contrast is derived. Subsequently, the experimental implementation is explained in detail and it is described how the vSTIRAP is employed to generate indistinguishable photons from the independent systems. This is a crucial step for the optical Bell-state measurement and the quality of the two-photon interference is discussed. After a detailed description of the experimental steps involved in the teleportation protocol, the chapter concludes with the discussion of the results.

5.3.1. Teleportation protocol

The employed protocol to perform and to analyze quantum teleportation consists of five steps (see Fig. 5.7):

- Preparation of the qubit at node A.

- Generation of atom-photon entanglement at node B.

- State mapping of atom A onto a photon A$'$.

- Bell-state measurement between the two photons.

- State detection at node B.

Initially, atom A is prepared in a qubit state $|\varphi\rangle_A = \alpha |\downarrow\rangle_A + \beta |\uparrow\rangle_A$. This is the state we aim to teleport to atom B. State preparation is achieved by mapping the polarization of a weak coherent pulse onto the spin state of the atom using a STIRAP [44]. Entanglement between the spin state of atom B and the polarization of an ancilla photon C is generated using the scheme described in section 4.3.1.1, which ideally results in the maximally entangled state

$$\left|\Psi^-\right\rangle_{\mathrm{BC}} = \frac{1}{\sqrt{2}} \left(|\downarrow\rangle_B |\circlearrowleft\rangle_C - |\uparrow\rangle_B |\circlearrowright\rangle_C \right). \tag{5.31}$$

Photon C is sent to node A via an optical fiber, where the required Bell-state measurement is performed. For this purpose, the state of atom A is mapped onto the polarization of another photon A$'$. This allows us to perform an all-optical Bell-state measurement as was explained in section 5.2. According to Eq. (5.12), detecting the joint-polarization state $|\Psi^-\rangle_{\mathrm{A'C}}$ of the two photons directly heralds the successful state transfer from atom A to atom B. This heralding signal has to be communicated to node B to indicate that the state transfer succeeded. In our setup, it is moreover possible to identify the $|\Psi^+\rangle_{\mathrm{A'C}}$ state in the Bell-state measurement, which heralds the projection of atom B onto the state $\sigma_{\mathrm{x}} |\varphi\rangle_B$. In this case, the initial qubit from node A up to a phase flip is retrieved.

In order to characterize the fidelity of the teleportation protocol, the state of atom B is measured after a heralding event has been registered. For this purpose, the state of atom B is transferred to another photon B$'$ and quantum state tomography of its polarization state is performed for six different initial states at node A that form three mutually unbiased bases. As explained in section 3.3, combining these measurements enable a complete process tomography of the teleportation channel.

5.3.2. Teleportation fidelity

The fidelity of the overall process depends on the quality of the aforementioned steps. In this section, a simple model to estimate the teleportation fidelity as a function of the fidelity of these individual steps is derived.

We first define the combined fidelity of state preparation and state mapping as the overlap of the ideal state $|\varphi\rangle$ we intend to prepare, with the measured photonic polarization after state preparation and mapping $\rho_{\mathrm{A'}}$: $\mathcal{F}_A = \langle\varphi| \rho_{\mathrm{A'}} |\varphi\rangle$. We assume that errors made at node
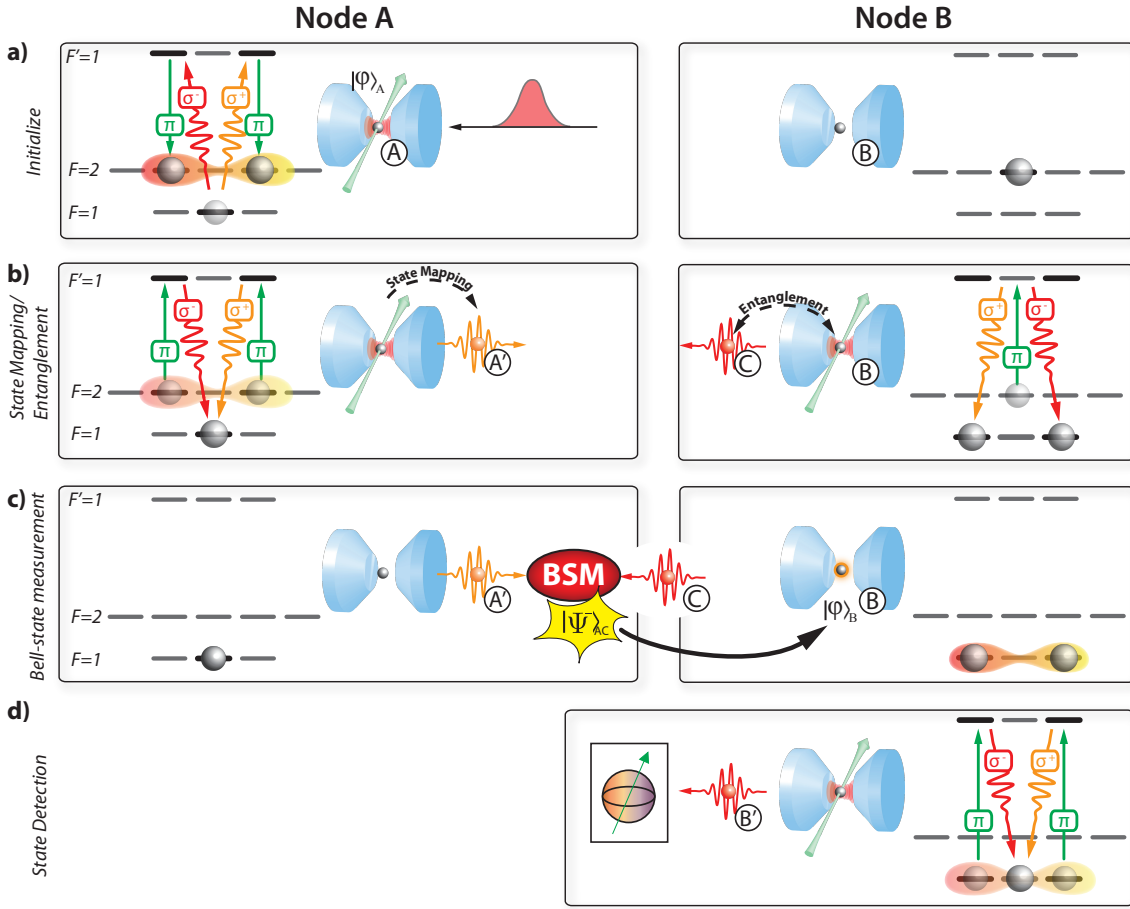
Figure 5.7.: Protocol for quantum teleportation between two remote atoms. At each node, a single atom is quasi-permanently trapped at the center of the cavity. **a)** Atom A is initialized in the state $|\varphi\rangle_{\mathrm{A}}$ by storing a coherent pulse with well-defined polarization. **b)** Entanglement is generated between atom B and an ancilla photon C. The atomic qubit at node A is mapped onto a photonic qubit A′. **c)** A Bell-state measurement (BSM) between the photons A′ and C is performed. Detection of a $|\Psi^-\rangle$ event heralds a successful state transfer. **d)** For detection of the state at node B, the atomic state is mapped onto the polarization of a single photon B′, whose polarization is subsequently analyzed.

A during state preparation and mapping result in the photonic state A′ being partially mixed, such that it can be written in the form

$$\rho_{\mathrm{A'}} = p_{\mathrm{A}} |\varphi\rangle \langle\varphi| + \frac{1}{2}(1 - p_{\mathrm{A}}) \mathbb{1}_2.$$

p_{A} is the probability that the state preparation and mapping results in the ideal state, and $\mathbb{1}_2$ denotes the identity operator in two dimensions. Using the definition of the state fidelity [Eq. (3.9)], the relation between p_{A} and the fidelity becomes

$$\mathcal{F}_{\mathrm{A}} = \langle\varphi| \rho_{\mathrm{A'}} |\varphi\rangle = \frac{1}{2}(p_{\mathrm{A}} + 1). \tag{5.32}$$

Similarly, we assume that the entangled state is of the form

$$\rho_{\text{ent}} = p_{\text{ent}} \left| \Psi^- \right\rangle \left\langle \Psi^- \right| + \frac{1}{4}(1 - p_{\text{ent}})\mathbb{1}_4,$$

where p_{ent} denotes the probability that the read-out atom-photon state is the ideal, maximally entangled Bell state $|\Psi^-\rangle$. In this case, the entanglement fidelity is

$$\mathcal{F}_{\text{ent}} = \left\langle \Psi^- \right| \rho_{\text{ent}} \left| \Psi^- \right\rangle = \frac{1}{4} + \frac{3}{4}p_{\text{ent}}. \tag{5.33}$$

We are interested in the state fidelity of atom B after teleportation. Let p_{w} be the probability for a wrong result during state detection, i.e. an event that reduces the visibility according to Eq. (3.10). Consequently, $1 - p_{\text{w}}$ is the probability to obtain a correct result. By using Eq. (3.11), the state fidelity at node B after teleportation can then be expressed as

$$\mathcal{F}_{\text{B}} = \frac{1}{2}\left(1 + \frac{(1 - p_{\text{w}}) - p_{\text{w}}}{(1 - p_{\text{w}}) + p_{\text{w}}}\right) = 1 - p_{\text{w}}. \tag{5.34}$$

The quality of two-photon interference affects the quality of the Bell-state measurement and is characterized by the interference contrast C (see section 5.2.3). According to the discussion in section 5.2.3, the ratio $P_{\parallel}^{(2)}/P_{\perp}^{(2)}$ is the probability that a photon pair impinging on the beam splitter *does not* show Hong-Ou-Mandel interference. Consequently, the contrast $C = 1 - P_{\parallel}^{(2)}/P_{\perp}^{(2)}$ is the probability that the photon pair *does* show Hong-Ou-Mandel interference. Following this argument, C is the probability for the case that a detected correlation in the Bell-state analyzer signaling a $|\Psi^-\rangle$ event has been caused by two photons that have actually been in the $|\Psi^-\rangle$ state. Particular emphasis has to be put on the fact that the influence of the interference contrast on the teleportation fidelity depends on the input state at node A. From the mutually unbiased basis states $\{|\mathcal{B}_i\rangle\}$, the states $|\downarrow_{\text{x}}\rangle$ and $|\uparrow_{\text{x}}\rangle$ are special because they are mapped onto eigenpolarizations of the detection basis of the Bell-state analyzer, H and V (see Appendix B). In this case, there is no need to detect the symmetry of the state, as classical polarization correlations between photons that did not interfere are sufficient to herald the projection of atom B onto the state initially prepared at atom A. Therefore, the fidelity is independent of the interference contrast. To make this point more clear, we consider the case where the initial state of atom A is $|\downarrow_{\text{x}}\rangle$. This state is mapped to a photon with polarization $|H\rangle$, which is jointly measured with a photon coming from node B in the Bell-state analyzer. Detection of a $|\Psi^-\rangle$ event (i.e. a correlation between H and V in different ports of the NPBS) signals that the two photons have been in orthogonal polarization states. Because the photon from node A was in the state $|H\rangle$, the signal in the V detector must have been caused by the photon from node B, independent of the interference between the two photons. Even if the polarization state of the photon from node B is correlated only classically with the spin state of atom B with respect to the H/V basis, the detection event projects the atom at node B onto the state $|\downarrow_{\text{x}}\rangle$. Classical correlations in the H/V basis refer to the polarization $V(H)$ being correlated with the atomic state $|\downarrow_{\text{x}}\rangle$ ($|\uparrow_{\text{x}}\rangle$), while polarizations states from the other mutually unbiased bases D/A and R/L being uncorrelated with the corresponding atomic state.

We first analyze the teleportation fidelity $\mathcal{F}_{\mathrm{B}}^{\perp}$ for the four input states $|\downarrow\rangle, |\uparrow\rangle, |\downarrow_{\mathrm{y}}\rangle, |\uparrow_{\mathrm{y}}\rangle$. The probability that the teleportation protocol succeeds is the product of the success probabilities of the individual steps. Following the preceding discussion, the probability for the protocol to succeed upon detection of a $|\Psi^-\rangle$ correlation is $Cp_{\mathrm{ent}}p_{\mathrm{A}}$. We assume, that whenever the teleportation protocol fails in spite of detection of a $|\Psi^-\rangle$ correlation (because of no interference or no entanglement or incorrect state preparation), the result of the state detection at node B is independent of the state we intended to prepare at node A, resulting in a fidelity of 1/2. This yields,

$$p_{\mathrm{w}} = \frac{1}{2}\left(1 - Cp_{\mathrm{ent}}p_{\mathrm{A}}\right). \tag{5.35}$$

Using Eq. (5.34) we find:

$$\mathcal{F}_{\mathrm{B}}^{\perp} = \frac{1}{2} + \frac{1}{2}Cp_{\mathrm{ent}}p_{\mathrm{A}}. \tag{5.36}$$

Using the expressions for p_{A} and p_{ent} from Eq. (5.32) and Eq. (5.33), respectively, this can be written as

$$\mathcal{F}_{\mathrm{B}}^{\perp} = \frac{1}{2} + \frac{4}{3}C\left(\mathcal{F}_{\mathrm{ent}} - \frac{1}{4}\right)\left(\mathcal{F}_{\mathrm{A}} - \frac{1}{2}\right). \tag{5.37}$$

An analogous analysis for the eigenpolarizations of the Bell-state analyzer $|\downarrow_{\mathrm{x}}\rangle$ and $|\uparrow_{\mathrm{x}}\rangle$, leads to

$$\mathcal{F}_{\mathrm{B}}^{\|} = \frac{1}{2} + \frac{4}{3}\left(\mathcal{F}_{\mathrm{ent}} - \frac{1}{4}\right)\left(\mathcal{F}_{\mathrm{A}} - \frac{1}{2}\right). \tag{5.38}$$

This corresponds to the result from Eq. (5.37) with $C = 1$ and is independent of the interference contrast. Averaging over $\mathcal{F}_{\mathrm{B}}^{\perp}$ and $\mathcal{F}_{\mathrm{B}}^{\|}$ for the six states $\{|\mathcal{B}_i\rangle\}$ results in the average state fidelity at node B after teleportation:

$$\overline{\mathcal{F}} = \frac{1}{2} + \frac{8}{9}\left(C + \frac{1}{2}\right)\left(\mathcal{F}_{\mathrm{ent}} - \frac{1}{4}\right)\left(\mathcal{F}_{\mathrm{A}} - \frac{1}{2}\right). \tag{5.39}$$

5.3.3. Experimental setup

After discussing the protocol and the fidelity, we now turn to the experimental implementation of quantum teleportation. Figure 5.8 shows a schematic of the experimental setup. In each system, single atoms are quasi-permanently trapped in a cavity using optical dipole traps (see chapter 2). The depths of the traps are different at the two nodes. The corresponding Stark shifts of the relevant transitions are 150 MHz ($|2, \pm 1\rangle \leftrightarrow |1, \pm 1\rangle'$ at node A) and 115 MHz ($|2,0\rangle \leftrightarrow |1,0\rangle'$ at node B), respectively. The π-polarized control laser fields that couple the hyperfine ground-state $F = 2$ to the excited hyperfine state $F' = 1$ have a detuning of 173 MHz with respect to the free atoms at both nodes. Taking the Stark shifts into account, the control fields are 23 MHz (node A) and 58 MHz (node B) blue detuned from the atomic transition. Both cavity fields couple the $F = 1 \leftrightarrow F' = 1$ transition and are in two-photon resonance with the control field.

The output modes of the cavities are coupled to single-mode fibers that direct the photons to the Bell-state analyzer, which is located in laboratory A. The output of these fibers is
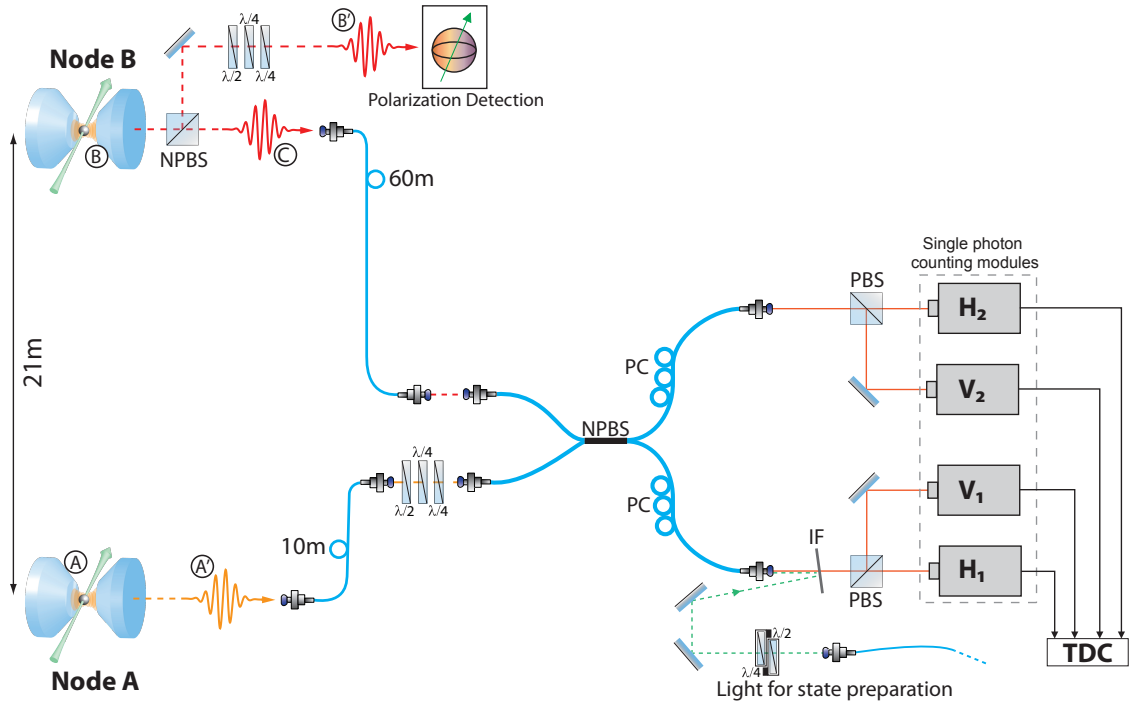
Figure 5.8.: Experimental setup for teleportation between two remote single atoms.
The state of atom A is mapped onto the polarization of a single photon A′. At node B, entanglement
is generated between the atom and a photon C. The two photons are coupled into single-mode fibers
and are directed to the Bell-state analyzer located in laboratory A. The photons are superimposed
on a fiber-based NPBS, whose output ports are monitored with four single-photon counting modules
which are connected to a time-to-digital converter (TDC). This allows us to perform a time-resolved
joint Bell-state measurement of the photons. The state of atom B after teleportation is determined
by generating another photon B′ and measuring its polarization. Polarization compensation of the
overall optical paths is achieved by using fiber-based polarization controllers (PC) and combinations
of half-wave ($\lambda/2$) and quarter-wave ($\lambda/4$) plates. To initialize atom A, a coherent laser pulse,
which polarization is set by two waveplates, is mapped onto the atomic spin state using STIRAP.
The laser is coupled into the cavity using reflection off an interference filter (IF).

free-space coupled into a fiber-based NPBS[9]. The beam splitter is the central element of
the Bell-state analyzer and its quality sets an upper bound for the achievable interference
contrast and hence for the achievable teleportation fidelity. The ratio between transmission
T and reflection R of the beam splitter is $\varrho = T/R = 1.1$. This corresponds to a maximal
achievable fringe visibility for a classical interference experiment of $V = \frac{2\sqrt{\varrho}}{\varrho+1} = 99.88\,\%$[10].
The visibility was measured using classical light fields to be $> 99\,\%$, proving that the
beam splitter is well suited for interference experiments. Each output port of the NPBS is
monitored using a combination of a PBS and two single-photon counting modules (SPCM).

---

[9]Gould, Corning PureMode HI 780-5/125

[10]The measured intensity in one output port of a beam splitter for two classical optical fields with relative
phase φ after interfering at the beam splitter is $I(\varphi) \propto \frac{1}{2} + \sqrt{TR}\cos(\varphi)$. The fringe visibility is defined
as $V = \frac{I_{\max}-I_{\min}}{I_{\max}+I_{\min}}$. With $I_{\max} = I(0)$ and $I_{\min} = I(\pi)$ the given formula for V can readily be derived.

The electronic pulses generated by the photon counters are recorded by a time-to-digital converter (TDC). From these data, correlation histograms between each combination of detector pairs can be created. There are in total six types of correlations between two different detectors in the depicted setup: $H_1V_1, H_2V_2, H_1H_2, V_1V_2, H_1V_2$ and V_1H_2 (for the labeling of the detectors see Fig. 5.8). According to section 5.2, correlations of the type H_1V_2 and V_1H_2 correspond to a detection of the $|\Psi^-\rangle$ state, whereas correlations of the type H_1V_1 and H_2V_2 correspond to the state $|\Psi^+\rangle$.

Compensation of unwanted polarization rotations. The optical components in the light path connecting the two laboratories lead to an unwanted rotation of the polarization of the light traveling along that path. This rotation must be compensated in order to measure in well-defined bases in both systems. To this end, we use half- and quarter-wave plates as well as in-line fiber polarization controllers that utilize bend-induced birefringence. These devices allow us to implement arbitrary rotations of the polarization state of light, thereby compensating any unwanted rotations in the overall setup (see section 4.2.2). To calibrate the compensation, we adjust the polarization controllers and waveplates such that light emerging from the cavities has the same polarization in both output ports of the NPBS, as well as in front of the polarization detector at node B.

5.3.4. Implementation of the protocol

In this section, the specific implementation of the individual steps involved in the teleportation protocol is explained. Each experimental run starts with the probabilistic loading of single atoms from a MOT into the cavity in both systems. As soon as a single atom is present in each cavity the protocol shown in Fig. 5.9 is started. It contains all the steps mentioned in section 5.3.1, which are explained in detail in the following.

State preparation at node A

To prepare the atomic state at node A, the polarization of a coherent laser pulse is mapped onto the spin state of the atom using a STIRAP (Fig. 5.7a). The laser is coupled into the high-transmissive mirror of cavity A after reflection off an interference filter. It was verified that the filter has no polarizing effect on the reflected light. The polarization of the light pulse and therefore the subsequent state of the atom is set by a half-wave and a quarter-wave plate.

Before the actual preparation is started, the atom is pumped to the hyperfine ground-state $F = 2$ and a π-polarized control laser pulse is applied to generate a single photon that is used as a reference for the evaluation of the data. By evaluating the $g^{(2)}$-correlation function of this photon it is possible to post-selectively discard experimental runs in which accidentally two or more atoms were trapped. The signature of a multi-atom event is $g^{(2)}(0)$ being significantly larger than zero. During evaluation of the data, experimental runs with $g^{(2)}(0) > 0.25$ are rejected. Additionally, this reference is used to estimate the efficiency of the state preparation process. Also at node B an additional photon in each
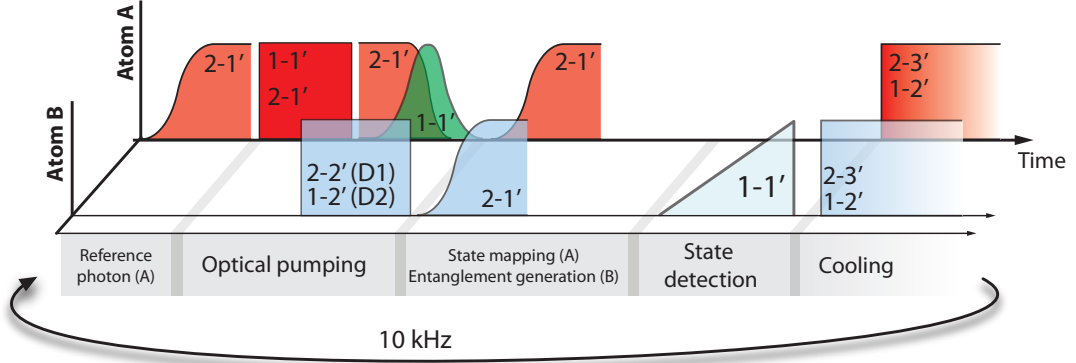
Figure 5.9.: Schematic of the experimental sequence for teleportation between two remote atoms. After generation of a single photon at node A, which is used as a reference for measuring the teleportation efficiency, the individual atoms are initialized by optical pumping. Thereafter, the atomic state of atom A is mapped onto the polarization of a single photon and entanglement between atom B and a single photon is generated. After detecting the state of atom B, a cooling interval ($\approx 80\,\mu\text{s}$) is applied to the atoms.

experimental run is generated (not shown in Fig. 5.9). The same criterion as for node A to discard multi-atom events is applied to node B.

Atom A is initialized in the state $|\varphi\rangle_{\text{A}} = \alpha\,|\downarrow\rangle_{\text{A}} + \beta\,|\uparrow\rangle_{\text{A}}$. The qubit basis states are encoded in $|\downarrow\rangle_{\text{A}} \equiv |F = 2, m_F = -1\rangle_{\text{A}}$ and $|\uparrow\rangle_{\text{A}} \equiv |F = 2, m_F = +1\rangle_{\text{A}}$. For this purpose, we employ the scheme described in section 4.2.1 to coherently map the polarization of a photon onto the atomic state. To achieve a high efficiency, we map the polarization of a coherent laser pulse with $\bar{n} \approx 5$ instead of a single photon onto the atom. This dramatically increases the preparation probability to almost unity, while the fidelity is not affected. To faithfully store the polarization and to maximize the efficiency, it is necessary to optically pump the atom into the state $|1,0\rangle$. By applying a π-polarized laser resonant with the $F = 1 \leftrightarrow F' = 1$ transition and a repump laser near-resonant with $F = 2 \leftrightarrow F' = 1$, the atomic population accumulates in $|1,0\rangle$ (see section 4.2.3). The light fields are applied simultaneously for a period of $5\,\mu\text{s}$. After pumping the atom, the control laser is switched on. The coherent laser pulse with a full width at half maximum of $280\,\text{ns}$, which is resonant with the cavity transition around $F = 1 \leftrightarrow F' = 1$ is sent onto the high-transmissive mirror. As soon as the pulse impinges onto the cavity, the Rabi frequency of the control laser is ramped down on a timescale of $300\,\text{ns}$. This maps the polarization state onto the atomic spin state [Eq. (4.10)]. The relative delay between the pulse and the switch-off time of the control is optimized for maximum storage efficiency [59].

To estimate the efficiency and the fidelity of the state preparation process, the atomic state is mapped onto the polarization of a single photon, which is measured with single-photon detectors locally in laboratory A. The efficiency is defined as the probability with which the atom is transferred from $F = 1$ to $F = 2$ in the storage process. This value can be measured by comparing the integrated counts of the reference photon with the integrated counts of the read-out photon. After optimization, a preparation efficiency close to unity was achieved. Due to long-term drifts in the course of the teleportation measurement

(approximately 60 hours), however, we find a reduced average preparation efficiency of 73 %. The reason is probably a slight drift of the control laser frequency with respect to the frequency of the cavity field. Variations on the order of a few 100 kHz already have a large impact on the storage efficiency [59], and consequently result in a reduced preparation efficiency. Another possible effect is a drift of the position of the dipole trap. This results in a drift of the Stark shift and the position of the atom with respect to the cavity mode. Both lead to a change of the dynamics of the STIRAP and consequently of the dynamics of the mapping process [148]. A reduced efficiency of the state preparation, however, does not necessarily affect the fidelity. The good quality of the preparation process is verified by measuring the fidelity of the read-out photon, defined as the overlap with the ideal state we intend to prepare. For the six mutually unbiased basis states, $\{|\mathcal{B}_i\rangle\}$, we find an average fidelity of $\mathcal{F}_\mathrm{A} \approx 95\,\%$.

Generation of atom-photon entanglement at node B

At node B, entanglement between the spin of the atom and the polarization of a photon C is generated using the scheme described in section 4.3.1.1 (Fig. 5.7b). After pumping the atom to the state $|2,0\rangle$, a π-polarized laser pulse that is in two-photon resonance with the cavity field couples the states $F = 2 \leftrightarrow F' = 1$ and drives a vSTIRAP which ideally results in the entangled atom-photon state of Eq. (5.31). The fidelity of the experimentally generated state with the ideal $|\Psi^-\rangle$ state is determined by mapping the atomic state onto a photonic polarization state using another vSTIRAP triggered by a π-polarized control pulse coupling the states $F = 1 \leftrightarrow F' = 1$. Measuring correlations between the polarizations of the two photons allows us to measure the entanglement witness and therefore the entanglement fidelity (see section 4.3.2). The result of this measurement therefore includes imperfections during mapping the state of atom B onto the photon. In the current experiment, the average value, including long-term drifts over 60 hours, is measured to be $\mathcal{F}_\mathrm{ent} = 89\,\%$.

Bell-state measurement

Photon C is directed to the Bell-state analyzer located in laboratory A. The qubit stored in atom A is mapped onto the polarization state of a photon A$'$. This is achieved by applying a control laser pulse, which is near-resonant with the transition $F = 2 \leftrightarrow F' = 1$ and in two-photon resonance with the cavity field, onto atom A. The photon is sent to the second input port of the Bell-state analyzer. Detection of a $|\Psi^-\rangle$ event for the joint Bell-state of the two photons heralds the successful teleportation from atom A to atom B.

State detection

The state of atom B after teleportation is measured by mapping the atomic spin-state onto the polarization of a photon B$'$ (Fig. 5.7d). This is accomplished by applying a π-polarized control pulse, which is in resonance with the frequency of the cavity field (near-resonant with the atomic $F = 1 \leftrightarrow F' = 1$ transition). This triggers the emission of a photon. By

using a detection setup (section 2.5) located in laboratory B, quantum state tomography of the photon and thus indirectly of the atom is performed.

Because the scheme used for the detection of the atomic state is the same as for the determination of the entanglement witness, imperfections during state detection are already included in the above quoted value for the entanglement fidelity $\mathcal{F}_{\mathrm{ent}}$.

5.3.5. Single photons made to interfere

In order to observe quantum interference and to perform a high-fidelity Bell-state measurement, it is crucial that the photons are indistinguishable, i.e. equal in polarization and frequency, and equal in their spatio-temporal mode. Because the photons emerge from independent sources, this is a very delicate task.

The spatial overlap is guaranteed by using a fiber-based beam splitter as described in section 5.3.3. The temporal profile and the frequency of the photonic wave packets can be controlled during the cavity-assisted photon generation process using an adiabatic passage. The physics of this process was already described in detail in section 4.1 and we will only focus on the particular implementation of the photon generation process employed in the teleportation protocol here.

Frequency. In order to generate photons of identical frequency, the control laser frequencies in both laboratories must be the same. To achieve this, the control lasers (a Ti:Sa laser at node A and a diode laser at node B, see chapter 2) are referenced to the output of a frequency comb that serves as an absolute frequency standard [51]. We check the relative frequency of the two lasers by detection of a beat note. The full $1/\mathrm{e}$-width of the spectral power density of the beat signal is $2\delta\nu = 800\,\mathrm{kHz}$ and represents an estimation of residual relative frequency fluctuations. Assuming a Gaussian frequency distribution, a formula for the achievable integrated contrast can be derived [146]:

$$C = \frac{1}{1 + \pi^2 \delta t^2 \delta\nu^2}.$$

As can immediately be seen from this equation, for photon lengths δt that are short compared to the inverse width of residual frequency variations $\delta\nu$, a frequency jitter has only a small impact on the contrast. In the present experiments we generate photons with a full width at half maximum of $\approx 250\,\mathrm{ns}$. The achievable contrast is then $C \approx 97\,\%$. Frequency jitter therefore has only a small influence on the quality of the two-photon interference.

Temporal shape. The temporal shape of the photonic wave packets can be engineered by adjusting the temporal shape of the control fields [95, 149]. As was discussed in section 4.1, the dynamics of the vSTIRAP depends on the strengths of the atomic transitions, the atom-cavity coupling and the detuning of the control laser with respect to the atomic resonance. Even if these parameters differ at the two nodes, photons with identical temporal envelope can be generated by choosing a suitable shape of the applied control laser pulse.

Figure 5.10.: Temporal shaping of single photon wave packets. Solid lines are measured data of ensemble averages. Dashed lines show approximately the applied control laser intensities. By choosing different slopes of the temporal course of the laser intensity (indicated by different colors) the photon length can be adjusted.
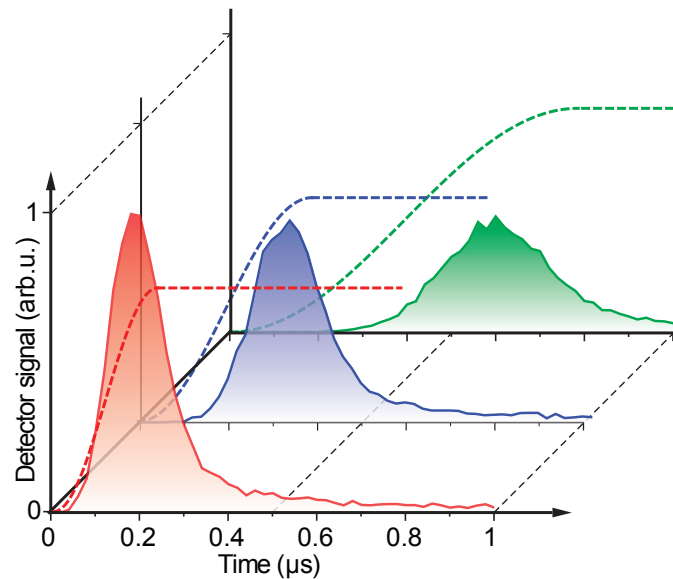
We aim to generate photons with a Gaussian profile, as this shape is proven to be most robust against fluctuations in the temporal mode in terms of the interference contrast [150]. We therefore apply a shape of the control laser intensity that approximately follows a $\sin^2$-function in time and settles at a constant value. Figure 5.10 shows three arrival-time histograms recorded with the single-photon detectors. They represent envelopes of photon wave packets for control pulse shapes that differ in the steepness of the leading edge. The maximum value of the laser power was set to $20\,\mu W$ for all shapes. The data shown in the figure demonstrate that the length of the symmetric photonic wave packet can be adjusted over a wide range without affecting the efficiency with which the photons are generated.

It must be noted that the measured arrival-time histograms always represent ensemble averages over independently generated photons. Thus, from these data no conclusions can be drawn about the individual photons and the underlying distribution of the photon shapes. In fact, it will turn out that these shot-to-shot variations in the photon generation process lead to a reduction of the interference contrast (see section 5.3.6).

Phase. As opposed to interference of classical optical fields, no interferometric stability on the scale of the wavelength is required for interfering single photons. Small shifts ($\ll \delta t$) between two photons do not influence the interference contrast. However, a phase shift *within* a photonic wave packet might have a measurable effect [151]. Such shifts can be caused by fluctuations in the optical fibers. Because the photons are short ($< 0.3\,\mu s$) compared to the timescale of acoustic noise ($\geq 100\,\mu s$), which could induce phase distortions in the fibers, we do not expect any influence of phase fluctuations on the interference contrast.

Synchronization. Because the optical Bell-state measurement requires photons in the same temporal mode, an accurate control of the timing of the experimental sequence is indispensable. In each setup, a digital pattern generator is used to control the precise

timing of the laser pulses (see chapter 2). System A hereby takes over the task of the master clock. Along with the start of the protocol at node A, an electronic signal is sent to the pattern generator at node B to trigger the start of the protocol at node B. This guarantees relative temporal stability between the two experiments.

Signal propagation time.   Any delay of the signals between the single-photon detectors and the TDC leads to an inaccurate measurement of the detection-time differences. As this reduces the achievable interference contrast, the discrepancies between signal propagation times have to be kept as small as possible. To measure the propagation times we use a weak, short coherent laser pulse with a steep, linear rising edge ($\approx 20\,\text{ns}$)[11] and couple it into one port of the fiber-based NPBS. The light pulse triggers all photon counters simultaneously. The relative signal propagation times can then be measured with high accuracy at the TDC. After adjusting the relative signal delay by changing cable lengths in the different paths, the residual arrival time differences of the electronic signals is measured to be $< 3\,\text{ns}$.

5.3.6. Two-photon quantum interference

According to the theoretical treatment in section 5.2.3, a measurement of correlations between detectors in different output ports of the NPBS for parallel and orthogonally polarized photons (non-interfering case as a reference) is necessary to determine the interference contrast [see Eq. (5.20)]. This can for example be achieved by placing polarization filters in front of the NPBS to prepare photons of well-defined polarization and performing the interference experiment for parallel and orthogonally polarized photons. Our approach, however, uses randomly polarized photons (i.e. they are in a statistical mixture of polarizations) at one input (from node B) and photons with a fixed polarization at the second input (from node A). When the photons are detected in the Bell-state analyzer, they are projected onto certain polarizations. We thus refer to the correlations of the type $H_1 H_2$ and $V_1 V_2$ as the joint detection probability for parallel polarized photons $P_\parallel^{(2)}$, and to the correlations of the type $H_1 V_2$ and $V_1 H_2$ as the joint detection probability for orthogonally polarized photons $P_\perp^{(2)}$. Experimentally, the contrast is calculated according to Eq. (5.20),

$$C = 1 - \frac{P_\parallel^{(2)}}{P_\perp^{(2)}} = 1 - \frac{N_\text{c}(H_1 H_2) + N_\text{c}(V_1 V_2)}{N_\text{c}(H_1 V_2) + N_\text{c}(V_1 H_2)}, \tag{5.40}$$

where $N_\text{c}(j)$ denotes the number of detected correlations of the type j. This of course assumes identical efficiencies of all four detectors. For unequal detector efficiencies ε_k ($k = H_1, V_1, H_2, V_2$) the measured contrast becomes

$$C = 1 - \frac{P_\parallel^{(2)}(\varepsilon_{H1}\varepsilon_{H2} + \varepsilon_{V1}\varepsilon_{V2})}{P_\perp^{(2)}(\varepsilon_{H1}\varepsilon_{V2} + \varepsilon_{V1}\varepsilon_{H2})} = 1 - \frac{P_\parallel^{(2)}}{P_\perp^{(2)}}\frac{r_1 r_2 + 1}{r_1 + r_2}, \tag{5.41}$$

---

[11]Generated with a fiber-based electro-optical amplitude-modulator with a bandwidth of $10\,\text{GHz}$.
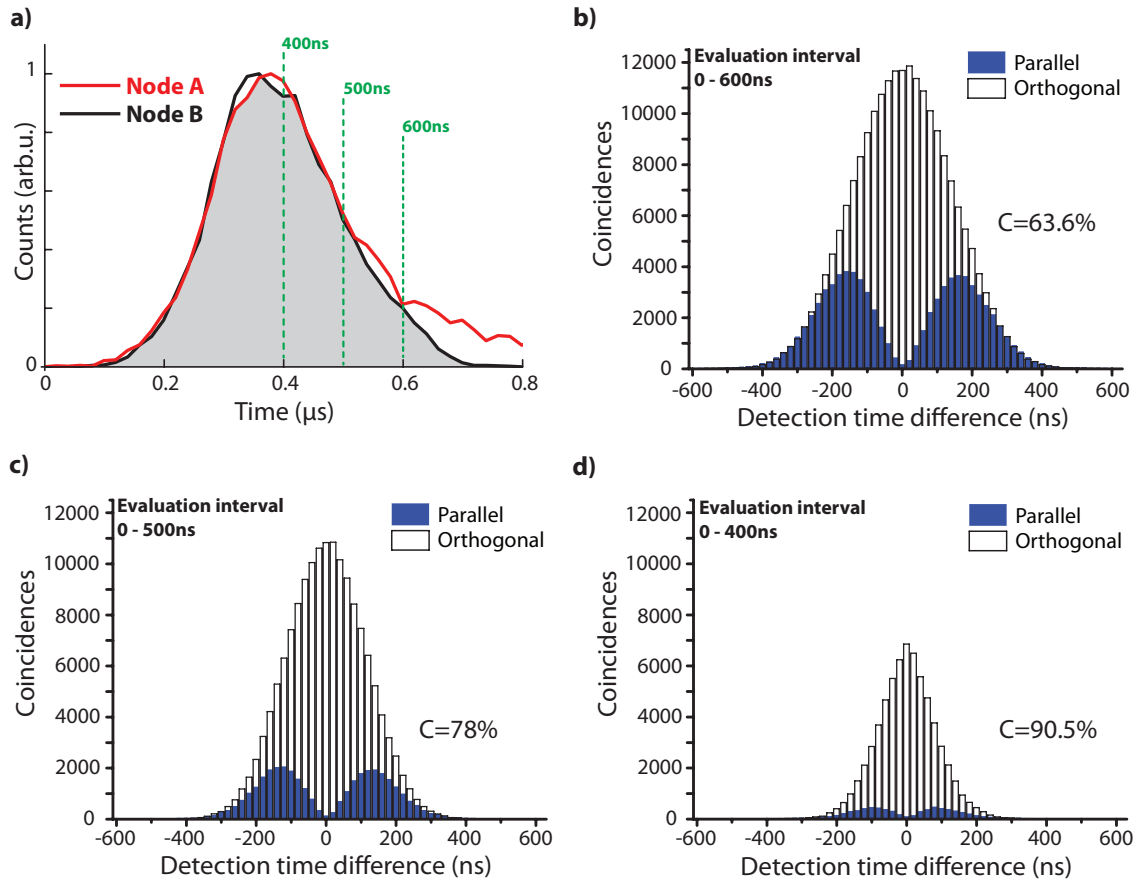
Figure 5.11.: a) Arrival-time histograms of photons emerging from node A (red) and node B (black). The full width at half maximum of the two nearly Gaussian-shaped photons is 250 ns. **b)-d) Joint-detection probability for parallel (blue filled bars) and orthogonally (black open bars) polarized photons.** The correlation histograms are shown for different evaluation intervals as defined by the dashed green lines in the arrival time histogram in a). The evaluation interval always starts at time zero.

with $r_1 = \varepsilon_{H1}/\varepsilon_{V1}$ and $r_2 = \varepsilon_{H2}/\varepsilon_{V2}$. Therefore, only differences in the same output port of the NPBS are of relevance. In our setup, we measure $r_1 = 1.07$ and $r_2 = 0.91$ so that the correction factor on the right-hand side of Eq. (5.41) becomes 0.997. The influence of detector efficiencies is small and is neglected in the following. Consequently, Eq. (5.40) is used to determine the contrast. Because the polarization of the photons from node B is random, both types of correlations (parallel and orthogonal) are equally probable. The measured correlation functions are therefore correctly normalized.

The vSTIRAP is employed to generate photons with identical envelopes at both nodes (Fig. 5.11a) by tuning the temporal shape of the applied control laser pulse (see section 5.3.5 and Fig. 5.10). The full width at half maximum of the integrated arrival-time histograms is 250 ns and the temporal overlap of the Gaussian shaped envelopes is almost perfect. The overlap integral computed between the envelope of the histograms has a value of $> 99\%$, when evaluating photons with an arrival time of up to 600 ns. The slight deviation in the falling edge of the pulse is due to non-perfect state preparation of the atom at
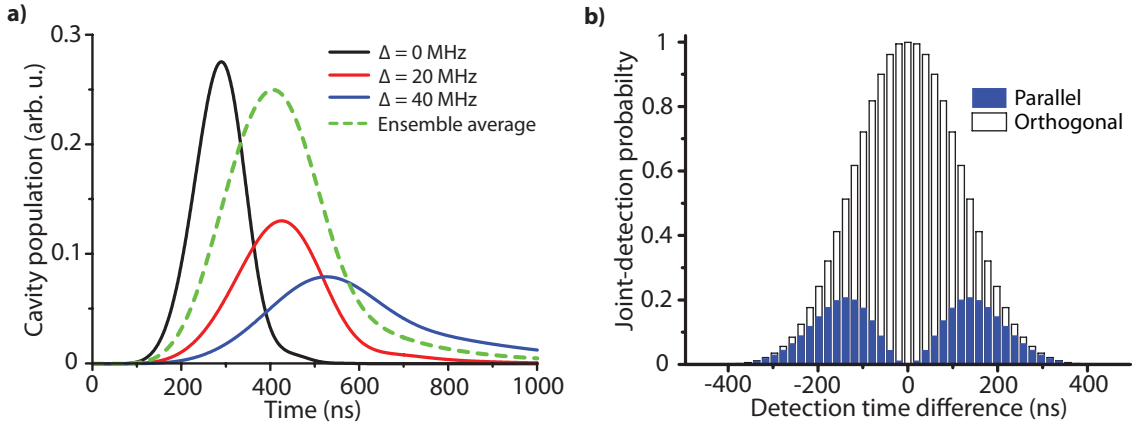
Figure 5.12.: Numerical simulation of photon generation and two-photon interference.
a) Examples of single-photon wave packets for different detunings Δ of the control and cavity field from the atomic resonance (solid black, red and blue lines). The ensemble average (dashed green line) is computed using a Monte Carlo method, according to the measured Stark shift variation of 8 MHz. **b)** Joint-detection probability for parallel and orthogonally polarized photons, computed for the same ensemble average as in a).

node A (cf. section 4.2.4). Events with an arrival time later than 600 ns are discarded in the following. Figure 5.11b shows the joint-detection probability for parallel $P_{\parallel}^{(2)}(\tau)$ and orthogonal polarizations $P_{\perp}^{(2)}(\tau)$ as a function of the detection time difference τ, where only photons within an evaluation interval of 600 ns of the wave packet envelopes are considered. The integrated contrast C as defined in Eq. (5.21) for the data shown in Fig. 5.11b is 63.6 % and clearly proves the quantum nature of the two-photon interference. Restricting the evaluation interval further by discarding detection events at the end of the photon, the contrast can be increased. The values for an interval of 500 ns and 400 ns are $C = 78\%$ and $C = 90.5\%$, respectively.

The measured dependence of the joint-detection probability on the detection-time difference for parallel and orthogonally polarized photons is now discussed. It can be explained by variations in the emission time of individual single photon wave packets (see section 5.2.3). To gain more insight into the physical mechanism causing these variations and their impact on the interference contrast, we perform a numerical simulation. The finite temperature of the atoms inside the trapping potential leads to fluctuating Stark shifts and consequently to fluctuating detunings of the control and cavity field with respect to the atomic transition. This detuning in turn affects the temporal dynamics of the photon generation process (see section 4.1). The Stark shift variations result in an inhomogeneous broadening of the atomic linewidth. By performing spectroscopy of the trapped atom, we find this broadening to be 8 MHz. Details on the simulation can be found in Appendix C. The principle is as follows: First, single-photon wave packets are simulated by solving the master equation of the system. Then, the integral of Eq. (5.17) is computed numerically for parallel and orthogonal polarizations using Eq. (5.18) and Eq. (5.19). Using a Monte Carlo method, the ensemble averages of the wave packets and of $P_{\parallel}^{(2)}(\tau)$ and $P_{\perp}^{(2)}(\tau)$ according to the measured distribution of the Stark shift is calculated. The result is shown
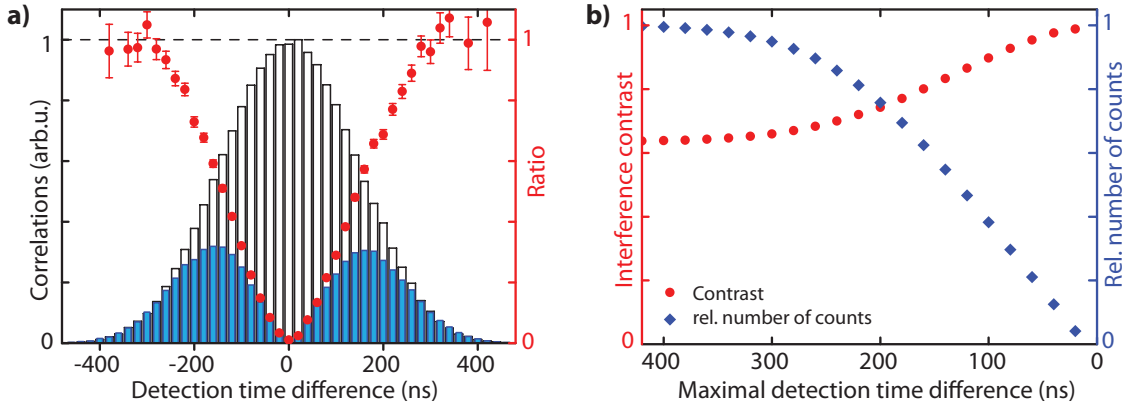
Figure 5.13.: Time-resolved two-photon interference. a) Result of the time-resolved corre-
lation measurement for photons with parallel (blue filled bars) and orthogonal (black open bars)
polarization in opposite output ports of the NPBS. The number of coincidences between photons
with the same polarization is strongly suppressed. The red data points show the ratio $P_\parallel^{(2)}/P_\perp^{(2)}$ for
each pair of binned correlations. The error bars indicate the statistical standard error. **b)** Integrated
interference contrast $C(T)$ [red points, Eq. (5.42)] and relative number of evaluated counts (blue
diamonds) as a function of the maximal detection time difference for a two-photon correlation in
different output ports of the NPBS. By post-selecting on short detection time differences, the inter-
ference contrast can be greatly enhanced. All statistical error bars are smaller than the respective
symbols. The data in a) and b) are shown for a coincidence interval of 600 ns (cf. Fig. 5.11).

in Fig. 5.12. The ensemble average of the photonic wave packet (Fig. 5.12a) corresponds to
the measured arrival-time histogram shown in Fig. 5.11a. The calculated joint-detection
probabilities (Fig. 5.12b) yield an interference contrast of 75 %, which is higher than what
is experimentally observed. Nevertheless, although the calculations are based on simplified
assumptions, for example with respect to the motion of the atoms (see Appendix C),
the result exhibits good qualitative agreement with the measured data (Fig. 5.11b). We
therefore conclude, that the finite temperature of the atom is the major contribution to
the non-perfect interference contrast.

In accordance with the theoretical expectation, the number of correlations between detectors
in different output ports of the NPBS and with identical polarization is almost zero for a
small time interval around $\tau = 0$ (Fig. 5.13a). For larger intervals the integrated contrast is
reduced, as fluctuations in the temporal modes as well as possible frequency differences [94]
between the photons play a more significant role (red data points in Fig. 5.13a). Similar to
the definition of the contrast in Eq. (5.21), an integrated contrast with limited bounds is
defined:

$$C(T) = 1 - \frac{\int_{-T}^{T} P_\parallel^{(2)}(\tau)\mathrm{d}\tau}{\int_{-T}^{T} P_\perp^{(2)}(\tau)\mathrm{d}\tau}. \tag{5.42}$$

The symmetric integration limit T defines a coincidence time window within which events
are considered for evaluating the interference contrast. Figure 5.13b shows the integrated
contrast $C(T)$ as a function of the time window T. By reducing the width of the time
window it is possible to increase the interference contrast to almost unity. For time
differences shorter than 20 ns, the contrast is 98.9 %. This proves that the Bell-state
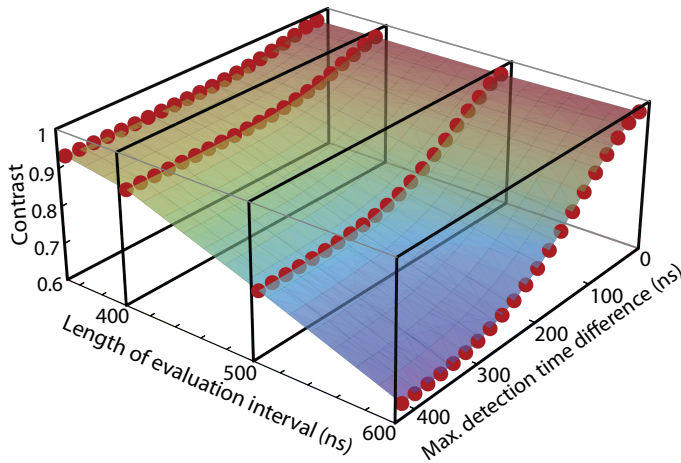
Figure 5.14.: Interference contrast as a function of the evaluation interval and the detection time difference. The red points are measured data. The surface is an interpolation between these points.

analyzer is well aligned and that each cavity system emits true single photons. At the same time, the number of events contributing to the evaluation of the contrast naturally decreases.

The dependence of the interference contrast on both, the evaluation interval (cf. Fig. 5.11) and the detection time difference is shown in Fig. 5.14.

The dependence of the contrast on the detection time difference leads to a strategy to increase the teleportation fidelity. Using the detection time difference between two photons as an additional heralding condition results in a dramatic increase of the interference contrast, and consequently of the teleportation fidelity (see section 5.3.2). The reduced number of events contributing to the Bell-state measurement then leads to a decreased efficiency of the teleportation protocol.

5.3.7. Teleportation results

After we analyzed the interference properties of the photons, and thereby the quality of the optical Bell-state measurement, we now turn to the discussion of the results of the teleportation experiment.

The integrated arrival-time histogram of the photons used in the Bell-state measurement is shown in Fig. 5.11a. We evaluate photon correlations in the interval from 0 to 0.6 µs. Detection of a correlation that corresponds to the $|\Psi^-\rangle$ state heralds a successful state transfer and projects atom B directly onto the state of atom A. For the time being, we apply no additional heralding condition by setting no restriction on the detection time difference within the evaluation interval.

5.3.7.1. Efficiency

We can only detect two of the four equally probable Bell states and do not apply an inverse unitary rotation that would be needed in case of a $|\Psi^+\rangle$ event. The efficiency of our scheme, conditioned on a $|\Psi^-\rangle$ detection, is thus intrinsically limited to 1/4. The relevant factors

Quantity	Value	Meaning
η_{A}	0.39	Photon generation efficiency at node A.
η_{B}	0.25	Photon generation efficiency at node B.
T_A	0.62	Probability for a photon from node A to be transmitted to a detector in the Bell-state analyzer.
T_B	0.24	Probability for a photon from node B to be transmitted to a detector in the Bell-state analyzer. Includes additional NPBS and one additional fiber compared to T_A.
ε^{D}	0.55	Quantum efficiencies of the single-photon detectors.
T_{out}	0.9	Outcoupling efficiency of the cavities into one single mode.

Table 5.2.: Efficiencies of the individual steps involved in the teleportation experiment.

yielding the teleportation efficiency are given in Table 5.2. T_{out} is the outcoupling efficiency of the cavities into one single free-space mode, $T_{\mathrm{A/B}}$ is the probability for a photon from node A/B to be transmitted to the Bell-state analyzer and ε^{D} is the quantum efficiency of the single-photon detectors. The probability to detect an intracavity photon in the Bell-state analyzer is then given by $P_{\mathrm{A/B}}^{\mathrm{det}} = T_{\mathrm{out}}T_{\mathrm{A/B}}\varepsilon^{\mathrm{D}}$ for node A and B, respectively. With the photon generation efficiencies η_{A} and η_{B}, the probability to register a photon in one of the detectors per photon-production attempt becomes $\xi_{\mathrm{A}} = \eta_{\mathrm{A}}P_{\mathrm{A}}^{\mathrm{det}} = 0.12$ and $\xi_{\mathrm{B}} = \eta_{\mathrm{B}}P_{\mathrm{B}}^{\mathrm{det}} = 0.03$, respectively. The probability for a detected two-photon correlation is then $\xi_{\mathrm{A}}\xi_{\mathrm{B}} = 0.36\,\%$. Consequently, the probability to register a $|\Psi^-\rangle$ Bell state is $\frac{1}{4}\xi_{\mathrm{A}}\xi_{\mathrm{B}} = 0.09\,\%$. The probability to detect a dark count in one of the detectors within the evaluation interval of $0.6\,\mu\mathrm{s}$ is $\sim 10^{-5}$. The probability of a dark count together with a single photon from either of the two atoms to trigger a $|\Psi^-\rangle$ event is on the order of 10^{-6}. As this number is three orders of magnitude smaller than the success probability of the teleportation protocol, the contribution of dark counts to the result of the Bell-state measurement does not play a role.

The experiment is repeated at a rate of $10\,\mathrm{kHz}$. When a single atom is trapped in each of the cavities, the rate of teleportation events is 10 per second. The duty cycle (the fraction of time during which a single atom is trapped in both systems) is approximately 0.25, averaged over the whole measurement time of 60 hours. This results in an effective rate of heralded teleportation events of ~ 2 per second. Including state preparation of qubit A (efficiency $73\,\%$, see section 5.3.4) and detection of state B (efficiency $2.4\,\%$, including generation of the mapping photon and its detection), we find the rate of evaluated events for the tomography to be 0.6 per minute. The contribution of dark counts during state detection is again negligible.

5.3.7.2. Fidelity

In order to characterize the fidelity of the teleportation protocol, we perform complete quantum process tomography (see section 3.3). For this purpose, we use a set of six states $\{|\mathcal{B}_i\rangle\} = \{|{\downarrow}\rangle, |{\uparrow}\rangle, |{\downarrow_{\mathrm{x}}}\rangle, |{\uparrow_{\mathrm{x}}}\rangle, |{\downarrow_{\mathrm{y}}}\rangle, |{\uparrow_{\mathrm{y}}}\rangle\}$ forming three mutually unbiased bases as input states at node A. For each input state, quantum state tomography of the corresponding

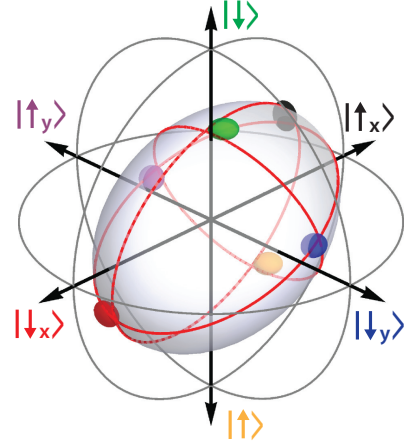| Input state	Fidelity (%)
$\left|\downarrow\right\rangle$	74.5 ± 2.6
$\left|\uparrow\right\rangle$	72.3 ± 2.8
$\left|\downarrow_y\right\rangle = \frac{1}{\sqrt{2}}\left(\left|\downarrow\right\rangle + i\left|\uparrow\right\rangle\right)$	73.0 ± 3.0
$\left|\uparrow_y\right\rangle = \frac{1}{\sqrt{2}}\left(\left|\downarrow\right\rangle - i\left|\uparrow\right\rangle\right)$	75.0 ± 3.0
$\left|\downarrow_x\right\rangle = \frac{1}{\sqrt{2}}\left(\left|\downarrow\right\rangle + \left|\uparrow\right\rangle\right)$	88.6 ± 2.3
$\left|\uparrow_x\right\rangle = \frac{1}{\sqrt{2}}\left(\left|\downarrow\right\rangle - \left|\uparrow\right\rangle\right)$	90.2 ± 2.5
Average	$\mathbf{78.9 \pm 1.1}$

Figure 5.15.: Quantum process tomography of the teleportation channel. The table shows the individual state fidelities of node B after teleportation, for six mutually unbiased input states of node A. The quoted errors are the statistical standard error. **Right:** Visualization of the process in Stokes space. The size of the colored ellipsoids represents the statistical standard error.

output state at node B after teleportation conditioned on a $\left|\Psi^-\right\rangle$ detection in the Bell-state measurement is performed. The resulting state fidelities with respect to the six different input states which are assumed to be ideal, $\langle\mathcal{B}_i|\,\rho_{\mathrm{B'}}\,|\mathcal{B}_i\rangle$, are listed in the table in Fig. 5.15. We find for the average state fidelity $\overline{\mathcal{F}} = (78.9 \pm 1.1)\,\%$, a value that is more than ten standard deviations above the threshold of $2/3$ that could be achieved by classical means [101]. The measured fidelity includes imperfections during state preparation and readout of node A, and the atom-to-photon state mapping employed for state readout at node B, and is therefore a lower bound to the fidelity of the teleportation itself (section 5.3.2). It can clearly be seen that the fidelities for the input states $\left|\downarrow_x\right\rangle$ and $\left|\uparrow_x\right\rangle$ are significantly higher than for the remaining four states, as was discussed in section 5.3.2.

To perform process tomography on the teleportation channel, we take the output density matrices of all six input states $\{|\mathcal{B}_i\rangle\}$ into account. The process matrix is reconstructed with respect to the Pauli operators σ_i using the maximum-likelihood technique. We find that the underlying process is not trace-preserving. Therefore, the results from section 3.3.2 are used to compute the fidelity. The fact that the tomography yields a non-trace-preserving process will be discussed in section 5.3.7.4. The process fidelity is found to be $\mathcal{F}_{\mathrm{proc}} = (68.6 \pm 1.0)\,\%$. From this value, the average state fidelity can be computed using Eq. (3.15) to be $(79.1\pm1.1)\,\%$. This value agrees with the average state fidelity obtained from the individual state fidelities and therefore proves the quality of the maximum-likelihood fit. Figure 5.15 shows the effect of the process on all possible input states in Stokes space. The reconstructed sphere is obtained using the process matrix, which was calculated using the maximum-likelihood approach. The aforementioned differences between the states $\{\left|\downarrow_x\right\rangle, \left|\uparrow_x\right\rangle\}$ and $\{\left|\downarrow\right\rangle, \left|\uparrow\right\rangle, \left|\downarrow_y\right\rangle, \left|\uparrow_y\right\rangle\}$ results in the ellipticity of the sphere.

The measured overall fidelity depends on the quality of the individual steps employed in the protocol. The interference contrast is $C = 64\,\%$ (section 5.3.6). The fidelity of the entangled state is $\mathcal{F}_{\mathrm{ent}} = 89\,\%$ and the fidelity of the state preparation of atom A is $\mathcal{F}_{\mathrm{A}} = 95\,\%$

(section 5.3.4). According to the discussion in section 5.3.2, the expected teleportation fidelity is $\overline{\mathcal{F}} = 79.2\,\%$. This value is in excellent agreement with the experimentally obtained fidelity.

5.3.7.3. Time-resolved Bell-state measurement

As was discussed in section 5.3.6, the time-resolved Bell-state measurement allows us to implement an additional heralding condition by using only correlations between photons with detection-time differences that do not exceed a certain value. For short detection-time differences, the interference contrast increases (see Fig. 5.13). Because the achievable average teleportation fidelity directly depends on the contrast, see Eq. (5.39), the fidelity is consequently also increased. For example, reducing the coincidence time window to 80 ns increases the contrast to 92.8 % and the average fidelity of the teleported states to $\overline{\mathcal{F}} = (88.0 \pm 1.5)\,\%$. At the same time, the efficiency is reduced to 0.04 %. Correspondingly, the reconstructed Bloch sphere shown in Fig. 5.16a has an increased volume compared with the one shown in Fig. 5.15. Figure 5.16b shows the process matrix as an alternative representation of the teleportation process. The dominant element is $\chi_{00} = 0.652$ and proves the good preservation of coherence during the protocol. The non-trace-preservation of the process results in the trace of the matrix being smaller than 1: $\mathrm{Tr}[\chi] = 0.792$. The value of of χ_{00} corresponds to a process fidelity of the non-trace-preserving process of $\mathcal{F}_{\mathrm{proc}} = \chi_{00}/\mathrm{Tr}[\chi] = 82.3\,\%$ [Eq. (3.19)]. The calculated average state fidelity obtained from $\mathcal{F}_{\mathrm{proc}}$ and Eq. (3.15) is 88.2 % and agrees with the measured average state fidelity $\overline{\mathcal{F}}$.

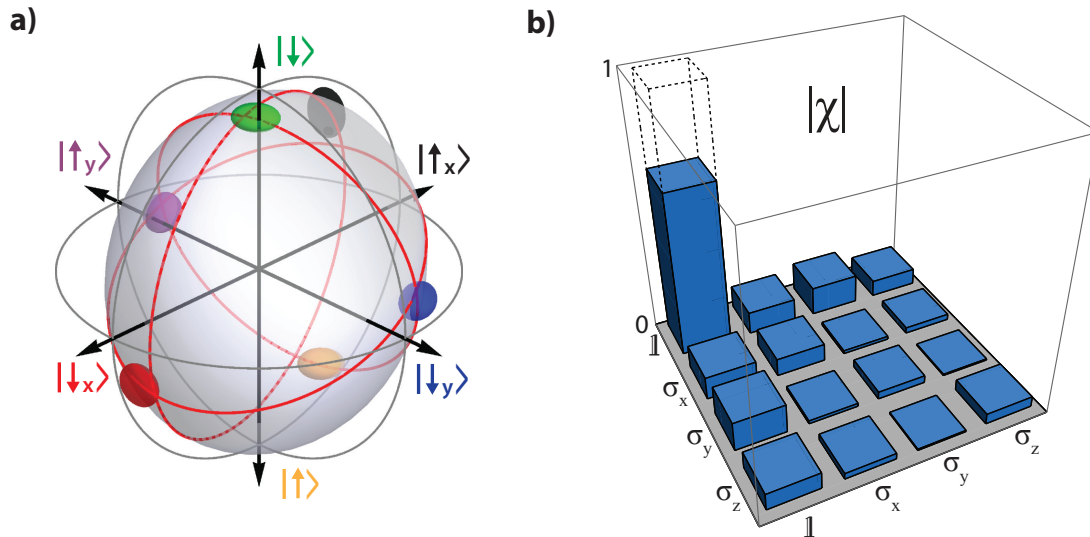In accordance with the model for the teleportation fidelity derived in section 5.3.2, the

Figure 5.16.: Quantum process tomography of the teleportation channel with temporal heralding. a) Visualization of the process in Stokes space. The size of the colored ellipsoids represents the statistical standard error. **b)** Absolute values of the reconstructed process matrix χ. The dashed bar corresponds to the matrix of the ideal process ($\chi_{00} = 1$).
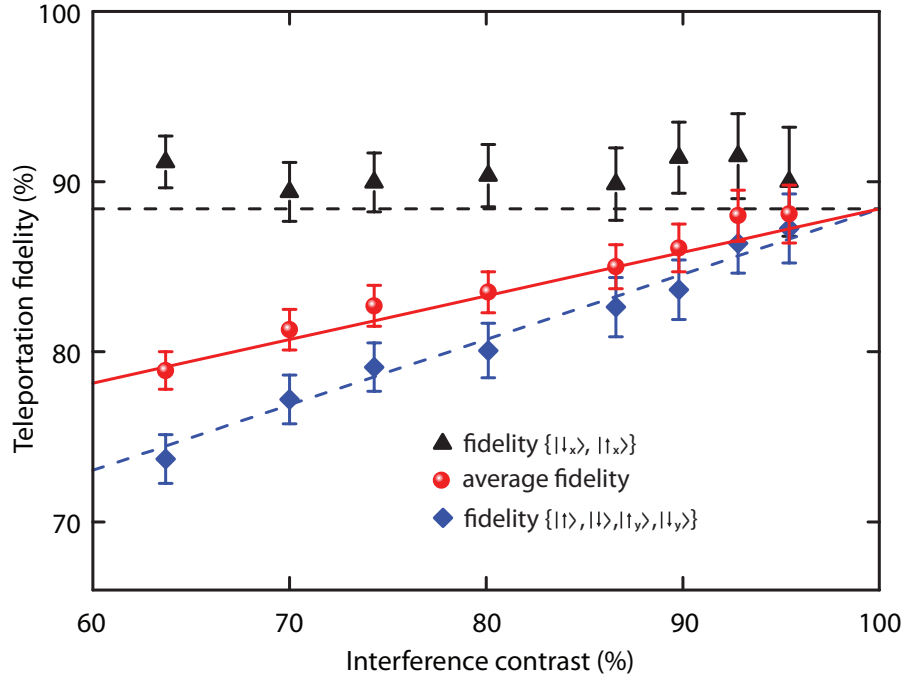
Figure 5.17.: Teleportation fidelity as a function of the interference contrast. Increasing the contrast by using the time-resolved Bell-state measurement increases the fidelity of the teleportation protocol. Black triangles are measured average fidelities for the two input states $|\downarrow_x\rangle$ and $|\uparrow_x\rangle$. The blue diamonds are averages over the other four input states $|\downarrow\rangle$, $|\uparrow\rangle$, $|\downarrow_y\rangle$, and $|\uparrow_y\rangle$. The red points represent the mean fidelity averaged over all six input states. The lines are the theoretical expectations according to the model presented in section 5.3.2.

relation between the fidelity and the contrast depends on the input state. Figure 5.17 shows the average fidelity for the states $\{|\downarrow\rangle, |\uparrow\rangle, |\downarrow_y\rangle, |\uparrow_y\rangle\}$ (blue), the average fidelity for the states $\{|\downarrow_x\rangle, |\uparrow_x\rangle\}$ (black) and the average for all six input states (red). The lines correspond to the theoretical prediction according to Eq. (5.37), Eq. (5.38) and Eq. (5.39) with the independently measured values $\mathcal{F}_{\mathrm{ent}} = 89\,\%$ and $\mathcal{F}_{\mathrm{A}} = 95\,\%$ (see section 5.3.4). Without a free parameter, the model exhibits excellent agreement with the measured data.

The second type of correlations that can be identified with the Bell-state analyzer is the $|\Psi^+\rangle$ state. It does not, however, project the receiver atom to the state of the sender atom $|\varphi\rangle$, but induces a unitary rotation σ_x [see Eq. (5.12)]. To complete the teleportation process, we would have to reverse this rotation by applying the inverse unitary operation. In our experiment, this step is missing. Nevertheless, we can compute the fidelity with respect to the states $\{\sigma_x|\mathcal{B}_i\rangle\}$. This gives an upper bound for the teleportation fidelity via $|\Psi^+\rangle$. Conditioned on a $|\Psi^+\rangle$ correlation in the Bell-state measurement, we find an average state fidelity of $\overline{\mathcal{F}} = (82.4 \pm 1.1)\,\%$, which is slightly higher than the value we obtain for $|\Psi^-\rangle$. Applying the additional heralding condition by reducing the coincidence window to 80 ns increases the fidelity to $(91.2 \pm 1.2)\,\%$. The reconstructed Bloch sphere and the process matrix for this case are shown in Fig. 5.18. The missing local operation σ_x manifests itself in a rotation of the reconstructed Bloch sphere by π around the axis
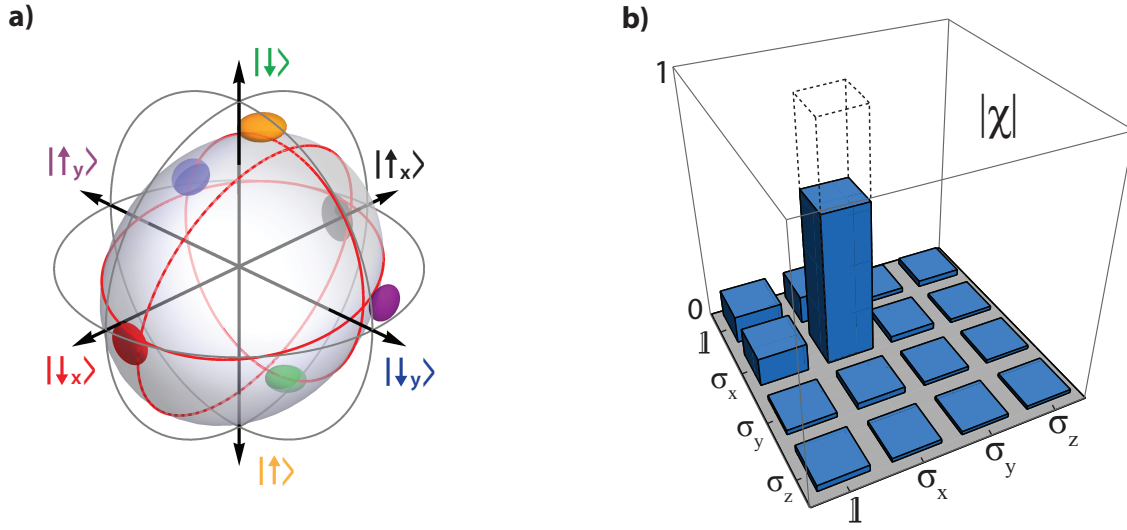
a)

b)

Figure 5.18.: Quantum process tomography of the teleportation channel with temporal heralding, conditioned on the detection of a $|\Psi^+\rangle$ Bell state. a) Visualization of the process in Stokes space. The unitary operation σ_x, corresponding to a rotation by π around the axis defined by the states $|\downarrow_x\rangle$ and $|\uparrow_x\rangle$, is clearly visible. The size of the colored ellipsoids represents the statistical standard error. **b)** Absolute values of the reconstructed process matrix χ. The dashed bar corresponds to the matrix element of the ideal process including the unitary operation σ_x ($\chi_{11} = 1$).

defined by the states $|\downarrow_x\rangle$ and $|\uparrow_x\rangle$. The dominant element of the reconstructed process matrix is χ_{11} as expected from Eq. (3.3).

5.3.7.4. Non-trace-preservation of the process

As was already mentioned in the discussion of the tomography results, we find the teleportation process to be non-trace-preserving. From the process matrix χ that we obtain for the measurement shown in Fig. 5.15, the trace is $\mathrm{Tr}[\chi] = 0.79 < 1$. Following the theoretical treatment in section 3.3.2, the operator $\mathcal{P}$ defined in Eq. (3.17) can be used to characterize a non-trace-preserving process. For the aforementioned process matrix χ this operator reads

$$\mathcal{P} = \begin{pmatrix} 0.801 & -0.184 + 0.094i \\ -0.184 - 0.094i & 0.785 \end{pmatrix}. \tag{5.43}$$

This matrix is Hermitian and has the eigenvalues $\lambda_1 = 1$ and $\lambda_2 = 0.59$, with corresponding eigenvectors $|\lambda_1\rangle$ and $|\lambda_2\rangle$. The eigenvectors are illustrated in Stokes space in Fig. 5.19a. They lie on the equator of the unit Bloch sphere and correspond to linearly polarized photonic states that are rotated with respect to the states H and V by $14°$. According to the theoretical treatment in section 3.3.2, input states of the quantum process, i.e. states initially prepared at node A, that are equal to $|\lambda_1\rangle$ or $|\lambda_2\rangle$ are teleported with different probabilities, λ_1 and λ_2, respectively. Input states that are superpositions of $|\lambda_1\rangle$ and $|\lambda_2\rangle$ are shifted towards the eigenstate with the larger eigenvalue λ_1. The eigenstates coincide to a good approximation with the states $|\uparrow_x\rangle$ and $|\downarrow_x\rangle$. This is the reason for the fact that
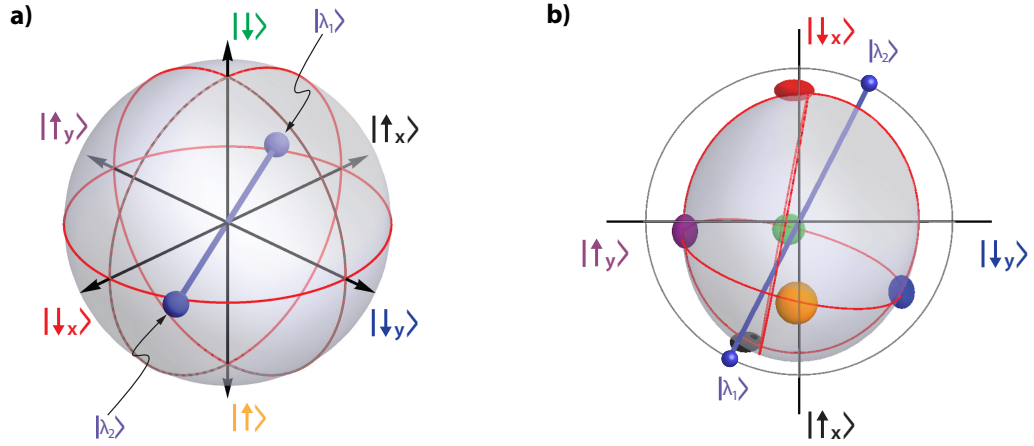
Figure 5.19.: Non-trace preservation of the teleportation process. a) The two eigenstates $|\lambda_1\rangle, |\lambda_2\rangle$ of the matrix $\mathcal{P}$ from Eq. (5.43) are shown in Stokes space (blue spheres). **b)** Bloch sphere from Fig. 5.16 viewed along the z-axis. It can clearly be seen that the states $\{|\downarrow\rangle, |\uparrow\rangle, |\downarrow_y\rangle, |\uparrow_y\rangle\}$ are shifted towards the state $|\lambda_1\rangle$.

the reconstructed states corresponding to the input states $\{|\downarrow\rangle, |\uparrow\rangle, |\downarrow_y\rangle, |\uparrow_y\rangle\}$ are shifted towards the state $|\uparrow_x\rangle$ (see Fig. 5.15-5.18 and Fig. 5.19b).

There are several possible reasons that can explain that the overall process does not preserve the trace. It could for example be some optical elements that have a slight polarizing effect. Another possibility is birefringence of the cavities. This effect would lead to a dependence of the resonance frequency of the cavity on the polarization of the mode, and results in different photon generation efficiencies for different polarizations. If, for example, the two eigenmodes of the birefringent cavity coincide with the polarization states H and V, and the frequency of the control field matches the resonance frequency of the mode corresponding to V-polarization, the generation efficiency of V-polarized photons is larger than the efficiency of H-polarized photons. In this case, the atom-photon mapping would distort the assignment between atomic and photonic qubits (Fig. B.2 in Appendix B) in such a way, that the qubit states are shifted towards $|\uparrow_x\rangle$. At node A, a birefringent resonator would therefore distort the state to be teleported during the atom-to-photon mapping process, which is used to implement the optical Bell-state measurement. However, the birefringence of the cavity of node A was measured and the effect was found to be small compared to the linewidth of the cavity [59]. Due to the aforementioned effect on the atom-to-photon mapping, birefringence of the cavity at node B would also affect the generated atom-photon entangled state, as well as the atom-to-photon state mapping during readout of the receiver qubit at node B. This in turn would lead to a distortion of the measured teleported states. A detailed quantitative analysis of the birefringence of this resonator might be of interest for future investigations.

6. Summary and outlook

In this thesis, the faithful transfer of quantum information between two single atoms at a distance of 21 m is demonstrated using the complementary methods of direct quantum state transfer and quantum teleportation. Each atom is trapped at the center of a high-finesse optical cavity, resulting in a highly efficient interface between light and matter. The two atom-cavity systems are located in different laboratories and are operated independently of one another. In the first part of the thesis, the light-matter interface is exploited to realize a *direct quantum state transfer* using single photons as information carriers. Our results constitute the first direct coupling of two distant single quantum emitters via single photons. In the second part, *quantum teleportation* of arbitrary qubits between two distant atoms is demonstrated. The direct transfer is the conceptually most simple way to communicate between material qubits and is in principle deterministic. This approach will be advantageous for realizations of quantum networks on the meter to kilometer scale, where the direct transport of material qubits and the state transfer using microwave photons would be a formidable challenge. Teleportation on the other hand, requires the implementation of a more sophisticated protocol, but has the advantage that it is intrinsically heralded and can be implemented in quantum repeater architectures, which allow for quantum communication on a global scale. The distance between the communication parties of 21 m represents the current record for matter-matter teleportation.

In the following, the two experiments are compared with respect to efficiency and fidelity of the state transfer. Moreover, potential improvements of our setup and prospects of cavity-based quantum networks are discussed.

For the direct transfer, the probability to successfully communicate a state between the two atoms is 0.2 %. One limitation of the efficiency in the current implementation is the photon generation efficiency at the sender site, which is deliberately kept low to suppress off-resonant excitations to nearby hyperfine states. This problem is not present for qubits encoded in the $F = 2$ manifold and could be circumvented by a local transfer of the qubit from $F = 1$ to the $F = 2$ manifold using optical Raman or microwave pulses. Since single-photon generation efficiencies of 60 % have been observed in our setup [92], an increase of the transfer efficiency by one order of magnitude seems feasible. For the teleportation experiment, the measured efficiency is 0.1 %. Compared to previous realizations with single atoms in free space, the use of cavities boosts the overall efficiency by almost five orders of magnitude [132]. It is now only two orders of magnitude away from the maximum value of 50 % that can be achieved with linear-optics schemes [145]. In our experiment, the efficiency is not predominantly limited by the single-photon generation and collection efficiency, but by the requirement to transmit and detect two photons simultaneously, which is inherent in the optical Bell-state measurement. Taking the experimental rates of 5 kHz for the direct transfer and 10 kHz for teleportation into account, both schemes would allow for a possible

rate of 10 transferred qubits per second in the current implementation. Our experiments puts quantum communication between material qubits into a regime where the time needed for a successful transmission event (about $0.1\,\mathrm{s}$, corresponding to the transfer rate of $10\,\mathrm{Hz}$) is shorter than coherence times observed in single atoms [152]. This is an indispensable requirement in quantum repeater architectures to maintain coherence in the individual nodes while long-distance entanglement is built up using a repeat-until-success scheme.

One limitation of the efficiencies in the described experiments is the moderate atom-cavity coupling strength g. Efficiencies approaching unity for the atom-to-photon and the photon-to-atom state mapping processes may be accomplished when the cavity mode volume is decreased. This can be achieved for example by using fiber-based optical cavities [153, 154], which are currently an active and exciting field of research. Moreover, the efficiency of the storage process, and consequently the efficiency of the direct state transfer, could be increased by impedance matching [148]. By elaborately selecting the temporal shape of the control laser, the amount of light reflected off the cavity can be further minimized. In addition, trapping an ensemble of atoms in the cavity would allow us to employ collective effects to dramatically increase the storage efficiency [155]. The last approach, however, would dismiss the advantages of single-particle network nodes.

We analyze both, direct transfer and teleportation, using quantum process tomography. Fidelities exceeding the classical threshold of $2/3$ prove the quantum nature of the underlying processes. The fidelity of the direct transfer was found to be $84\,\%$, while for the teleportation we achieve a fidelity of $79\,\%$. In both experiments, non-perfect state preparation of the atoms limits the achievable fidelity. In the teleportation experiment, non-perfect interference of the photons is an additional source of error. By implementing an additional heralding condition based on a time-resolved Bell-state measurement, the influence of this effect can be minimized. We achieve a fidelity of up to $88\,\%$, while reducing the efficiency to $0.04\,\%$. The fidelities of both schemes could be enhanced by improving optical pumping, which is used to initialize the atoms for photon storage and entanglement generation. Additionally, cooling the atoms to their motional ground state [54] would minimize variations of the atom-cavity coupling strength and of the Stark shift. As this would improve the indistinguishability of the generated single photons, the teleportation fidelity would increase.

The aforementioned increase of the teleportation fidelity by using a time-resolved Bell-state measurement is a universal technique and can be employed in any optical Bell-state measurement with sufficient temporal resolution. Using vSTIRAP for photon production allows us to tune the frequency of the emitted photons and consequently allows for the creation of frequency-matched photons even though the transition frequencies at the two nodes are different, for example due to different environmental influences. In our setup, the atomic transitions differ by six atomic linewidths due to the different Stark shifts induced by the dipole traps. This demonstrates the ability to teleport a quantum state between non-identical memories and opens up new perspectives for solid-state-based approaches to quantum networks. These systems, such as quantum dots or nitrogen-vacancy centers in diamond, generally suffer from different transition frequencies of sender and receiver [156–159].

The current implementation of the direct state transfer does not include a herald. For our system based on single-atom cavity nodes, however, the implementation is conceptually

straightforward [160]. The successful storage process is associated with a change of the atomic hyperfine state. The depopulation of the initial state can then be probed spectroscopically, using cavity-assisted hyperfine state detection [64, 161, 162]. As the splitting between the two hyperfine ground states in ^{87}Rb is large, optical probing of the $F = 1$ population on the closed transition $F = 1 \leftrightarrow F' = 0$ should leave the qubit stored in $F = 2$ unaltered. The main challenge is to detect the population in $F = 1$ with high fidelity before off-resonant excitations lead to decay into $F = 2$, that is, with only a few scattered photons. As numerical simulations show, the implementation is challenging with our cavities. It is, however, certainly feasible with current cavity technology [162].

The efficiency of our current implementation of the Bell-state measurement used for teleportation is limited. It is, however, possible to perform a complete and deterministic Bell-state measurement in our system [160, 163]. This requires the implementation of a deterministic controlled-NOT gate between the sender atom and the photonic part of the entangled Bell pair. The protocol could be implemented as follows [160]: Two atoms are trapped simultaneously in the cavity of the sender. The qubit to be teleported is stored in one of the atoms. Entanglement is generated between the second atom and the atom of the receiver [45, 164]. The interaction of the two atoms with the cavity mode can now be employed to perform the controlled-NOT gate between the atoms, by mapping the state of the first atom onto the second atom [165]. Subsequent detection of the state of the second atom [64, 161, 162] completes the Bell-state measurement. As this scheme discriminates all four Bell states, it is in principle deterministic. The proposed protocol requires the ability to trap and individually address two single atoms in one cavity.

Our results demonstrate that cavity-based systems are very promising candidates for the realization of quantum networks with arbitrary topologies. The current network could be extended to more complex geometries with more than two nodes by using only classical optics. The direct state transfer has also been exploited to generate entanglement between two distant single atoms. By creating entanglement between an atom and a photon as a first step, and then transferring the photon to and storing it in the distant atom, entanglement between the two atoms can be generated [45]. The demonstrated optical Bell-state measurement in the teleportation experiment can also be applied to perform entanglement swapping [47, 103, 164] as required for the experimental realization of a quantum repeater. The use of cavities and the resulting success probabilities offer a clear perspective for scalability, thus paving the way towards large-scale quantum networks. Moreover, our approach to quantum teleportation allows for the implementation of a complete and deterministic Bell-state measurement that would be an important step towards the realization of a quantum repeater for long-distance quantum communication.

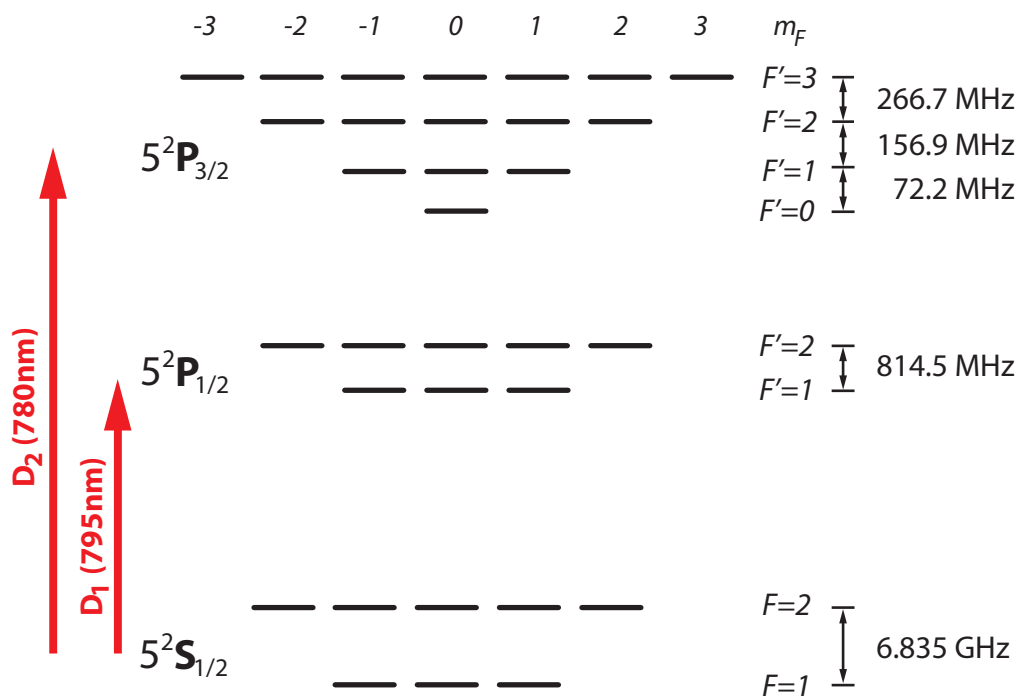# A. Level structure of the ^{87}Rb D$_1$ and D$_2$ line

Figure A.1.: Detailed level structure of the ^{87}Rb D$_1$and D$_2$ line [100]. The shown structure is not to scale.

B. Atomic qubit and photonic polarization

A $\sigma^-(\sigma^+)$ transition is defined as a transition that decreases (increases) the magnetic quantum number m_F by 1 upon absorption of a photon. A π transition leaves m_F unchanged. The quantization axis of the system is chosen to be the cavity axis. π transitions can be driven by shining in light along a direction that is perpendicular to the cavity axis, and linearly polarized along that axis. The helicity of photons propagating along the quantization axis is defined with respect to the opposite direction of the beam propagation. Right-handed polarization (R) rotates clockwise, while left-handed polarization (L) rotates counter-clockwise. $R(L)$ polarized light drives $\sigma^-(\sigma^+)$ transitions.
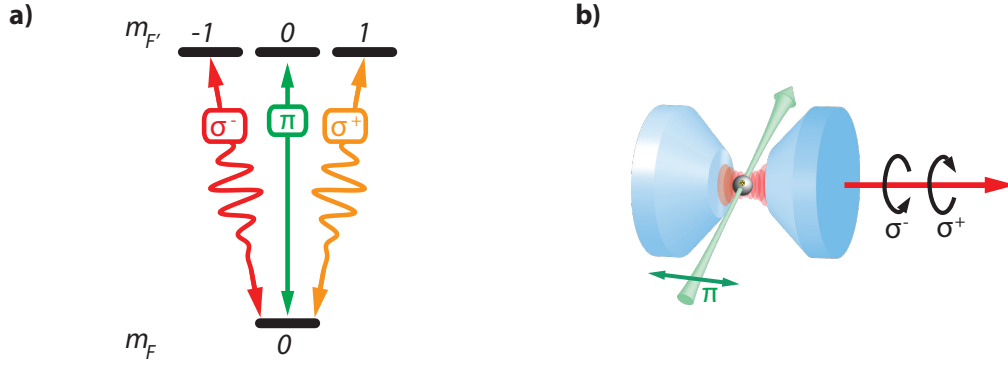

Figure B.1.: Definition of the quantization axis. a) The polarization components $\sigma^\pm$ are defined with respect to the atomic transition. **b)** Polarization components in the laboratory frame of reference.

Atomic qubit	Composition	Photon polarization
$|\!\downarrow\rangle$		$|R\rangle\,(|\circlearrowright\rangle)$
$|\!\uparrow\rangle$		$|L\rangle\,(|\circlearrowleft\rangle)$
$|\!\downarrow_\text{x}\rangle$	$\frac{1}{\sqrt{2}}\left(|\!\downarrow\rangle + |\!\uparrow\rangle\right)$	$|H\rangle = \frac{1}{\sqrt{2}}\left(|\circlearrowright\rangle + |\circlearrowleft\rangle\right)$
$|\!\uparrow_\text{x}\rangle$	$\frac{1}{\sqrt{2}}\left(|\!\downarrow\rangle - |\!\uparrow\rangle\right)$	$|V\rangle = \frac{1}{\sqrt{2}}\left(|\circlearrowright\rangle - |\circlearrowleft\rangle\right)$
$|\!\downarrow_\text{y}\rangle$	$\frac{1}{\sqrt{2}}\left(|\!\downarrow\rangle + i\,|\!\uparrow\rangle\right)$	$|D\rangle = \frac{1}{\sqrt{2}}\left(|\circlearrowright\rangle + i\,|\circlearrowleft\rangle\right)$
$|\!\uparrow_\text{y}\rangle$	$\frac{1}{\sqrt{2}}\left(|\!\downarrow\rangle - i\,|\!\uparrow\rangle\right)$	$|A\rangle = \frac{1}{\sqrt{2}}\left(|\circlearrowright\rangle - i\,|\circlearrowleft\rangle\right)$

Table B.1.: Definition of atomic and photonic qubits. The photonic polarization in the right column is the polarization state of a photon that is emitted from an atom in the corresponding state. Equivalently, if a properly initialized atom absorbs a photon with a fixed polarization, the final atomic state is the corresponding one from the left column.

Figure B.2 shows the equivalence between atomic spin states and photonic polarization states. Bloch and Poincaré sphere are treated equivalently.
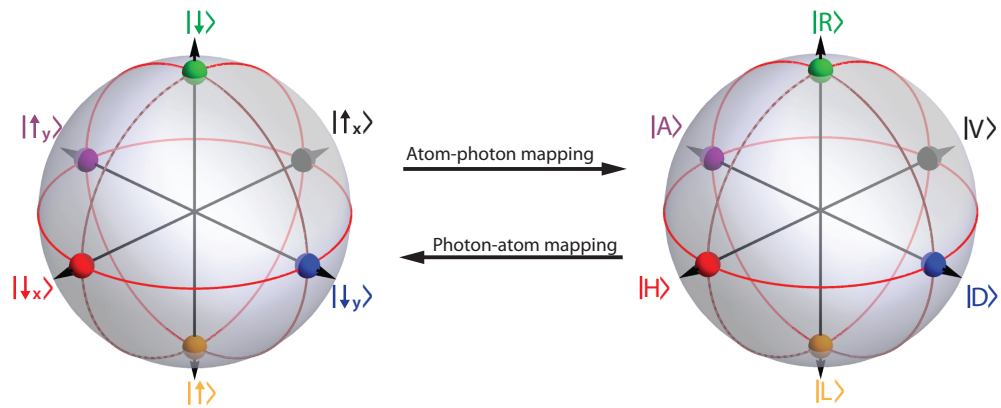

Figure B.2.: Correspondence between the Bloch sphere (left) and the Poincaré sphere (right). Atom-photon mapping transfers atomic onto photonic qubits. Photon-atom mapping does the reverse process (cf. Tab. B.1).

C. Numerical simulations

C.1. Dynamics of the atom-cavity system

The temporal evolution of the atom-cavity state $\rho(t)$ is governed by the master equation [166]

$$\frac{\mathrm{d}}{\mathrm{d}t}\rho(t) = -\frac{i}{\hbar}\left[H(t),\rho(t)\right] + \mathcal{L}\left[\rho(t)\right]. \tag{C.1}$$

The first term of the right-hand side describes the coherent evolution of the state according to the Hamilton operator $H(t)$. The coupling of the atomic states and of the cavity field to the environment is described by the Lindblad operator $\mathcal{L}$. The Hamiltonian is comprised of a stationary and an interaction part: $H = H_{\mathrm{stat}} + H_{\mathrm{int}}$. We transform the system to a frame that rotates with the frequency of the control laser ω_L and neglect fast-rotating terms (rotating-wave-approximation). In the rotating frame, the energy of the atomic ground states are raised by the laser frequency.

The stationary Hamiltonian contains an atomic and a cavity part:

$$H_{\mathrm{stat}} = H_{\mathrm{atom}} + H_{\mathrm{cavity}} = \sum_{g,e}\left(\Delta_L\left|g\right\rangle\left\langle g\right| + \Delta_e\left|e\right\rangle\left\langle e\right|\right) + \Delta_{LC}a^\dagger a. \tag{C.2}$$

The atomic part is a sum over all ground states $\left|g\right\rangle$ and excited states $\left|e\right\rangle$. $\Delta_L = \omega_0 - \omega_L$ is the detuning of the laser with respect to an excited state with frequency ω_0 that serves as the reference level with zero energy. $\Delta_e = \omega_0 - \omega_e$ is the frequency of the excited state ω_e with respect to the reference state. $\Delta_{LC} = \omega_C - \omega_L$ is the detuning of the cavity field with respect to the rotating frame. If the control laser is in two-photon resonance with the cavity, it is $\Delta_{LC} = 0$.

The interaction part describes the coupling between atomic states (induced by a control laser with Rabi frequency Ω) and the coupling between the atom and the cavity field (induced by the atom-cavity coupling g):

$$H_{\mathrm{int}} = \sum_{g,e} g_{ge}\left|g\right\rangle\left\langle e\right|a^\dagger + \frac{1}{2}\Omega_{ge}\left|g\right\rangle\left\langle e\right| + \mathrm{H.c.} \tag{C.3}$$

The coupling strengths g_{ge} and Ω_{ge} depend on the matrix element of the respective transition $\left|g\right\rangle \leftrightarrow \left|e\right\rangle$ [100]. The atom-cavity coupling on the $F = 1 \leftrightarrow F' = 1$ transition of the D_2 line is $g_0/2\pi = 5.1\,\mathrm{MHz}$. The cavity couples atomic states with $m_F \rightarrow m_F \pm 1$ ($\sigma^\pm$ transitions). Because the atom is not in its motional ground state, it moves considerably along the cavity axis. This is taken into account by assuming a reduced coupling constant $g = 0.6g_0$ [51]. The control field with Rabi frequency Ω drives π-transitions from the ground states with $F = 2$ to the excited states.

The Lindblad operator $\mathcal{L}$ describes the decay of excited atomic and cavity states:

$$\mathcal{L}\left[\rho(t)\right] = \sum_{ge} \gamma_{eg} \left(2 \left|g\right\rangle \left\langle e\right| \rho \left|e\right\rangle \left\langle g\right| - \left|e\right\rangle \left\langle e\right| \rho - \rho \left|e\right\rangle \left\langle e\right|\right)$$
$$+ \kappa \left(2 a \rho a^\dagger - a^\dagger a \rho - \rho a^\dagger a\right). \tag{C.4}$$

The master equation is solved in Python using *QuTiP* [167]. To minimize computation time, the Fock space of the cavity is restricted to maximally one excitation.

The simulated photonic wave packets in Fig. 4.6a are computed for different initial atomic states. Figure C.1 shows the atomic level structure used in the calculation. A detailed analysis of the Stark shifts induced by the π-polarized light of the FORT [168], results in differential shifts of excited states with different quantum numbers F' and $m_{F'}$. The simulation starts with an empty cavity and the atom in state $|2, m_F\rangle$. A control pulse with a $\sin^2$-shape is switched on. After 800 ns it settles at a Rabi frequency of $\Omega/2\pi = 14\,\mathrm{MHz}$ on the transition $|2,0\rangle \leftrightarrow |1,0\rangle'$. Control and cavity field are both 20 MHz blue detuned from the excited atomic state $|1, \pm 1\rangle'$. All atomic ground states and the excited states of the $F' = 1$ and $F' = 2$ manifolds are considered in the simulation. Figure 4.6a shows the expectation value of the number operator of the cavity field $\langle a^\dagger a\rangle$ as a function of time.
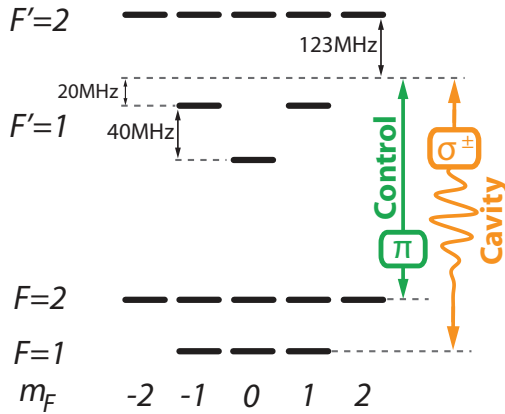

Figure C.1.: Atomic level structure used in the simulation in section 4.2.4. The different energies of the Zeeman states are caused by differential Stark shifts induced by the dipole trap.

C.2. Monte Carlo simulation of two-photon interference

A spectroscopic measurement of the linewidth of a single atom inside the optical dipole trap yields a Lorentzian shaped profile with a full width at half maximum of 14 MHz. Given the natural linewidth of 6 MHz, this means that the atomic resonance is inhomogeneously broadened by 8 MHz. We thus assume a Lorentz distribution of Stark shifts for the atom in the dipole trap:

$$f(\Delta) = \frac{1}{w\pi \left(1 + \frac{(\Delta - \Delta_0)^2}{w^2}\right)}, \tag{C.5}$$

with a width $2w/2\pi = 8\,\mathrm{MHz}$ around the mean value $\Delta_0/2\pi = 20\,\mathrm{MHz}$. Photonic wave packets for different detunings $\Delta = \Delta_L$ are precomputed by solving the master equation.

We assume the control field to be in two-photon resonance with the cavity field ($\Delta_{LC} = 0$). The initial condition of the system is an empty cavity and the atomic state is $|2, +1\rangle$. The control pulse has a $\sin^2$-shape and settles after $700\,\text{ns}$ at a Rabi frequency of $25\,\text{MHz}$ on the transition $|2,0\rangle \leftrightarrow |1,0\rangle'$. All atomic ground states and the excited states of the $F' = 1$ manifold are considered. Three examples of simulated photons are shown in Fig. 5.12a. The ensemble average is computed using a Monte Carlo method. Random numbers are generated from the Lorentz distribution $f(\Delta)$. Each number corresponds to a detuning value. By summing over many photons according to the random detunings, the ensemble average is obtained.

The simulation of two-photon interference is performed by repeating the following steps:

- Generate two independent random numbers from the Lorentz distribution $f(\Delta)$.

- Compute $G_{\parallel}^{(2)}$ and $G_{\perp}^{(2)}$ [Eq. (5.18) and Eq. (5.19)] for a pair of precomputed photonic wave packets for Stark shifts Δ corresponding to the random numbers.

- Compute $P_{\perp}^{(2)}$ and $P_{\parallel}^{(2)}$ by solving the integral of Eq. (5.17) numerically.

For the computation of $G_{\parallel}^{(2)}$ and $G_{\perp}^{(2)}$, only the interval between 0 and $0.6\,\text{µs}$ of the photonic wave packets, as in the evaluation of the measured data, is taken into account (cf. 5.12a). By repeating these steps several times (10000 times for the result shown in Fig. 5.12), the joint-detection probabilities as a function of the detection-time difference in Fig. 5.12b are obtained.

It must be noted, that the used model is very simple. It assumes, that the atom does not move during the process of single-photon generation, i.e. the coupling g and the detuning (Stark shift) are assumed to be constant during vSTIRAP. A more rigorous model would have to include a temporal varying coupling and detuning. Moreover, the model disregards any influence of frequency fluctuations as well as frequency differences of the photons, which could be caused by non-adiabatic corrections in the photon generation process [93]. Nevertheless, the simple model exhibits good qualitative agreement with the measurement result.

Bibliography

[1] T. H. Maiman. Stimulated Optical Radiation in Ruby. *Nature* **187**, 493–494 (1960).

[2] R. G. Henderson. Nuclear magnetic resonance imaging: a review. *Journal of the Royal Society of Medicine* **76**, 206–212 (1983).

[3] J. C. Bergquist, S. R. Jefferts and D. J. Wineland. Time Measurement at the Millennium. *Physics Today* **54**, 37 (2001).

[4] J. P. Dowling and G. J. Milburn. Quantum technology: the second quantum revolution. *Philosophical transactions. Series A, Mathematical, physical, and engineering sciences* **361**, 1655–1674 (2003).

[5] V. Giovannetti, S. Lloyd and L. Maccone. Quantum Metrology. *Physical Review Letters* **96**, 010401 (2006).

[6] M. Reed, J. Randall, R. Aggarwal, R. Matyi, T. Moore and A. Wetsel. Observation of discrete electronic states in a zero-dimensional semiconductor nanostructure. *Physical Review Letters* **60**, 535–537 (1988).

[7] I. Bloch. Ultracold quantum gases in optical lattices. *Nature Physics* **1**, 23–30 (2005).

[8] J. Wrachtrup and F. Jelezko. Processing quantum information in diamond. *Journal of Physics: Condensed Matter* **18**, S807–S824 (2006).

[9] R. J. Schoelkopf and S. M. Girvin. Wiring up quantum systems. *Nature* **451**, 664–669 (2008).

[10] N. Gisin and R. Thew. Quantum communication. *Nature Photonics* **1**, 165–171 (2007).

[11] E. Knill. Quantum computing. *Nature* **463**, 441–443 (2010).

[12] P. Zoller, T. Beth, D. Binosi, R. Blatt, H. Briegel, D. Bruss, T. Calarco, J. I. Cirac, D. Deutsch, J. Eisert, A. Ekert, C. Fabre, N. Gisin, P. Grangiere, M. Grassl, S. Haroche, A. Imamoglu, A. Karlson, J. Kempe, L. Kouwenhoven, S. Kröll, G. Leuchs, M. Lewenstein, D. Loss, N. Lütkenhaus, S. Massar, J. E. Mooij, M. B. Plenio, E. Polzik, S. Popescu, G. Rempe, A. Sergienko, D. Suter, J. Twamley, G. Wendin, R. Werner, A. Winter, J. Wrachtrup and A. Zeilinger. Quantum information processing and communication. *The European Physical Journal D* **36**, 203–228 (2005).

[13] R. P. Feynman. Simulating physics with computers. *International Journal of Theoretical Physics* **21**, 467–488 (1982).

[14] S. Lloyd. Universal Quantum Simulators. *Science* **273**, 1073–1078 (1996).

[15] D. Deutsch. Quantum Theory, the Church-Turing Principle and the Universal Quantum Computer. *Proceedings of the Royal Society A: Mathematical, Physical and Engineering Sciences* **400**, 97–117 (1985).

[16] C. Bennett and D. DiVincenzo. Quantum information and computation. *Nature* **404**, 247–255 (2000).

[17] P. W. Shor. Algorithms for quantum computation: discrete logarithms and factoring. *Proceedings 35th Annual Symposium on Foundations of Computer Science* **35**, 124–134 (1994).

[18] L. K. Grover. A fast quantum mechanical algorithm for database search. *Proceedings of the twentyeighth annual ACM symposium on Theory of computing STOC 96* **28**, 8 (1996).

[19] C. H. Bennett and G. Brassard. Quantum Cryptography: Public Key Distribution and Coin Tossing. In: *Proceedings of the IEEE International Conference on Computers, Systems and Signal Processing*, 175–179, New York, (1984).

[20] A. K. Ekert. Quantum cryptography based on Bell's theorem. *Physical Review Letters* **67**, 661–663 (1991).

[21] W. K. Wootters and W. H. Zurek. A single quantum cannot be cloned. *Nature* **299**, 802–803 (1982).

[22] D. Deutsch, A. Ekert, R. Jozsa, C. Macchiavello, S. Popescu and A. Sanpera. Quantum Privacy Amplification and the Security of Quantum Cryptography over Noisy Channels. *Physical Review Letters* **77**, 2818–2821 (1996).

[23] N. Gisin, G. Ribordy, W. Tittel and H. Zbinden. Quantum cryptography. *Reviews of Modern Physics* **74**, 145–195 (2002).

[24] N. Lütkenhaus and A. J. Shields. Focus on Quantum Cryptography: Theory and Practice. *New Journal of Physics* **11**, 45005 (2009).

[25] A. I. Lvovsky, B. C. Sanders and W. Tittel. Optical quantum memory. *Nature Photonics* **3**, 706–714 (2009).

[26] C. Simon, M. Afzelius, J. Appel, A. Boyer de la Giroday, S. J. Dewhurst, N. Gisin, C. Y. Hu, F. Jelezko, S. Kröll, J. H. Müller, J. Nunn, E. S. Polzik, J. G. Rarity, H. De Riedmatten, W. Rosenfeld, A. J. Shields, N. Sköld, R. M. Stevenson, R. Thew, I. A. Walmsley, M. C. Weber, H. Weinfurter, J. Wrachtrup and R. J. Young. Quantum memories. *The European Physical Journal D - Atomic, Molecular, Optical and Plasma Physics* **58**, 1–22 (2010).

[27] H. J. Kimble. The quantum internet. *Nature* **453**, 1023–1030 (2008).

[28] K. Hammerer, A. S. Sørensen and E. S. Polzik. Quantum interface between light and atomic ensembles. *Reviews of Modern Physics* **82**, 1041–1093 (2010).

[29] N. Sangouard, C. Simon, H. de Riedmatten and N. Gisin. Quantum repeaters based on atomic ensembles and linear optics. *Reviews of Modern Physics* **83**, 33–80 (2011).

[30] H. de Riedmatten, M. Afzelius, M. U. Staudt, C. Simon and N. Gisin. A solid-state light-matter interface at the single-photon level. *Nature* **456**, 773–777 (2008).

[31] L.-M. Duan, M. D. Lukin, J. I. Cirac and P. Zoller. Long-distance quantum communication with atomic ensembles and linear optics. *Nature* **414**, 413–418 (2001).

[32] L.-M. Duan and C. Monroe. Quantum networks with trapped ions. *Reviews of Modern Physics* **82**, 1209–1224 (2010).

[33] N. Akopian, N. Lindner, E. Poem, Y. Berlatzky, J. Avron, D. Gershoni, B. Gerardot and P. Petroff. Entangled Photon Pairs from Semiconductor Quantum Dots. *Physical Review Letters* **96**, 130501 (2006).

[34] P. C. Maurer, G. Kucsko, C. Latta, L. Jiang, N. Y. Yao, S. D. Bennett, F. Pastawski, D. Hunger, N. Chisholm, M. Markham, D. J. Twitchen, J. I. Cirac and M. D. Lukin. Room-Temperature Quantum Bit Memory Exceeding One Second. *Science* **336**, 1283–1286 (2012).

[35] M. Steger, K. Saeedi, M. L. W. Thewalt, J. J. L. Morton, H. Riemann, N. V. Abrosimov, P. Becker and H.-J. Pohl. Quantum information storage for over 180 s using donor spins in a 28Si "semiconductor vacuum". *Science* **336**, 1280–1283 (2012).

[36] B. Lounis and M. Orrit. Single-photon sources. *Reports on Progress in Physics* **68**, 1129–1179 (2005).

[37] D. Jaksch, J. I. Cirac, P. Zoller, S. L. Rolston, R. Côté and M. D. Lukin. Fast Quantum Gates for Neutral Atoms. *Physical Review Letters* **85**, 2208–2211 (2000).

[38] L. Isenhower, E. Urban, X. L. Zhang, A. T. Gill, T. Henage, T. A. Johnson, T. G. Walker and M. Saffman. Demonstration of a Neutral Atom Controlled-NOT Quantum Gate. *Physical Review Letters* **104**, 010503 (2010).

[39] N. Timoney, I. Baumgart, M. Johanning, A. F. Varon, M. B. Plenio, A. Retzker and C. Wunderlich. Quantum gates and memory using microwave-dressed states. *Nature* **476**, 185–188 (2011).

[40] J. P. Home, D. Hanneke, J. D. Jost, J. M. Amini, D. Leibfried and D. J. Wineland. Complete methods set for scalable ion trap quantum information processing. *Science* **325**, 1227–1230 (2009).

[41] J. I. Cirac, P. Zoller, H. J. Kimble and H. Mabuchi. Quantum State Transfer and Entanglement Distribution among Distant Nodes in a Quantum Network. *Physical Review Letters* **78**, 3221–3224 (1997).

[42] T. D. Ladd, F. Jelezko, R. Laflamme, Y. Nakamura, C. Monroe and J. L. O'Brien. Quantum computers. *Nature* **464**, 45–53 (2010).

[43] C. H. Bennett, G. Brassard, C. Crépeau, R. Jozsa, A. Peres and W. K. Wootters. Teleporting an unknown quantum state via dual classical and Einstein-Podolsky-Rosen channels. *Physical Review Letters* **70**, 1895–1899 (1993).

[44] H. P. Specht, C. Nölleke, A. Reiserer, M. Uphoff, E. Figueroa, S. Ritter and G. Rempe. A single-atom quantum memory. *Nature* **473**, 190–193 (2011).

[45] S. Ritter, C. Nölleke, C. Hahn, A. Reiserer, A. Neuzner, M. Uphoff, M. Mücke, E. Figueroa, J. Bochmann and G. Rempe. An elementary quantum network of single atoms in optical cavities. *Nature* **484**, 195–200 (2012).

[46] H. J. Briegel, W. Dür, J. I. Cirac and P. Zoller. Quantum Repeaters: The Role of Imperfect Local Operations in Quantum Communication. *Physical Review Letters* **81**, 5932–5935 (1998).

[47] J.-W. Pan, D. Bouwmeester, H. Weinfurter and A. Zeilinger. Experimental Entanglement Swapping: Entangling Photons That Never Interacted. *Physical Review Letters* **80**, 3891–3894 (1998).

[48] C. Nölleke, A. Neuzner, A. Reiserer, C. Hahn, G. Rempe and S. Ritter. Efficient Teleportation Between Remote Single-Atom Quantum Memories. *Physical Review Letters* **110**, 140403 (2013).

[49] S. Nußmann. Kühlen und Positionieren eines Atoms in einem optischen Resonator. Ph.D. Thesis, Max-Planck-Institut für Quantenoptik / Technische Universität München (2006).

[50] B. Weber. Distribution of quantum information between an atom and two photons. Ph.D. Thesis, Max-Planck-Institut für Quantenoptik / Technische Universität München (2008).

[51] J. Bochmann. Coherent Dynamics and State Detection of Single Atoms in a Cavity. Ph.D. Thesis, Max-Planck-Institut für Quantenoptik / Technische Universität München (2010).

[52] M. Mücke. Elektromagnetisch induzierte Transparenz mit einem einzelnen Atom. Ph.D. Thesis, Max-Planck-Institut für Quantenoptik / Technische Universität München (2011).

[53] S. Nußmann, K. Murr, M. Hijlkema, B. Weber, A. Kuhn and G. Rempe. Vacuum-stimulated cooling of single atoms in three dimensions. *Nature Physics* **1**, 122–125 (2005).

[54] A. Reiserer, C. Nölleke, S. Ritter and G. Rempe. Ground-State Cooling of a Single Atom at the Center of an Optical Cavity. *Physical Review Letters* **110**, 223003 (2013).

[55] S. Nußmann, M. Hijlkema, B. Weber, F. Rohde, G. Rempe and A. Kuhn. Submicron Positioning of Single Atoms in a Microcavity. *Physical Review Letters* **95**, 173602 (2005).

[56] M. A. Nielsen and I. L. Chuang. *Quantum Computation and Quantum Information*. Cambridge University Press, 1 Edition (2000).

[57] M. Prevedelli, F. T. G. M and T. W. Hänsch. Phase Locking of Grating Tuned Diode Lasers. *Appl Phys B* **60**, S241–S248 (1995).

[58] N. Strauß, I. Ernsting, S. Schiller, A. Wicht, P. Huke and R.-H. Rinkleff. A simple scheme for precise relative frequency stabilization of lasers. *Applied Physics B: Lasers*

and Optics **88**, 21–28 (2007).

[59] H. P. Specht. Einzelatom-Quantenspeicher für Polarisations-Qubits. Ph.D. Thesis, Max-Planck-Institut für Quantenoptik / Technische Universität München (2010).

[60] R. W. P. Drever, J. L. Hall, F. V. Kowalski, J. Hough, G. M. Ford, A. J. Munley and H. Ward. Laser phase and frequency stabilization using an optical resonator. *Applied Physics B: Lasers and Optics* **31**, 97–105 (1983).

[61] M. Hijlkema. Single photons from a single atom trapped in a high-finesse optical cavity. Ph.D. Thesis, Max-Planck-Institut für Quantenoptik / Technische Universität München (2007).

[62] W. Rosenfeld, J. Volz, M. Weber and H. Weinfurter. Coherence of a qubit stored in Zeeman levels of a single optically trapped atom. *Physical Review A* **84**, 022343 (2011).

[63] C. Guhl. Zustandsdetektion einzelner Atome in einem optischen Resonator hoher Finesse. Diploma Thesis, Max-Planck-Institut für Quantenoptik / Technische Universität München (2009).

[64] J. Bochmann, M. Mücke, C. Guhl, S. Ritter, G. Rempe and D. L. Moehring. Lossless State Detection of Single Neutral Atoms. *Physical Review Letters* **104**, 203601 (2010).

[65] J. B. Altepeter, E. R. Jeffrey and P. G. Kwiat. Photonic State Tomography. *Advances In Atomic, Molecular, and Optical Physics* **52**, 105–159 (2005).

[66] U. Fano. A Stokes-Parameter Technique for the Treatment of Polarization in Quantum Mechanics. *Physical Review* **93**, 121–123 (1954).

[67] D. F. V. James, P. G. Kwiat, W. J. Munro and A. G. White. Measurement of qubits. *Physical Review A* **64**, 052312 (2001).

[68] M. Howard, J. Twamley, C. Wittmann, T. Gaebel, F. Jelezko and J. Wrachtrup. Quantum process tomography and Linblad estimation of a solid-state qubit. *New Journal of Physics* **8**, 33 (2006).

[69] I. Chuang and M. A. Nielsen. Prescription for experimental determination of the dynamics of a quantum black box. *Journal of Modern Optics* **44**, 2455–2467 (1997).

[70] J. Fiurášek and Z. Hradil. Maximum-likelihood estimation of quantum processes. *Physical Review A* **63**, 020101 (2001).

[71] J. L. O'Brien, G. J. Pryde, A. Gilchrist, D. F. V. James, N. K. Langford, T. C. Ralph and A. G. White. Quantum Process Tomography of a Controlled-NOT Gate. *Physical Review Letters* **93**, 080502 (2004).

[72] M. D. Bowdrey, D. K. Oi, A. J. Short, K. Banaszek and J. A. Jones. Fidelity of single qubit maps. *Physics Letters A* **294**, 258–260 (2002).

[73] A. Gilchrist, N. Langford and M. Nielsen. Distance measures to compare real and ideal quantum processes. *Physical Review A* **71**, 062310 (2005).

[74] N. Kiesel, C. Schmid, U. Weber, R. Ursin and H. Weinfurter. Linear Optics Controlled-

Phase Gate Made Simple. *Physical Review Letters* **95**, 210505 (2005).

[75] N. Kiesel. Experiments on Multiphoton Entanglement. Ph.D. Thesis, LMU München (2007).

[76] I. Bongioanni, L. Sansoni, F. Sciarrino, G. Vallone and P. Mataloni. Experimental quantum process tomography of non-trace-preserving maps. *Physical Review A* **82**, 042307 (2010).

[77] A. Bendersky, F. Pastawski and J. Paz. Selective and efficient quantum process tomography. *Physical Review A* **80**, 032116 (2009).

[78] C. T. Schmiegelow, M. A. Larotonda and J. P. Paz. Selective and Efficient Quantum Process Tomography with Single Photons. *Physical Review Letters* **104**, 123601 (2010).

[79] A. Klappenecker and M. Roetteler. Mutually Unbiased Bases are Complex Projective 2-Designs. *arXiv:quant-ph* 0502031 (2005).

[80] C. Dankert, R. Cleve, J. Emerson and E. Livine. Exact and approximate unitary 2-designs and their application to fidelity estimation. *Physical Review A* **80**, 012304 (2009).

[81] E. Schrödinger. Discussion of Probability Relations between Separated Systems. *Mathematical Proceedings of the Cambridge Philosophical Society* **31**, 555–563 (1935).

[82] K. Mattle, H. Weinfurter, P. G. Kwiat and A. Zeilinger. Dense Coding in Experimental Quantum Communication. *Physical Review Letters* **76**, 4656–4659 (1996).

[83] M. B. Plenio and S. Virmani. An introduction to entanglement measures. *Quantum Information and Computation* **7**, 1–51 (2007).

[84] S. J. van Enk, N. Lütkenhaus and H. J. Kimble. Experimental procedures for entanglement verification. *Physical Review A* **75**, 052318 (2007).

[85] M. Horodecki, P. Horodecki and R. Horodecki. Separability of mixed states: necessary and sufficient conditions. *Physics Letters A* **223**, 1–8 (1996).

[86] O. Gühne, P. Hyllus, D. Bruss, A. Ekert, M. Lewenstein, C. Macchiavello and A. Sanpera. Detection of entanglement with few local measurements. *Physical Review A* **66**, 062305 (2002).

[87] M. Lettner. Ein Bose-Einstein-Kondensat als Quantenspeicher für Zwei-Teilchen-Verschränkung. Ph.D. Thesis, Max-Planck-Institut für Quantenoptik / Technische Universität München (2011).

[88] A. D. Boozer, A. Boca, R. Miller, T. E. Northup and H. J. Kimble. Reversible State Transfer between Light and a Single Trapped Atom. *Physical Review Letters* **98**, 193601 (2007).

[89] T. Wilk, S. C. Webster, A. Kuhn and G. Rempe. Single-atom single-photon quantum interface. *Science* **317**, 488–490 (2007).

[90] A. Kuhn, M. Hennrich, T. Bondo and G. Rempe. Controlled generation of single

photons from a strongly coupled atom-cavity system. *Applied Physics B: Lasers and Optics* **69**, 373–377 (1999).

[91] M. Hijlkema, B. Weber, H. P. Specht, S. C. Webster, A. Kuhn and G. Rempe. A single-photon server with just one atom. *Nature Physics* **3**, 253–255 (2007).

[92] M. Mücke, J. Bochmann, C. Hahn, A. Neuzner, C. Nölleke, A. Reiserer, G. Rempe and S. Ritter. Generation of single photons from an atom-cavity system. *Physical Review A* **87**, 063805 (2013).

[93] M. Hennrich. Kontrollierte Erzeugung einzelner Photonen in einem optischen Resonator hoher Finesse. Ph.D. Thesis, Max-Planck-Institut für Quantenoptik / Technische Universität München (2003).

[94] T. Legero, T. Wilk, M. Hennrich, G. Rempe and A. Kuhn. Quantum Beat of Two Single Photons. *Physical Review Letters* **93**, 070503 (2004).

[95] M. Keller, B. Lange, K. Hayasaka, W. Lange and H. Walther. Continuous generation of single photons with controlled waveform in an ion-trap cavity system. *Nature* **431**, 1075–1078 (2004).

[96] T. Wilk, H. P. Specht, S. C. Webster, G. Rempe and A. Kuhn. Scheme for generating a sequence of single photons of alternating polarization. *Journal of Modern Optics* **54**, 1569–1580 (2007).

[97] T. Wilk, S. C. Webster, H. P. Specht, G. Rempe and A. Kuhn. Polarization-Controlled Single Photons. *Physical Review Letters* **98**, 063601 (2007).

[98] B. Weber, H. P. Specht, T. Müller, J. Bochmann, M. Mücke, D. L. Moehring and G. Rempe. Photon-Photon Entanglement with a Single Trapped Atom. *Physical Review Letters* **102**, 030501 (2009).

[99] S. Baur. Speicherung der Polarisation von Licht in einem Bose-Einstein-Kondensat. Diploma Thesis, Max-Planck-Institut für Quantenoptik / Technische Universität München (2010).

[100] D. A. Steck. Rubidium 87 D Line Data. http://steck.us/alkalidata/ (Version 2.1.4) (2010).

[101] S. Massar and S. Popescu. Optimal Extraction of Information from Finite Quantum Ensembles. *Physical Review Letters* **74**, 1259–1263 (1995).

[102] V. Winkler and A. Neuzner. Qubits und verschränkte Atome. *c't* **12**, 42–43 (2012).

[103] D. L. Moehring, P. Maunz, S. Olmschenk, K. C. Younge, D. N. Matsukevich, L.-M. Duan and C. Monroe. Entanglement of single-atom quantum bits at a distance. *Nature* **449**, 68–71 (2007).

[104] C. Bennett, G. Brassard, S. Popescu, B. Schumacher, J. Smolin and W. Wootters. Purification of Noisy Entanglement and Faithful Teleportation via Noisy Channels. *Physical Review Letters* **76**, 722–725 (1996).

[105] W. Dür, H. J. Briegel, J. I. Cirac and P. Zoller. Quantum repeaters based on

entanglement purification. *Physical Review A* **59**, 169–181 (1999).

[106] C. H. Bennett, S. Popescu and B. Schumacher. Concentrating partial entanglement by local operations. *Physical Review A* **53**, 2046–2052 (1996).

[107] C. Bennett, D. DiVincenzo, J. Smolin and W. Wootters. Mixed-state entanglement and quantum error correction. *Physical Review A* **54**, 3824–3851 (1996).

[108] R. Horodecki, M. Horodecki and P. Horodecki. Teleportation, Bell's inequalities and inseparability. *Physics Letters A* **222**, 21–25 (1996).

[109] S. Popescu. Bell's inequalities versus teleportation: What is nonlocality? *Physical Review Letters* **72**, 797–799 (1994).

[110] D. Bouwmeester, J.-W. Pan, K. Mattle, M. Eibl, H. Weinfurter and A. Zeilinger. Experimental quantum teleportation. *Nature* **390**, 575–579 (1997).

[111] D. Boschi, S. Branca, F. De Martini, L. Hardy and S. Popescu. Experimental Realization of Teleporting an Unknown Pure Quantum State via Dual Classical and Einstein-Podolsky-Rosen Channels. *Physical Review Letters* **80**, 1121–1125 (1998).

[112] A. Furusawa, J. L. Sørensen, S. L. Braunstein, C. A. Fuchs, H. J. Kimble and E. S. Polzik. Unconditional Quantum Teleportation. *Science* **282**, 706–709 (1998).

[113] E. Knill, R. Laflamme and G. J. Milburn. A scheme for efficient quantum computation with linear optics. *Nature* **409**, 46–52 (2001).

[114] I. Marcikic, H. de Riedmatten, W. Tittel, H. Zbinden and N. Gisin. Long-distance teleportation of qubits at telecommunication wavelengths. *Nature* **421**, 509–513 (2003).

[115] H. de Riedmatten, I. Marcikic, W. Tittel, H. Zbinden, D. Collins and N. Gisin. Long Distance Quantum Teleportation in a Quantum Relay Configuration. *Physical Review Letters* **92**, 047904 (2004).

[116] D. Collins, N. Gisin and H. De Riedmatten. Quantum relays for long distance quantum cryptography. *Journal of Modern Optics* **52**, 735–753 (2005).

[117] X.-S. Ma, T. Herbst, T. Scheidl, D. Wang, S. Kropatschek, W. Naylor, B. Wittmann, A. Mech, J. Kofler, E. Anisimova, V. Makarov, T. Jennewein, R. Ursin and A. Zeilinger. Quantum teleportation over 143 kilometres using active feed-forward. *Nature* **489**, 269–273 (2012).

[118] X.-M. Jin, J.-G. Ren, B. Yang, Z.-H. Yi, F. Zhou, X.-F. Xu, S.-K. Wang, D. Yang, Y.-F. Hu, S. Jiang, T. Yang, H. Yin, K. Chen, C.-Z. Peng and J.-W. Pan. Experimental free-space quantum teleportation. *Nature Photonics* **4**, 376–381 (2010).

[119] J. Yin, J.-G. Ren, H. Lu, Y. Cao, H.-L. Yong, Y.-P. Wu, C. Liu, S.-K. Liao, F. Zhou, Y. Jiang, X.-D. Cai, P. Xu, G.-S. Pan, J.-J. Jia, Y.-M. Huang, H. Yin, J.-Y. Wang, Y.-A. Chen, C.-Z. Peng and J.-W. Pan. Quantum teleportation and entanglement distribution over 100-kilometre free-space channels. *Nature* **488**, 185–188 (2012).

[120] P. Villoresi, T. Jennewein, F. Tamburini, M. Aspelmeyer, C. Bonato, R. Ursin,

C. Pernechele, V. Luceri, G. Bianco, A. Zeilinger and C. Barbieri. Experimental verification of the feasibility of a quantum channel between space and Earth. *New Journal of Physics* **10**, 033038 (2008).

[121] A. Kogut, D. N. Spergel, C. Barnes, C. L. Bennett, M. Halpern, G. Hinshaw, N. Jarosik, M. Limon, S. S. Meyer, L. Page, G. S. Tucker, E. Wollack and E. L. Wright. First-Year Wilkinson Microwave Anisotropy Probe (WMAP) Observations: Temperature-Polarization Correlation. *The Astrophysical Journal Supplement Series* **148**, 161–173 (2003).

[122] J. van Houwelingen, N. Brunner, A. Beveratos, H. Zbinden and N. Gisin. Quantum Teleportation with a Three-Bell-State Analyzer. *Physical Review Letters* **96**, 130502 (2006).

[123] U. Andersen, G. Leuchs and C. Silberhorn. Continuous-variable quantum information processing. *Laser & Photonics Reviews* **4**, 337–354 (2010).

[124] J. F. Sherson, H. Krauter, R. K. Olsson, B. Julsgaard, K. Hammerer, I. Cirac and E. S. Polzik. Quantum teleportation between light and matter. *Nature* **443**, 557–560 (2006).

[125] H. Krauter, D. Salart, C. A. Muschik, J. M. Petersen, H. Shen, T. Fernholz and E. S. Polzik. Deterministic quantum teleportation between distant atomic objects. *Nature Physics* **9**, 400–404 (2013).

[126] S. L. Braunstein and H. J. Kimble. Teleportation of Continuous Quantum Variables. *Physical Review Letters* **80**, 869–872 (1998).

[127] S. Pirandola and S. Mancini. Quantum teleportation with continuous variables: A survey. *Laser Physics* **16**, 1418–1438 (2006).

[128] M. Riebe, H. Haffner, C. F. Roos, W. Hansel, J. Benhelm, G. P. T. Lancaster, T. W. Korber, C. Becher, F. Schmidt-Kaler, D. F. V. James and R. Blatt. Deterministic quantum teleportation with atoms. *Nature* **429**, 734–737 (2004).

[129] M. D. Barrett, J. Chiaverini, T. Schaetz, J. Britton, W. M. Itano, J. D. Jost, E. Knill, C. Langer, D. Leibfried, R. Ozeri and D. J. Wineland. Deterministic quantum teleportation of atomic qubits. *Nature* **429**, 737–739 (2004).

[130] L. Steffen, A. Fedorov, M. Oppliger, Y. Salathe, P. Kurpiers, M. Baur, G. Puebla-Hellmann, C. Eichler and A. Wallraff. Realization of Deterministic Quantum Teleportation with Solid State Qubits. *arXiv* 1302.5621 (2013).

[131] Y.-A. Chen, S. Chen, Z.-S. Yuan, B. Zhao, C.-S. Chuu, J. Schmiedmayer and J.-W. Pan. Memory-built-in quantum teleportation with photonic and atomic qubits. *Nature Physics* **4**, 103–107 (2008).

[132] S. Olmschenk, D. N. Matsukevich, P. Maunz, D. Hayes, L.-M. Duan and C. Monroe. Quantum Teleportation Between Distant Matter Qubits. *Science* **323**, 486–489 (2009).

[133] M. A. Nielsen, E. Knill and R. Laflamme. Complete quantum teleportation using

nuclear magnetic resonance. *Nature* **396**, 52–55 (1998).

[134] X.-H. Bao, X.-F. Xu, C.-M. Li, Z.-S. Yuan, C.-Y. Lu and J.-W. Pan. Quantum teleportation between remote atomic-ensemble quantum memories. *Proceedings of the National Academy of Sciences of the United States of America* **109**, 20347 (2012).

[135] M. Lukin, S. Yelin and M. Fleischhauer. Entanglement of Atomic Ensembles by Trapping Correlated Photon States. *Physical Review Letters* **84**, 4232–4235 (2000).

[136] D. Phillips, A. Fleischhauer, A. Mair, R. Walsworth and M. Lukin. Storage of Light in Atomic Vapor. *Physical Review Letters* **86**, 783–786 (2001).

[137] C. Liu, Z. Dutton, C. H. Behroozi and L. V. Hau. Observation of coherent optical information storage in an atomic medium using halted light pulses. *Nature* **409**, 490–493 (2001).

[138] H. Weinfurter. Experimental Bell-State Analysis. *Europhysics Letters (EPL)* **25**, 559–564 (1994).

[139] S. Braunstein and A. Mann. Measurement of the Bell operator and quantum teleportation. *Physical Review A* **51**, R1727–R1730 (1995).

[140] M. Born and E. Wolf. *Principles of Optics: Electromagnetic Theory of Propagation, Interference and Diffraction of Light.* Cambridge University Press, 7 Edition (1999).

[141] T. Legero. Zeitaufgelöste Zwei-Photonen-Interferenz. Ph.D. Thesis, Max-Planck-Institut für Quantenoptik / Technische Universität München (2005).

[142] A. Zeilinger. General properties of lossless beam splitters in interferometry. *American Journal of Physics* **49**, 882 (1981).

[143] C. K. Hong, Z. Y. Ou and L. Mandel. Measurement of subpicosecond time intervals between two photons by interference. *Physical Review Letters* **59**, 2044–2046 (1987).

[144] A. Zeilinger, H. J. Bernstein and M. Horne. Information Transfer with Two-state Two-particle Quantum Systems. *Journal of Modern Optics* **41**, 2375–2384 (1994).

[145] J. Calsamiglia and N. Lütkenhaus. Maximum efficiency of a linear-optical Bell-state analyzer. *Applied Physics B* **72**, 67–71 (2001).

[146] T. Legero, T. Wilk, A. Kuhn and G. Rempe. Characterization of single photons using two-photon interference. *Advances In Atomic, Molecular, and Optical Physics* **53**, 253–289 (2006).

[147] R. J. Glauber. *Quantum Theory of Optical Coherence: Selected Papers and Lectures.* Wiley, 1 Edition (2007).

[148] M. Fleischhauer, S. Yelin and M. Lukin. How to trap photons? Storing single-photon quantum states in collective atomic excitations. *Optics Communications* **179**, 395–410 (2000).

[149] G. S. Vasilev, D. Ljunggren and A. Kuhn. Single photons made-to-measure. *New Journal of Physics* **12**, 063024 (2010).

[150] P. P. Rohde, T. C. Ralph and M. A. Nielsen. Optimal photons for quantum-information processing. *Physical Review A* **72**, 052332 (2005).

[151] H. P. Specht, J. Bochmann, M. Mücke, B. Weber, E. Figueroa, D. L. Moehring and G. Rempe. Phase shaping of single-photon wave packets. *Nature Photonics* **3**, 469–472 (2009).

[152] C. Langer, R. Ozeri, J. D. Jost, J. Chiaverini, B. DeMarco, A. B. Kish, R. B. Blakestad, J. Britton, D. B. Hume, W. M. Itano, D. Leibfried, R. Reichle, T. Rosenband, T. Schaetz, P. O. Schmidt and D. J. Wineland. Long-Lived Qubit Memory Using Atomic Ions. *Physical Review Letters* **95**, 060502 (2005).

[153] D. Hunger, T. Steinmetz, Y. Colombe, C. Deutsch, T. W. Hänsch and J. Reichel. A fiber Fabry-Perot cavity with high finesse. *New Journal of Physics* **12**, 065038 (2010).

[154] M. Steiner, H. M. Meyer, C. Deutsch, J. Reichel and M. Köhl. Single Ion Coupled to an Optical Fiber Cavity. *Physical Review Letters* **110**, 043003 (2013).

[155] P. F. Herskind, A. Dantan, J. P. Marler, M. Albert and M. Drewsen. Realization of collective strong coupling with ion Coulomb crystals in an optical cavity. *Nature Physics* **5**, 494–498 (2009).

[156] R. B. Patel, A. J. Bennett, I. Farrer, C. A. Nicoll, D. A. Ritchie and A. J. Shields. Two-photon interference of the emission from electrically tunable remote quantum dots. *Nature Photonics* **4**, 632–635 (2010).

[157] R. Lettow, Y. L. a. Rezus, A. Renn, G. Zumofen, E. Ikonen, S. Götzinger and V. Sandoghdar. Quantum Interference of Tunably Indistinguishable Photons from Remote Organic Molecules. *Physical Review Letters* **104**, 123605 (2010).

[158] H. Bernien, L. Childress, L. Robledo, M. Markham, D. Twitchen and R. Hanson. Two-Photon Quantum Interference from Separate Nitrogen Vacancy Centers in Diamond. *Physical Review Letters* **108**, 043604 (2012).

[159] A. Sipahigil, M. Goldman, E. Togan, Y. Chu, M. Markham, D. Twitchen, A. Zibrov, A. Kubanek and M. Lukin. Quantum Interference of Single Photons from Remote Nitrogen-Vacancy Centers in Diamond. *Physical Review Letters* **108**, 143601 (2012).

[160] S. Lloyd, M. S. Shahriar, J. H. Shapiro and P. R. Hemmer. Long Distance, Unconditional Teleportation of Atomic States via Complete Bell State Measurements. *Physical Review Letters* **87**, 167903 (2001).

[161] R. Gehr, J. Volz, G. Dubois, T. Steinmetz, Y. Colombe, B. L. Lev, R. Long, J. Estève and J. Reichel. Cavity-Based Single Atom Preparation and High-Fidelity Hyperfine State Readout. *Physical Review Letters* **104**, 203602 (2010).

[162] J. Volz, R. Gehr, G. Dubois, J. Esteve and J. Reichel. Measurement of the internal state of a single atom without energy exchange. *Nature* **475**, 210–213 (2011).

[163] J. Cirac and A. Parkins. Schemes for atomic-state teleportation. *Physical Review A* **50**, R4441–R4444 (1994).

[164] J. Hofmann, M. Krug, N. Ortegel, L. Gerard, M. Weber, W. Rosenfeld and H. Weinfurter. Heralded Entanglement Between Widely Separated Atoms. *Science* **337**, 72–75 (2012).

[165] T. Pellizzari, S. Gardiner, J. Cirac and P. Zoller. Decoherence, Continuous Observation, and Quantum Computing: A Cavity QED Model. *Physical Review Letters* **75**, 3788–3791 (1995).

[166] D. F. Walls and G. J. Milburn. *Quantum optics*. Springer, 2 Edition (2008).

[167] J. Johansson, P. Nation and F. Nori. QuTiP: An open-source Python framework for the dynamics of open quantum systems. *Computer Physics Communications* **183**, 1760–1772 (2012).

[168] R. Grimm, M. Weidemüller and Y. B. Ovchinnikov. Optical dipole traps for neutral atoms. *Advances in Atomic, Molecular and Optical Physics and Optical Physics* **42**, 95–170 (2000).

Publications

GROUND-STATE COOLING OF A SINGLE ATOM AT THE CENTER OF AN OPTICAL CAVITY
A. Reiserer, C. Nölleke, S. Ritter, G. Rempe
Physical Review Letters **110**, 223003 (2013).

EFFICIENT TELEPORTATION BETWEEN REMOTE SINGLE-ATOM QUANTUM MEMORIES
C. Nölleke, A. Neuzner, A. Reiserer, C. Hahn, G. Rempe, S. Ritter
Physical Review Letters **110**, 140403 (2013).

GENERATION OF SINGLE PHOTONS FROM AN ATOM-CAVITY SYSTEM
M. Mücke, J. Bochmann, C. Hahn, A. Neuzner, C. Nölleke, A. Reiserer, G. Rempe, S. Ritter
Physical Review A **87**, 063805 (2013).

AN ELEMENTARY QUANTUM NETWORK OF SINGLE ATOMS IN OPTICAL CAVITIES
S. Ritter, C. Nölleke, C. Hahn, A. Reiserer, A. Neuzner, M. Uphoff, M. Mücke, E. Figueroa, J. Bochmann, G. Rempe
Nature **484**, 195-200 (2012).

A SINGLE-ATOM QUANTUM MEMORY
H. P. Specht, C. Nölleke, A. Reiserer, M. Uphoff, E. Figueroa, S. Ritter, G. Rempe
Nature **473**, 190-193 (2011).

Danke!

An dieser Stelle möchte ich allen danken die zum Gelingen dieser Arbeit beigetragen haben.

Mein erster Dank gilt Prof. Gerhard Rempe für das mir entgegengebrachte Vertrauen und für die Möglichkeit, auf dem spannenden Gebiet der Quantenoptik zu arbeiten.

Weiterer großer Dank für die freundschaftliche, aber immer unglaublich professionelle Zusammenarbeit gilt meinen Kollegen vom *Netzwerkknoten A*, namentlich Holger Specht, Andreas Reiserer, Manuel Uphoff und Eden Figueroa, sowie vom *Netzwerkknoten B*, Jörg Bochmann, Martin Mücke, Andreas Neuzner und Carolin Hahn. Insbesondere danke ich Holger, der mich zu Beginn mit sehr viel Geduld an das komplexe Experiment herangeführt hat, und Eden, der mich an seiner *passion* für die Physik teilhaben ließ. Die meiste Zeit im Labor durfte ich mit Andi R. verbringen, der mit vielen Ideen und großen Enthusiasmus das Experiment deutlich weiterentwickelt hat. Eine großes Dankeschön an alle für 4 Jahre Laborwahnsinn inklusive der einen oder anderen Messnacht.

Stephan Ritter, der als Post-Doc die beiden losen Enden zu einem Netzwerk verbunden hat, danke ich für die großartige Unterstützung im Labor und bei sonstigen Problemen. Nur aufgrund seiner Begeisterung für unsere Experimente und seiner Fachkenntnisse konnten unsere Projekte überhaupt durchgeführt werden. In diesem Zusammenhang muss auch David Moehring erwähnt werden, der uns leider in Richtung seiner Heimat verlassen hat.

Der Beitrag unserer Techniker, Josef Bayerl, Helmut Stehbeck, Franz Denk, Tobias Urban und Thomas Wiesmeier kann gar nicht hoch genug eingeschätzt werden, da ohne ihre Mitarbeit die durchgeführten Experimente schlicht nicht möglich gewesen wären. Speziell Josef hat mich in den ersten Monaten beim Bau der neuen Cavity mit Rat und Tat unterstützt.

Ich danke der gesamten Arbeitsgruppe für die vielen Grillabende, Skiausflüge und sonstigen Feiern. Zu vergessen sind natürlich nicht die vielen Stunden am Kicker. Es hat sich ausgezahlt. Ebenso wunderbar war das Zusammenspiel mit den Bolzplatzhelden vom SV Quantenkick. Der Spaßfaktor in der Gruppe und am Institut ist definitiv nie zu kurz gekommen, und ich bin froh, ein Teil davon gewesen sein zu dürfen. Mit Dominik Fauser und Eden Figueroa konnte ich meine Begeisterung für schwarzgelben Fußball teilen. Danke für den Double-Sieg und den gemeinsamen Besuch im Westfalenstadion.

Meiner Familie und Andrea danke ich für die Unterstützung in allen Lebenslagen, die ich in den letzten Jahren erfahren durfte.